DUCTILITY OF REINFORCED CONCRETE BRIDGE PIERS

UNDER SEISMIC LOADING

A report submitted in partial fulfilment

of the

requirements for the degree

of

Master of Engineering,

at the University of Canterbury,

Christchurch, New Zealand.

by

ANG BENG GHEE

University of Canterbury

February 1981

ABSTRACT

A continuation of the extensive research project undertaken in the University of Canterbury on ductility of bridge piers is reported. The testing described herein covers an experimental investigation into the post-elastic ductile behaviour of reinforced concrete bridge piers, particularly into the influence of aspect ratio on such behaviour.

The test units, two octagonal and two square sections, were designed according to the Second Draft of the Concrete Design Code DZ 3101, for different axial load levels. The testing included slow static incremental loading followed by fast dynamic cyclic loadings.

The results are presented in the form of load-displacement hysteresis curves, curvature profiles and transverse steel strain distribution. Discussion of results deals with the comparison of ultimate moment capacities, measured ductilities, equivalent plastic hinge lengths, maximum concrete compression strains, the ultimate shear forces, the enhancement of concrete strength by confinement and the idealized stress-strain curves for confined concrete.

Some comparisons with previous projects are made and conclusions drawn from the entire analysis.

ACKNOWLEDGEMENTS

The research reported herein was carried out in the Department of Civil Engineering, University of Canterbury, under the overall guidance of Professor R. Park.

The project was supervised by Dr. M.J.N. Priestley and Professor R. Park, whose advice, guidance and encouragement is gratefully acknowledged.

I wish to take the opportunity to express my appreciation of the assistance given by the Senior Technical Officer, Mr. N.W. Prebble, and all the technical staff of the Department who, in one way or another, contributed towards the success of the project. Special acknowledgements are given to Mr. G. Hill, Mr. G. Clark and Mr. A.H. Bell, because their helpful advice and valuable practical experience in the process of construction and testing enabled me to achieve the successful results.

I am also very grateful for the generous financial assistance provided by the National Roads Board.

Furthermore, the work of Mrs. D.E. Ball in typing the manuscript is very much appreciated. Many thanks to her.

Last but not least, my special thanks to my family for their encouragement and endless support.

TABLE OF CONTENTS

LIST OF FIGURES

LIST OF TABLES

NOTATION

A_c = area of concrete core measured to outside of hoops or spirals.

A_g = gross area of section.

A_{sh} = total effective area of hoop bars and supplementary cross ties in direction under consideration within spacing s_h.

A_{sp} = area of spiral steel.

A_v = area of shear reinforcement.

b = width of compression face of member.

c = neutral axis depth.

d = distance from extreme compression fibre to centroid of tension reinforcement.

D,h = overall lateral dimension of section.

d_s,h" = lateral dimension of section to outside of transverse reinforcement.

E_c = modulus of elasticity of concrete.

f_c = concrete compressive stress.

f'_c = compressive cylinder strength of concrete.

f'_{cc} = enhanced concrete compressive strength.

f''_{cc} = experimental enhanced concrete compressive strength.

f_ℓ = lateral pressure on concrete due to confinement.

f_y = yield strength of longitudinal reinforcement.

f_{yh} = yield strength of transverse reinforcement.

H_u = ultimate lateral load.

I_{gross} = moment of inertia of section.

I_{cr} = moment of inertia of cracked section neglecting tension contribution from concrete.

K = concrete strength enhancement factor.

K_1, K_2, K_3, β_1 = concrete compressive stress block parameters.

k_1, k_3 = factors for equivalent plastic hinge length computation, depending on steel and concrete strength.

M = moment of resistance.

M_u = ultimate moment.

NA = neutral axis

n = modular ratio

p_e = maximum design axial load due to gravity and seismic loading.

S_h = pitch of spiral reinforcing or centre to centre spacing of hoop sets.

V_c = shear force carried by concrete.

V_s = shear force carried by shear reinforcement.

V_u = ultimate shear force.

V_i = ideal shear strength of section.

v_u = ultimate shear stress.

v_b = basic shear stress.

v_c = ideal shear stress provided by concrete.

z, z_m = slope of falling branch of concrete stress-strain relation.

Δ = lateral deflection.

Δ_p = lateral deflection due to inelastic deformation beyond Δ_y.

Δ_y = lateral deflection at first yield.

ε_c = concrete compressive strain.

ε_{cu} = ultimate concrete compressive strain.

ε_{20c} = concrete strain at $0.2f'_c$.

ε_{sh} = strain at strain-hardening of steel.

ε_y = steel strain at commencement of yield.

μ_o = overall displacement ductility factor.

μ = displacement ductility factor.

ϕ = section curvature or strength reduction factor.

ϕ_u = ultimate curvature.

ϕ_y = curvature at first yield.

θ = rotation of centre-block.

θ_p = plastic rotation.

ρ_s = ratio of transverse steel to volume of concrete core measured to the outside of transverse steel.

ρ_t = ratio of total area of longitudinal steel to gross area of column section.

CHAPTER ONE

INTRODUCTION

1.1 GENERAL

It has been shown by dynamic analyses that the theoretical response inertia loads of structures responding elastically to severe earthquake ground motions are significantly greater than the static design lateral loads recommended by codes such as NZS 4203 (1). However, it would be very uneconomical to design structures to respond elastically to such high inertia loads. Hence, if the structures are to survive through such severe earthquakes, some means of energy dissipation need to be provided. So, unless devices such as mechanical energy dissipators are incorporated in the design, the structures must possess sufficient ductility so that seismic energy can be absorbed and dissipated by some form of post-elastic deformation.

Unlike buildings, column hinging in bridge structures is not easily avoidable if adequate ductility is to be achieved. In order to obtain such column hinges sufficient transverse confining reinforcement must be provided to confine the concrete core as well as to prevent the brittle shear failure and at the same time, providing lateral support to the longitudinal flexural reinforcement which, otherwise, will buckle laterally under high axial compression.

The 1971 San Fernando earthquake resulted in the collapse of 5 bridges together with 42 others suffering significant damage. The main cause of the failures was attributed to the inadequate detailing of the bridge columns in terms of providing enough transverse steel in the plastic hinge regions, and in the anchorage of the transverse steel. Nevertheless, this earthquake did give impetus to later research on the seismic design practice for bridges.

At the University of Canterbury, research into the ductility demand and ductility capacity of bridge piers under seismic attack has been carried out during the past decade. This project is a continuation of this extensive research programme.

1.2 AIM AND SCOPE

The aim of this study is to provide further experimental results concerning code provisions for seismic design of bridge piers subject to

reversed flexure and axial loads. Particular attention will be given to

(1) the influence of aspect ratio on the ductility of bridge piers,

and (2) the shear carried by the concrete confined by transverse reinforcement (2,3).

Since significant efforts have been made to discuss and define the term "ductility" and the ductility demand criteria in several previous projects, it is not the intention of this report to elaborate on this topic again.

In this research project, 4 column specimens (2 octagonal and 2 square sections) were designed to the code specifications of the Second draft of DZ 3101 (17) for different levels of axial load. The specimens were similar to those studied by R.T. Potangaroa (4) and W.D. Gill (5) except that the lateral dimension of the cross-section was reduced while the length was increased so as to increase the aspect ratio. Comparison with their results is included in the later part of this research report.

1.3 REVIEW OF PREVIOUS PROJECTS

A series of theoretical and experimental investigations into the seismic resistance of reinforced concrete bridge columns was conducted at the University of Canterbury. The following paragraphs give a brief review of the related work conducted during M.E. and Ph.D. investigations:

Year*	Brief description of project
1969	Kent (6) investigated the behaviour of flexural members with concrete confined by transverse reinforcement. He attempted to present theoretical stress-strain relations for steel and confined rectangular concrete sections under monotonic loading. The idealization of stress-strain characteristics of confined concrete was assumed to act as the envelope for cyclic behaviour.
1971	Sampson (7) made a theoretical study of the effect of confinement of concrete on curvature ductility for columns under monotonic loading. A computer program was then developed to investigate the parameters which influence the stress-strain behaviour.

* It refers to the year in which the preparation of the report was completed.

1972 Norton (8) extended the work of Sampson by further studying the moment-curvature characteristics of rectangular eccentrically loaded reinforced columns. He discovered that the then design procedures recommended by some seismic codes of practice were unsound and inadequate. He suggested an alternative and more rational procedure for detailing.

1974 Leslie (9) conducted a comprehensive literature survey into the research on the characteristics of confined concrete. From the surveyed materials, he proposed an idealized stress-strain relationship for circularly confined concrete. He also undertook the laboratory testing of grade 380 reinforcing steel to obtain the required cyclic stress-strain behaviour.

1975 Davey (10) started the first testing of reinforced concrete bridge piers, the prototype structure of which was designed according to the MWD "Highway Bridge Design Brief" (15). He subjected the 3 one-third scale octagonal models to static cyclic loading with different moment to shear ratio and found that large post-elastic deformations were available for all the units tested.

1975 Cameron (11) carried out a series of computer analyses to investigate the effects of several parameters on the inelastic seismic response of bridge piers. He drew conclusions on several factors which have significant effects on the seismic resistance performance of bridge piers. Among them were the hysteresis loop shape and the foundation flexibility. He further concluded that the MWD specification of displacement ductility capacity of 6 for highway bridges was a realistic requirement.

1976 Munro (12) continued the experimental work by testing a unit similar to those of Davey's but with a higher spiral steel content. He also tested an identical pier at one-sixth scale on a shaking table to obtain experimental measurements for comparison with theoretical prediction using dynamic inelastic computer analyses. In addition, he put forward the problem of flexible foundations for further research activities.

1978 Ng (13) investigated the interaction between additional foundation flexibility, earthquake characteristics and ductility demand using computer modelling. He further tested Munro's one-sixth model which had not been shaken to destruction and another one-sixth model with large transverse reinforcement content and subject to high axial load. Testing of his second unit showed good ductile behaviour.

1979 Gill (5) conducted tests on 4 full-size reinforced concrete columns with various quantities of rectangular hoops, designed in accordance with the draft concrete code DZ 3101, and subjected to various levels of axial load. The columns were tested under simulated earthquake loadings and the results obtained showed good ductile behaviour. Considerable enhancement of flexural strength was observed over that calculated by normal code design procedures.

1979 Potangaroa (4) conducted tests similar to Gill's work but on octagonal specimens with spiral reinforcement. Again, the results demonstrated good ductile behaviour for the columns designed to the confinement requirements of DZ 3101. He also noticed a large increase in the flexural strength and the high maximum concrete strains at the extreme compression fibre of the confined core.

The above review, though not fully comprehensive, illustrates the trend along which the research programmes have been conducted. Since this project is the continuation of Gill's and Potangaroa's work, more detailed descriptions of their projects and results will be given elsewhere in other chapters.

In particular, the tests reported herein were intended to provide a more stringent test of confinement requirements of DZ 3101 (16,17). Because of the squat nature of Potangaroa's and Gill's test units (aspect ratio of 2) it is possible that the steep moment gradient and effects of additional confinement provided by the loading stub at midheight may have created advantageous conditions for ductility. By testing columns with twice the aspect ratio of Gill's and Potangaroa's, the region subjected to high moment would be more extensive and the role of the confining steel would be expected to be more critically tested.

Concurrently, there was a parallel study by T. Zanza on similar sized specimens investigating the influence of laps in the plastic hinge zone which was provided with half of the confining steel required by DZ 3101.

1.4 FORMAT

In Chapter 2, the design and construction of the test specimens are described. Besides the theoretical calculations, the practical aspects of construction and instrumentation will be discussed.

Chapter 3 contains the description of the testing procedures employed which include the design of a new loading frame and the process of specimen installation.

The results and observations of the tests form the contents of Chapter 4. A summary of material properties is included as well.

Chapter 5 presents the discussion and analysis of the results. Comparison with those of Gill's and Potangaroa's studies will be put forward. Confinement for the test columns is compared with requirements from various codes (16,17,18).

Finally some conclusions are drawn and recommendations for future research made in Chapter 6.

The list of references will appear in the Appendix.

CHAPTER TWO

DESIGN AND CONSTRUCTION OF TEST SPECIMENS

2.1 DESIGN OF COLUMN SPECIMENS

The installation in 1978 of the 10 MN Dartec Universal Testing machine at the University of Canterbury had enabled the testing of full size or near full size models of column units in the last two projects (4,5). The same facility was used for the present project which involved similar testing procedures on more slender columns. Fig. 2.1a and Fig. 2.1b show the dimensions of the column specimens tested. The lateral dimension of cross-section was deliberately decreased to 400 mm and the longitudinal dimension increased to 1.6 m in order to achieve a ratio of shear span to member thickness of four which was twice that of the previous two projects. The governing factor for the dimension was the maximum clear height, after making allowance for plates and rollers, available within the Dartec machine. Eventually, an overall length of 3.9 m was adopted and this length gave enough room for rotating the specimen into its vertical position (see Sec. 3.2).

2.1.1 Octagonal Section

(a) Column designation

The columns were numbered according to the sequence at which they were cast and tested.

Two octagonal specimens were designed and detailed for the following axial load levels:

$$\text{Specimen 1 :} \quad \frac{P_e}{f'_c A_g} = 0.12$$

$$\text{Specimen 2 :} \quad \frac{P_e}{f'_c A_g} = 0.53$$

Final levels of axial load provided were calculated and adjusted to give an exact concordance with DZ 3101 confinement requirements, using the actual material strength.

(b) Designed material and section properties

$$\text{Aspect ratio} = \frac{1600}{400}$$

$$= 4 \quad \left(\text{c.f. } \frac{1200}{600} = 2, \text{ Reference 4}\right)$$

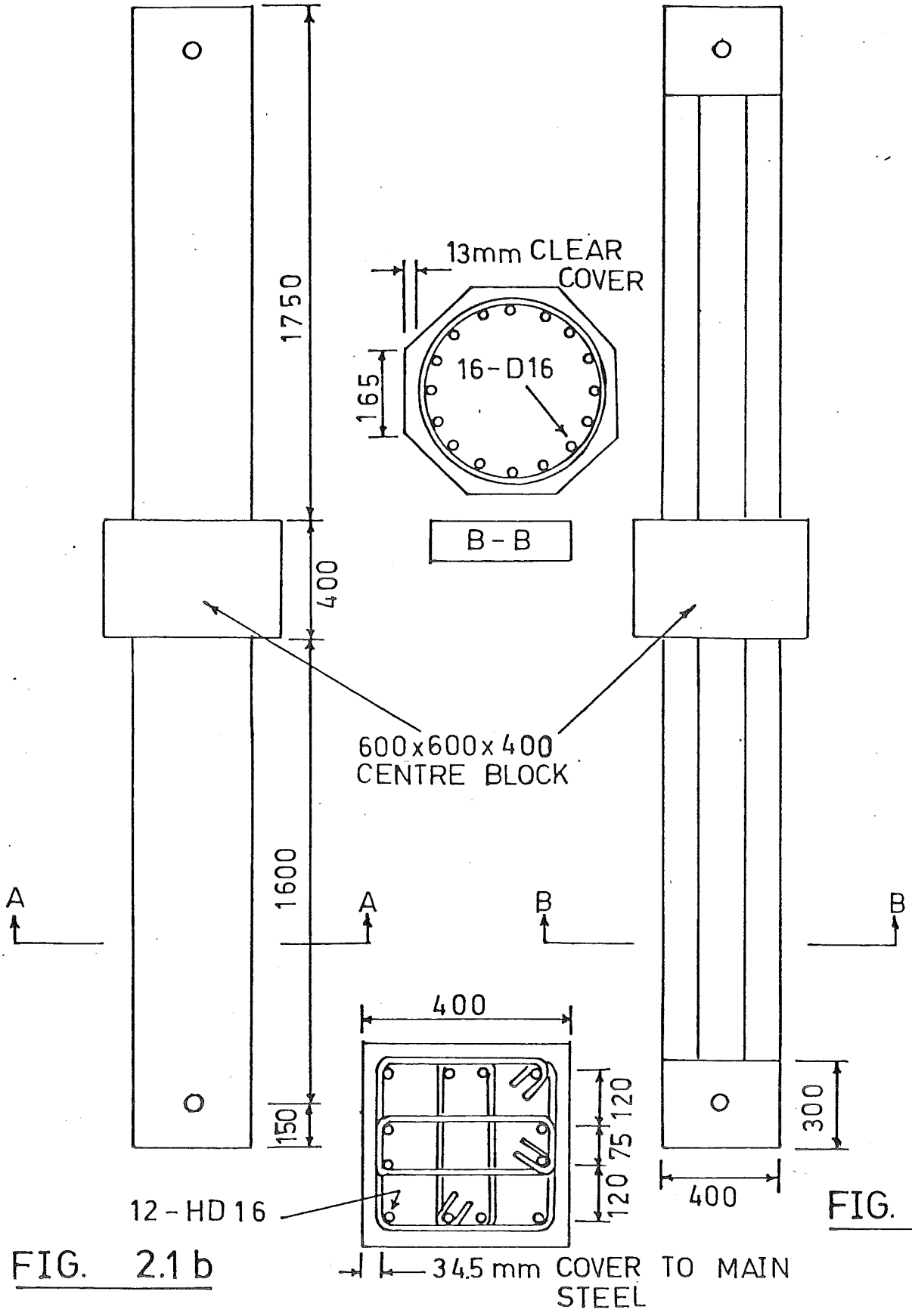

FIG. 2.1 b

FIG. 2.1 c

DIMENSIONS OF SPECIMENS

$$A_g = 132775 \text{ mm}^2$$

$$A_c = 109858 \text{ mm}^2 \text{ (cover = 13 mm)}$$

$$f'_c = 30 \text{ MPa}$$

$$E_c = 4700\sqrt{f'_c}$$

$$= 25.7 \times 10^3 \text{ MPa}$$

$$I_{gross} = \frac{\pi \times 0.4^4}{64} \text{ m}^4$$

$$= 1.2566 \times 10^{-3} \text{ m}^4$$

$$f_y = 275 \text{ MPa nominal}$$

$$f_{yh} = 275 \text{ MPa nominal}$$

(c) Longitudinal reinforcement

Adopting the same amount of steel content as in Potangaroa's specimens, $\rho_t = 0.0243$, the area of longitudinal steel required was

$$(\frac{2}{3})^2 \text{ x area of 16 - D24}$$

$$= 3217 \text{ mm}^2$$

This value gave sixteen D16 bars having the same arrangement as those in Potangaroa's specimens (Fig. 2.1a).

The longitudinal bars were welded to 10 mm end plates at both ends of the specimens to ensure enough anchorage.

(d) Spiral steel ratio

In accordance with Second Draft of DZ 3101 (17), Clause 6.4.4.3 (a-1), the special transverse spiral steel required for confinement in potential plastic hinge when

$$P_e \leq 0.7 f'_c A_g \text{ is}$$

$$\rho_s = 0.45 \left[\frac{A_g}{A_c} - 1\right] \frac{f'_c}{f_{yh}} \left[0.5 + 1.25\frac{P_e}{f'_c A_g}\right] \quad (1)$$

or $$\rho_s = 0.12 \frac{f'_c}{f_{yh}} \left[0.5 + 1.25\frac{P_e}{f'_c A_g}\right] \quad (2)$$

whichever is the greater. The corresponding equations in First Draft (16) were modified to give the above equations which provide some extra confinement at low axial load levels, and compensate for the possibility of the actual value of f'_c significantly exceeding the specified value (2).

Since $0.45 \left[\frac{A_g}{A_c} - 1\right] = 0.09 < 0.12$, Equation (2) governed and accordingly

ρ_s for specimen 1 = 0.00851

and ρ_s for specimen 2 = 0.001522

ρ_s (provided) $= \frac{4 A_{sp}}{d_s S_h}$ where d_s^* = 400 - 2 x 13 mm
= 374 mm

Fig.2.3a gives the details of the amount of spiral steel provided.

* The cover concrete was scaled from 20 mm to $\frac{2}{3}$ x 20 = 13 mm.

(e) Pitch of spiral, S_h

From DZ 3101 requirements, the maximum centre to centre spacing between spirals should not exceed the smaller of

(i) one-fifth of column diameter = $\frac{400}{5}$ mm
= 80 mm

(ii) six times the longitudinal bar diamater = 6 x 16 mm
= 96 mm

or (iii) 200 mm

In Clause 6.4.4.3 (a-3), the third criterion of 200 mm replaces the original requirement of 125 mm (from the first draft of DZ 3101) because it was felt that adequate confinement of the concrete core of columns with diameter less than 1.0 m would be obtained with first criterion of the three (2).

Therefore the maximum allowable pitch for spirals in both specimens was 80 mm.

Over the remaining length of the columns the spacings of spirals were governed by the shear requirements as shown in Fig. 2.3a.

(f) Potential plastic hinge region

According to the code specifications (Clause 6.4.4.1), for specimen 1 where $P_e < 0.3 f'_c A_g$, the potential plastic hinge is taken to be not less than

(i) the diameter of cross-section = 400 mm

or (ii) where the moment exceeds 0.8 the maximum moment at that end of the member = 0.2 x 1600 mm
= 320 mm

Hence, 400 mm governs for specimen 1, and for specimen 2 where $P_e > 0.3\ f'_c\ A_g$, the potential plastic hinge region extends over the region not less than

(i) 1.5 times column diameter = 1.5 x 400 mm
= 600 mm

or (ii) where the moment exceed 0.7 of the maximum moment at that end of the member = 0.3 x 1600 mm
= 480 mm

Therefore, 600 mm governs for specimen 2.

The potential plastic hinge region had been modified from the first draft of DZ 3101 to take into account the greater spread of plasticity under high axial load levels (2).

(g) Shear design

Using the appropriate column design charts of the ACI publication, "Ultimate Strength Design of Reinforced Concrete Columns" (19), the moment capacities of the columns can be determined. The chart values for flexural strength were adjusted to give a capacity reduction factor, ϕ, of unity. 0.75 times the axial loads were input to obtain the chart values of ultimate strength which were then multiplied by a factor of $\frac{1}{0.75}$. The resulting moment was then factored by 1.25 to give the overstrength moment expected from strain hardening and material strength exceeding specified values.

The design shear force was calculated from the computed flexural strength, taking into account the P-Δ effect. Referring to Fig. 2.2, the ultimate moment

$$M_u = \left(\frac{H_u}{2} \times 1.6\right) + P_e \Delta \qquad (3)$$

Therefore $H_u = \frac{M_u - P_e \Delta}{0.8}$ where the value of Δ was obtained using the I_{cr} value. The ultimate design shear force*, V_u, would then be $\frac{H_u}{2}$.

From Second Draft of DZ 3101, Clause 7.4.2, the shear force carried by concrete in potential plastic hinge regions is given by

$$v_c = 4v_b\sqrt{\frac{P_e}{f'_c A_g}} - 0.1 \qquad (4)$$

---

* Since the capacity design approach was used, the strength reduction factor ϕ was taken to be unity and consequently $V_u = V_i$.

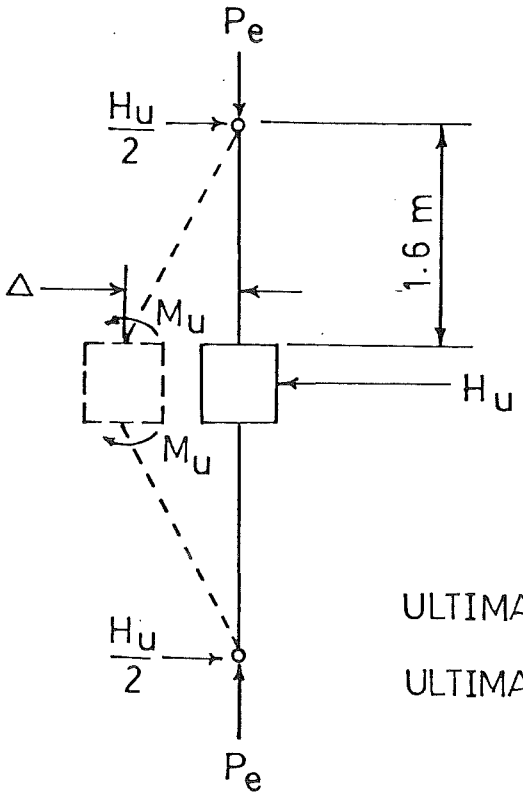

ULTIMATE MOMENT $M_u = \frac{P_u}{2} \times 1.6 + P_e \Delta$

ULTIMATE LATERAL LOAD $P_u = 0.8 (M_u - P_e \Delta)$

FIG. 2.2 PIER IDEALISATION

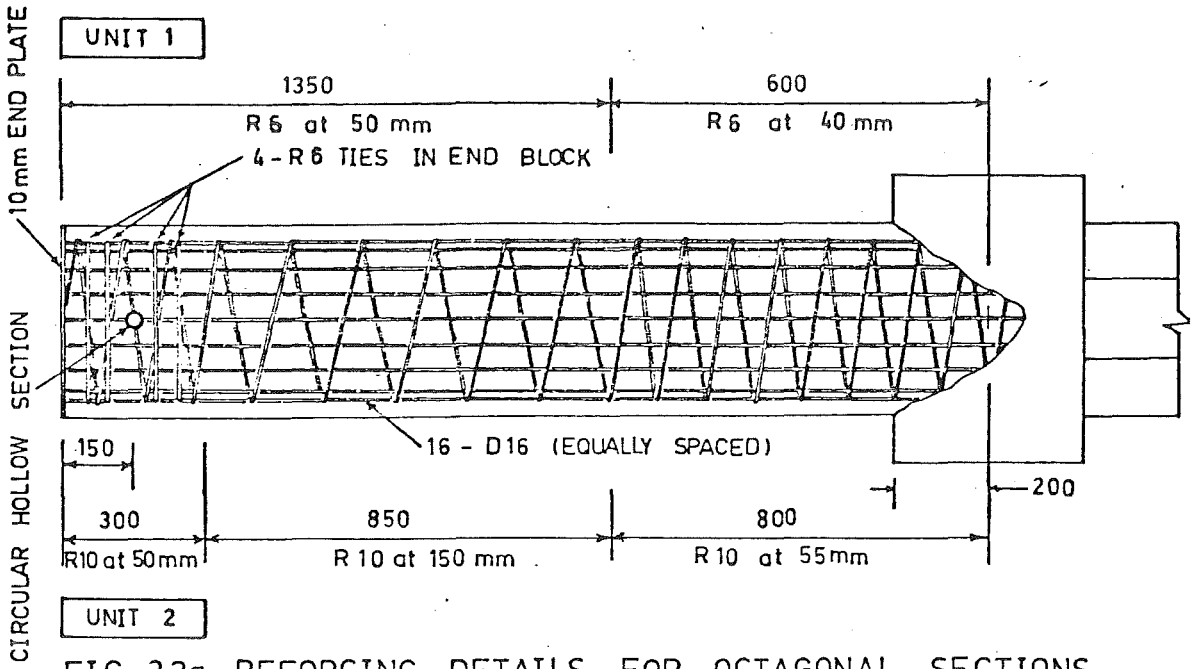

FIG. 2.3a REFORCING DETAILS FOR OCTAGONAL SECTIONS

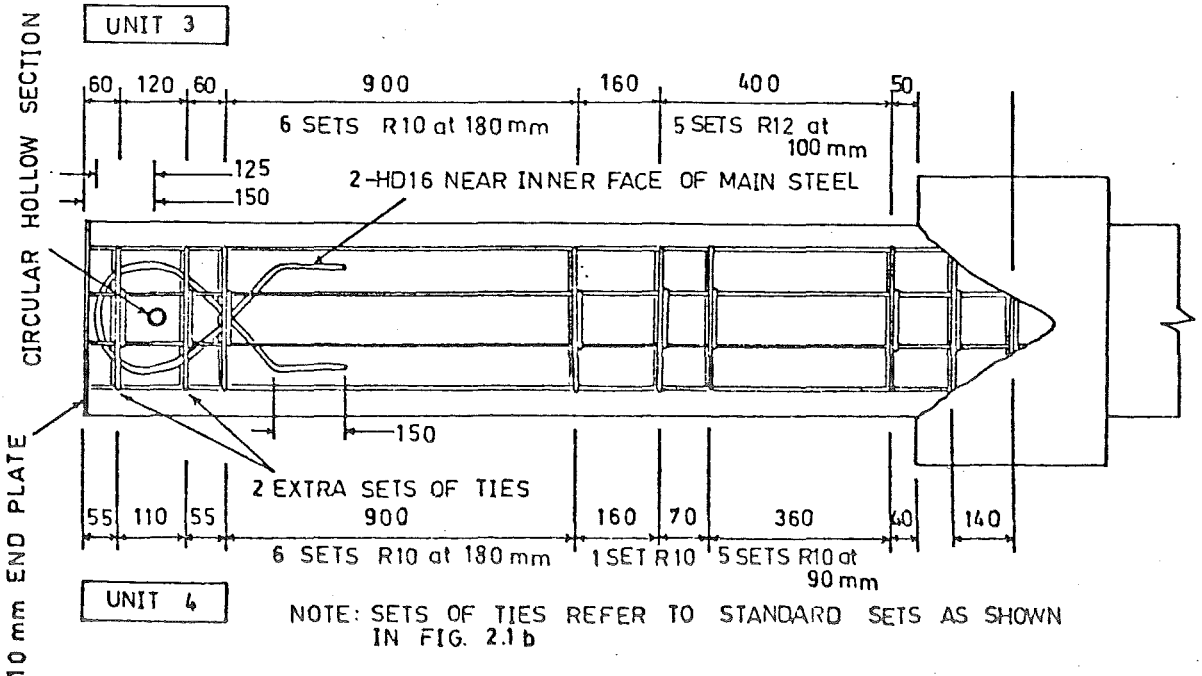

NOTE: SETS OF TIES REFER TO STANDARD SETS AS SHOWN IN FIG. 2.1 b

FIG. 2.3 b REFORCING DETAILS OF SQUARE SECTIONS

where $v_c = 0$ for $\frac{P_e}{f'_c A_g} \leq 0.1$, and

$$v_b = (0.07 + 10\rho_w)\sqrt{f'_c} \quad (5)$$

where $0.08\sqrt{f'_c} \leq v_b \leq 0.2\sqrt{f'_c}$

According to clause 7.4.3.2, Equation (4) applies over the end region which is not less than

(i) the depth of member in the direction of earthquake forces = 400 mm

(ii) one-sixth the height of the member = $\frac{3200}{6}$ mm = 533 mm.

Therefore, for simplicity, it was taken to be valid over a length of 600 mm; equal to the potential plastic hinge region of Specimens 2 and 3.

The rest of the shear force is resisted by the spiral steel, clause 7.2.1.3, i.e.

$$V_s = V_u - V_c \quad (6)$$

provided $v_u - v_c \leq 0.67\sqrt{f'_c}$ (clause 7.2.6.10)

and $v_u \leq 0.8\sqrt{f'_c}$ (clause 7.4.4.5).

Beyond the regions defined by clause 7.4.3.2, shear contribution from concrete is taken to be

$$v_c = \left(1 + 3\frac{P_e}{f'_c A_g}\right) v_b, \text{ (clause 7.2.2.1 (b))} \quad (7)$$

where v_b is as given by Equation (5).

Finally, the shear resistance provided by the spiral steel was calculated using the following equation,

$$V_{s(provided)} = \frac{4}{\pi} \frac{ds}{S_h} A_{sp} f_{yh} \quad (8)$$

and a minimum amount of steel to resist at least 0.35 MPa, clause 7.2.4.3, shear stress is desirable even if it is found to be not required by virtue of Equation (6), i.e. $V_c \geq V_u$.

2.1.2 Square Section

The design for square sections was more or less similar to the octagonal sections. Except where necessary, description is kept to a minimum.

(a) Column designation

To follow up those of octagonal section, the 2 square sections were

Specimen 3 : $\frac{P_e}{f'_c A_g} = 0.38$

Specimen 4 : $\frac{P_e}{f'_c A_g} = 0.21$

(b) Designed material and section properties

Aspect ratio $= \frac{1600}{400}$

$= 4$ (c.f. $\frac{1200}{550} = 2.18$, Reference 5)

$A_g = 160000 \text{ mm}^2$

$A_c = 13201 \text{ mm}^2$, $h'' = 351$ mm (R10 hoops)

$= 126025 \text{ mm}^2$, $h'' = 355$ mm (R12 hoops)

$f'_c = 30$ MPa

$E_c = 4700\sqrt{f'_c}$

$= 25.7 \times 10^3$ MPa

$I_{gross} = \frac{1}{12} \times 0.4^4 \text{ m}^4$

$= 2.1333 \times 10^{-3} \text{ m}^4$

$f_y = 380$ MPa

$f_{yh} = 275$ MPa

(c) Longitudinal reinforcement

Conforming to the requirements as set out in Second Draft of DZ 3101, Clause 6.4.4.2, it was decided to use 12-HD16 bars with the spacing as shown in Fig. 2.1 b. This amounted to a longitudinal steel content, ρ_t , of 0.0151 (c.f. $\rho_t = 0.0179$ of Gill's units).

The anchorage provision was the same as that in octagonal section.

(d) Transverse reinforcement

For similar reasons (3), in clause 6.4.4.3(b), the equations in First Draft were modified to give the following equations:

$$A_{sh} = 0.3\, S_h\, h''\, \left[\frac{A_g}{A_c} - 1\right] \frac{f'_c}{f_{yh}} \left[0.5 + 1.25 \frac{P_e}{f'_c A_g}\right] \quad (9)$$

$$\text{or} \quad A_{sh} = 0.12\, S_h\, h'' \frac{f'_c}{f_{yh}} \left[0.5 + 1.25 \frac{P_e}{f'_c A_g}\right] \quad (10)$$

whichever is greater. In the case under investigation, $0.3 \left[\frac{A_g}{A_c} - 1\right] = 0.09 < 0.12$. Hence Equation (10) governed.

The arrangement of the hoops is summarized in Fig. 2.3b.

(e) Hoop spacings, S_h

Since the same lateral dimension of cross-section and same size of main steel were used, the maximum allowable spacing was still 80 mm. (Sec. 2.1.1 (e)).

(f) Potential plastic hinge region

The criteria for potential plastic hinge region were decided by the length of column and the lateral dimension which were the same in the 2 different sections, hence, for

Specimen 3 : 600 mm

and Specimen 4 : 400 mm (Sec. 2.1.1 (f)).

(g) Shear design

The basic design equations were the same as for spiral steel (Sec. 2.1.1 (g)) except for some small variations in the provision for transverse steel. The value of shear resistance provided by the ties is given by

$$V_s = \frac{A_v f_{yh}}{b S_h} \quad (11)$$

where S_h is limited to be not greater than 0.5d (i.e. about 180 mm) nor 600 mm, Clause 7.2.5.4.(a), and it needs to be halved if $(V_u - V_c) > 0.33\sqrt{f'_c}$, Clause 7.2.5.4 (c).

2.2 CONSTRUCTION PROCESS

2.2.1 Mould Construction

Two plywood moulds were constructed on a steel UB and channel section framework base. The moulds were stiffened with angle sections along the edges and held in position with screws and rods across the top and bottom. (See Fig. 2.4, 2.7 a & b).

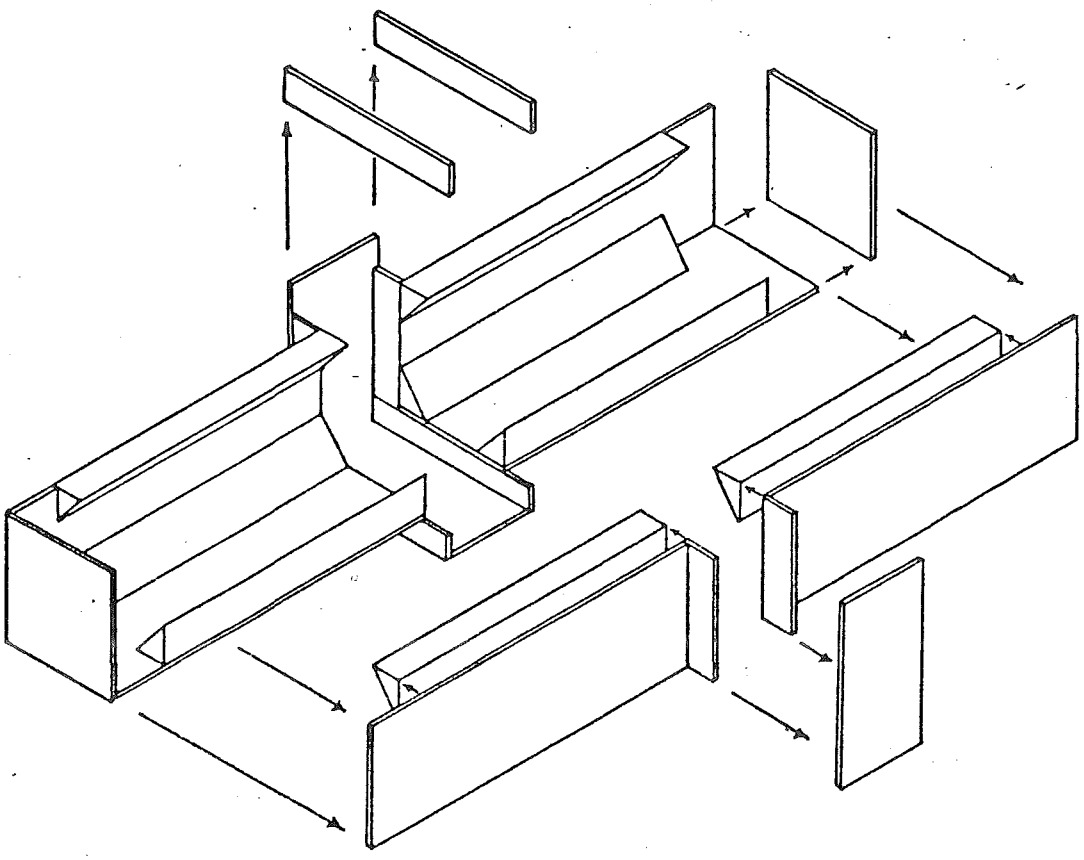

FIG. 2.4 OCTAGONAL MOULD CONSTRUCTION

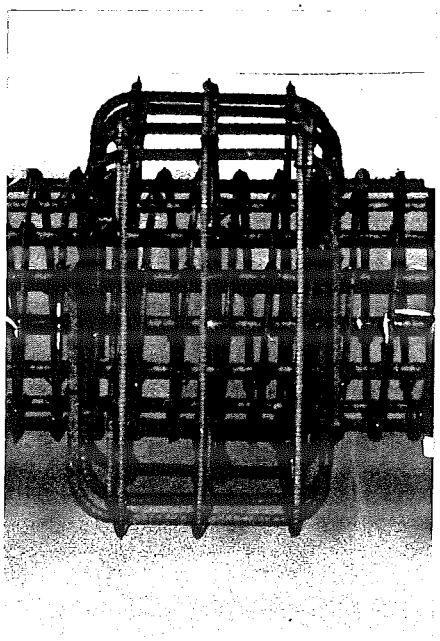

FIG. 2.5 CENTRE BLOCK CONSTRUCTION

The plywood was given a few coats of paint to prevent water absorption during curing. Just prior to placing the concrete any gap along joining edges was sealed with waterproof tape and the mould given a coat of oil to assist stripping of formwork after curing.

In the case of the octagonal section, cardboard was placed over the tight corners to prevent any breaking of these corners during stripping.

2.2.2 Fabrication of Steel Cage

From the experience in fabricating similar specimens in the last two projects, the fabrication process was easily accomplished. The construction sequence started with tying the transverse reinforcement to the main steel, starting from the centre and working out towards the ends. To be efficient time-wise, the main bulk of the reinforcement, i.e. the spirals and hoops, were bent by a steel fabricator outside the University. The longitudinal bars were then welded to the end-plates. The centre block reinforcing cage, Fig. 2.5, was constructed and the steel rods for the dial gauges were positioned and tied. The final procedures included placing the lifting hooks and positioning and welding the steel tubes at their correct locations.

There were some small variations in the construction process for the 2 different sections. For the octagonal specimens, the electrical resistance strain gauges were placed after the spirals were tied in position, whereas the ties of the square sections were strain-gauged before they were placed. Furthermore, to control any excessive cracking of concrete around the 2 reaction pins at the ends, the pitch of the spirals was reduced to 50 mm over a distance of 300 mm at these end regions while 4 additional R-6 ties were included. In the case of square sections 2 α-shaped steel were placed near the inner face of longitudinal bars together with 2 additional sets of ties, one at each side of the pin. (See Fig. 2.6a,b). Finally the spirals were lapped (about 100 mm) and single V flare welded. The ties were not welded.

2.2.3 Placing of Concrete

The completed steel cage was placed in the mould and the holding-rods were tightened to prevent the mould from moving apart during vibration. Where necessary wooden wedges were used for the same purpose. The specimens were cast in the horizontal position (Fig. 2.7a & b) and because of the small opening in the case of octagonal section, a wooden chute was used to aid the pouring process. The concrete was compacted

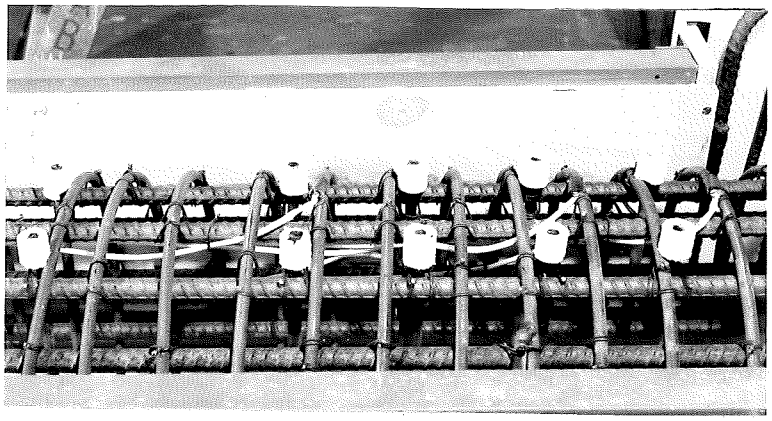

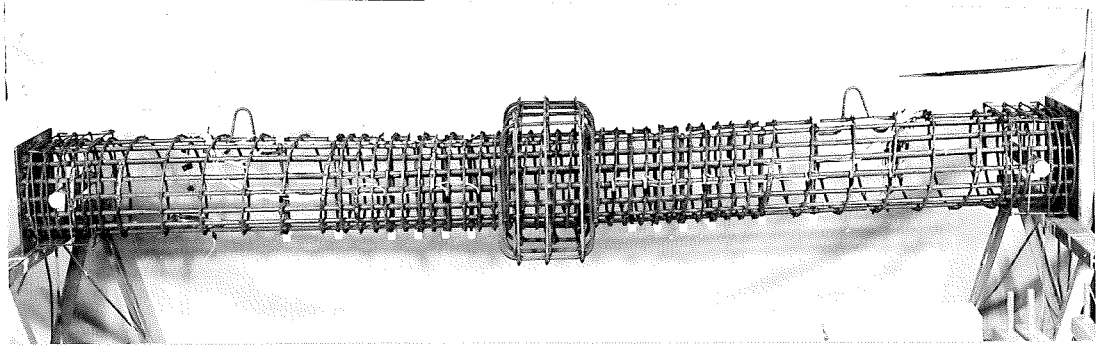

FIG. 2.6 a REINFORCING CAGE (OCTAGONAL)

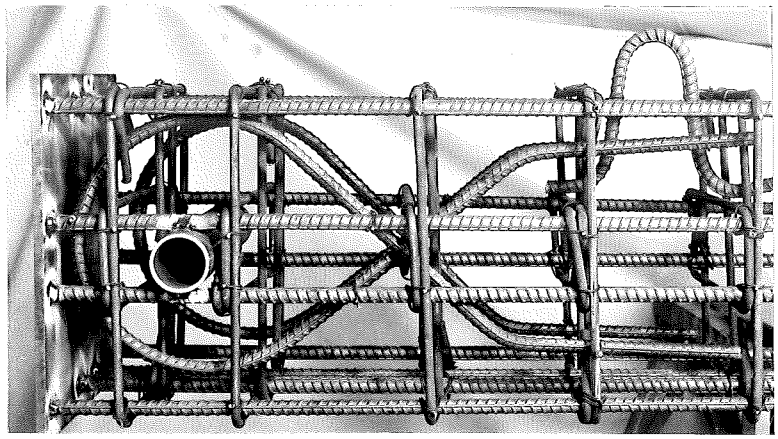

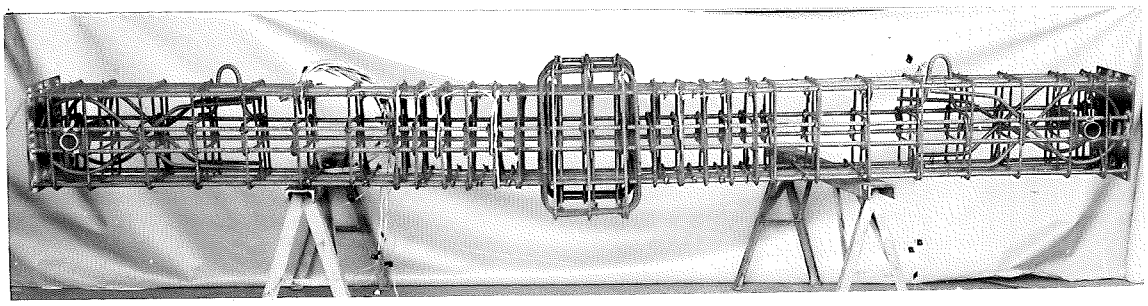

FIG. 2.6 b REINFORCING CAGE (SQUARE)

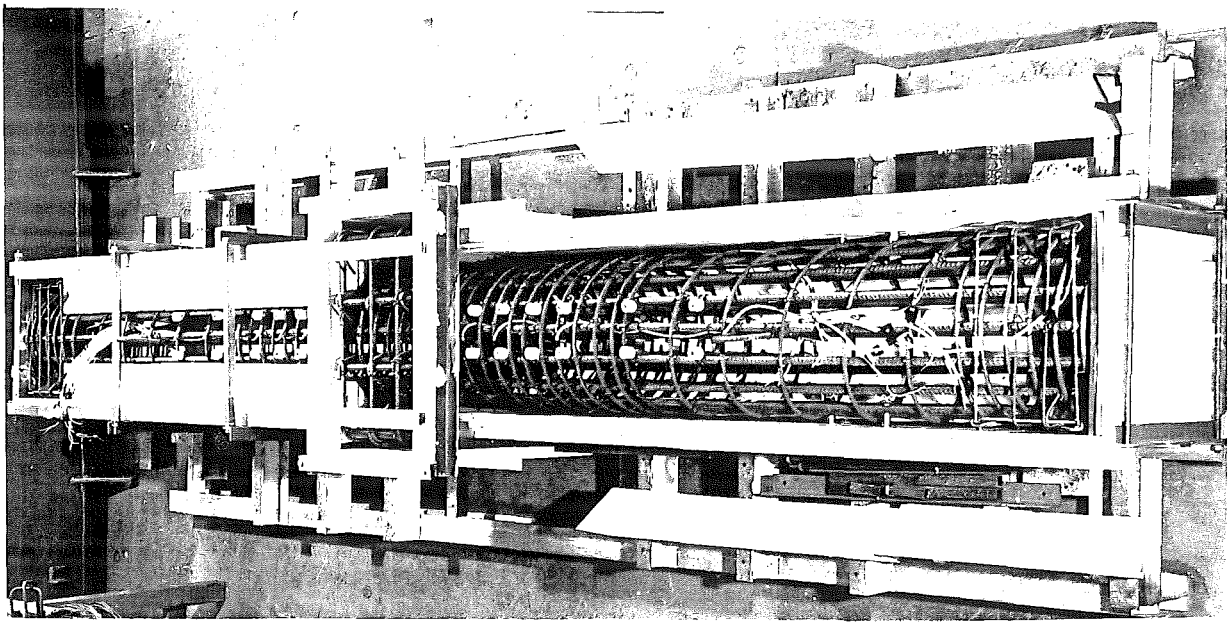

FIG. 2.7 a STEEL CAGE IN MOULD (OCTAGONAL)

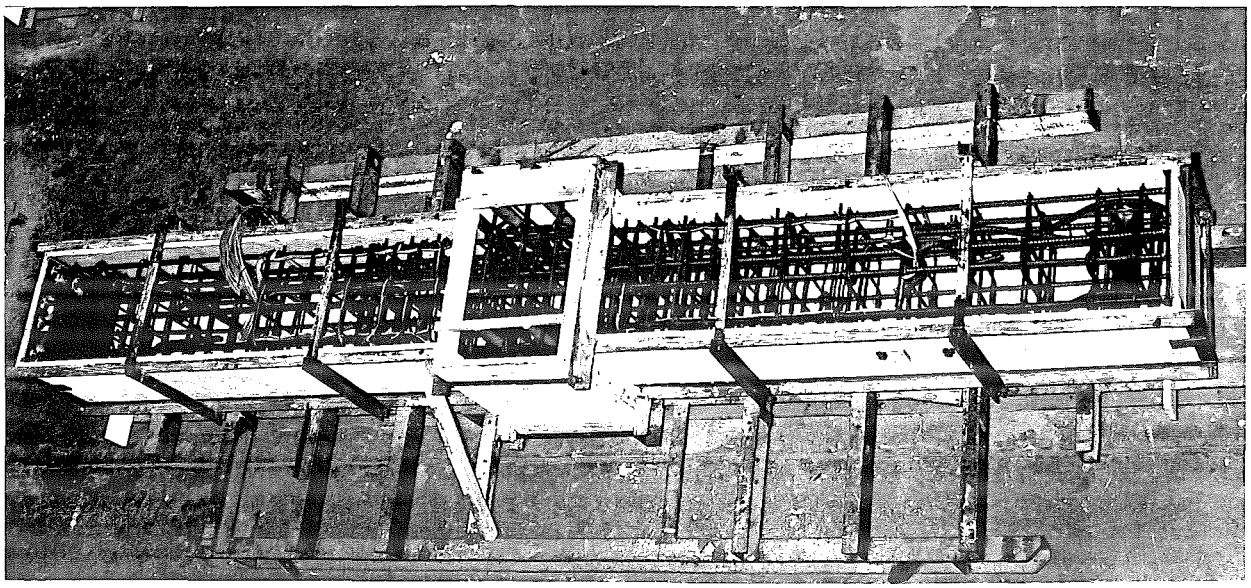

FIG. 2.7 b STEEL CAGE IN MOULD (SQUARE)

and vibrated, then screeded and later on floated. The sides of the mould were lightly tapped to remove any air bubbles trapped under the top slanting sides of the octagonal section to eliminate the occurrence of blow-holes.

After initial set of the concrete has occurred the specimen was covered with damp sacks and plastic sheetings for about seven days before stripping the formwork. After stripping, any blow holes present were plastered and the specimen was given a coat of white paint to facilitate crack identification.

While the concrete was being placed, slump test was carried out to check against that specified in the order and nine standard concrete cylinders were made for later determination of concrete strength.

The concrete was provided by a ready mix contractor and the concrete properties specified were as follows:

Average aggregate size = 20 mm
slump = 75 mm
f'_c = 30 MPa.

2.3 INSTRUMENTATION

2.3.1 Strain Gauges for Measuring Shear, Confining and Longitudinal Strains

Since quite a positive result was arrived at in the previous two projects, it was felt that less extensive strain gauging would be sufficient. In fact, for each column, only one potential plastic hinge region was given a sufficient number of strain gauges to cover the whole area of interest. The other hinge region contained just a few gauges to serve as a check. The identification of strain gauges was done arbitrarily as shown in Fig. 2.8a & b. The strain gauges were numbered from the centre block outwards. No attempt was made to give the check gauges a different labelling system because their number was not large enough to confuse the job.

A new method of strain-gauging to monitor longitudinal strains was tried on specimen 4. In this method two pairs of diametrically opposite strain gauges were mounted on a piece of 8 mm bright plain mild steel rod at 20 mm on each side of the centre point (Fig. 2.9a). The rod was 500 mm long, and threaded over a distance of 90 mm at both ends to provide sufficient anchorage in the concrete. The rod was then "insulated" with a plastic tube of 300 mm over the central portion and the opening ends were sealed up against entrance of moisture. A pair of this set up (Fig. 2.9b) was tied along the centre-line adjacent to

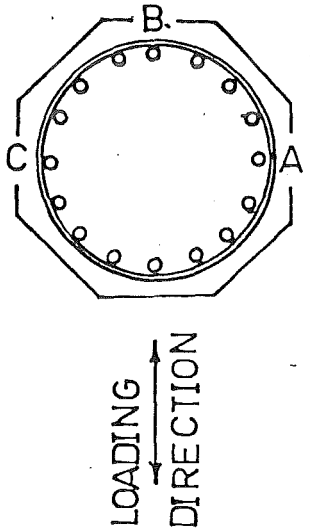

FIG. 2.8a

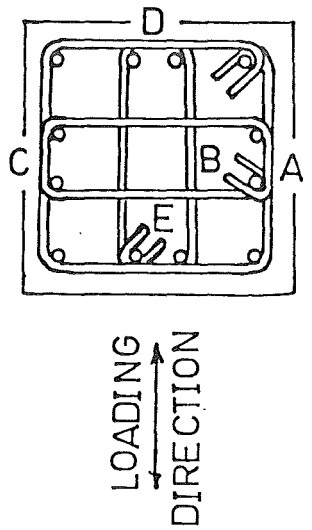

FIG. 2.8b

FIG. 2.8 a & b IDENTIFICATION OF STRAIN GAUGE

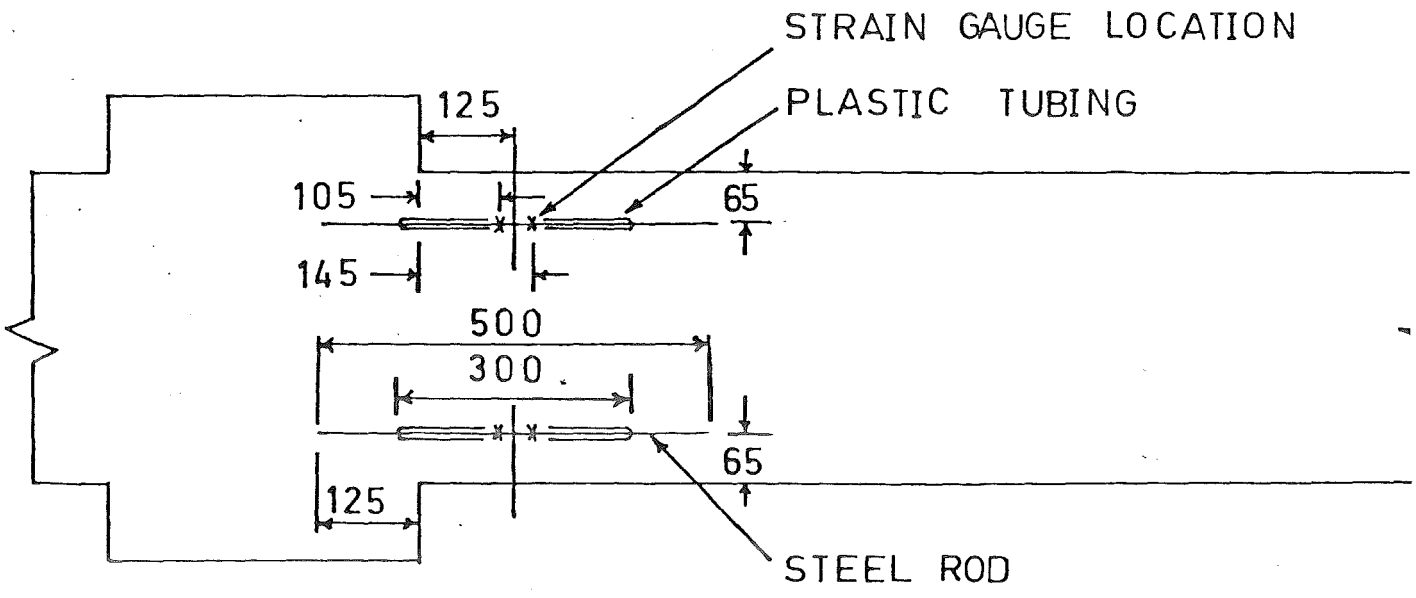

FIG. 2.9a STRAIN GAUGES FOR CURVATURE MEASUREMENTS

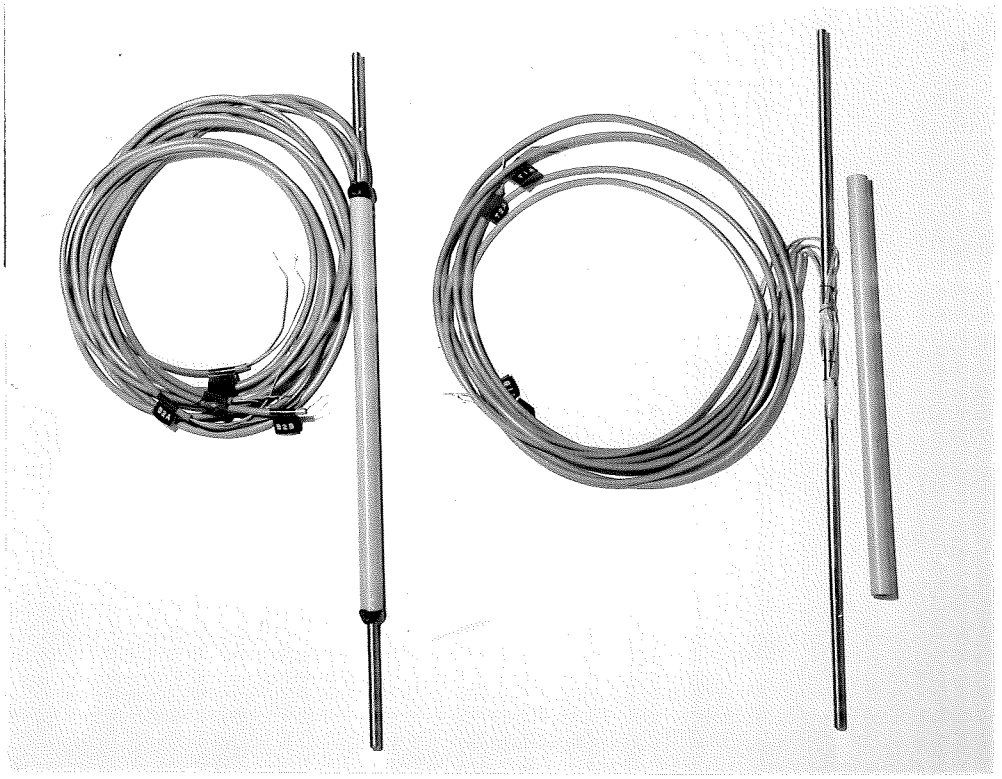

FIG. 2.9 b A PAIR OF THE SET-UP

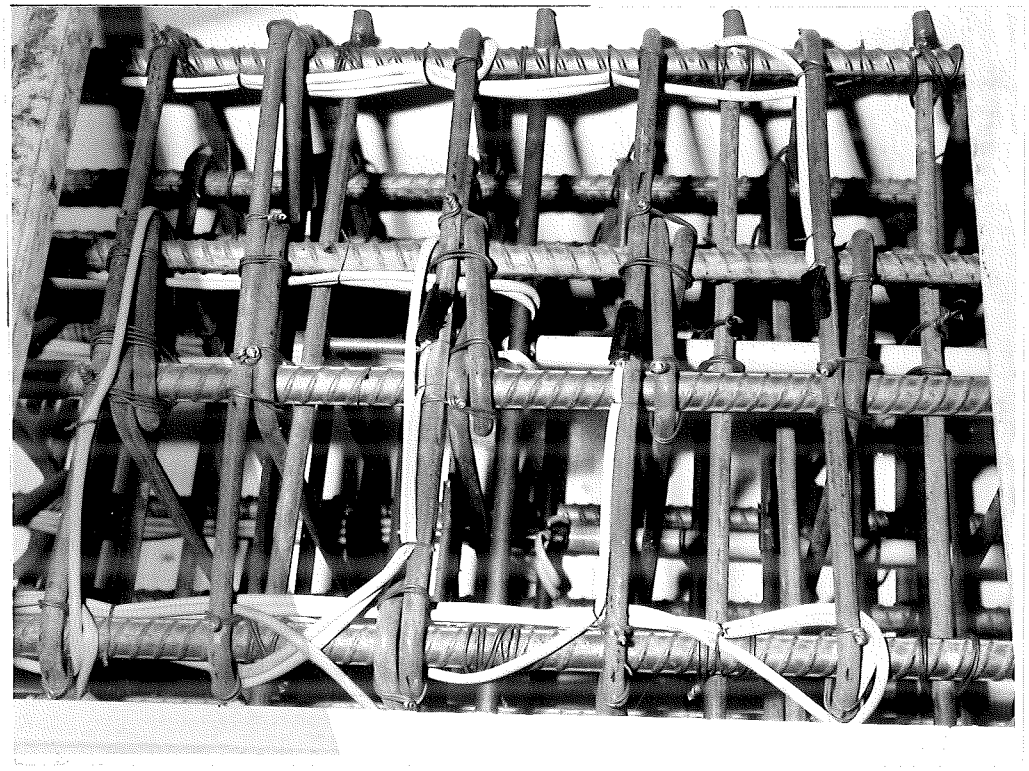

FIG. 2.9 c A CLOSE-UP VIEW

the dial gauge rods on either face in the direction of loading. (See Fig. 2.9c).

The process of applying the electric resistance strain gauges was as follows.

(i) The gauge locations were lightly filed, then smoothed with emery paper and cleaned thoroughly with Methyl Ethyl Ketone (MEK).

(ii) The 5 mm Kyowa KFC-5-C1-11 electric resistance strain gauge was glued using a cyano acrylate strain gauge cement, CC-15A, with the aid of cellotape and light finger pressure.

(iii) The self-adhesive Showa SFG-ST terminal strips were then stuck to the gauge sites.

(iv) The wires, in a protective vinyl tube were soldered on to the terminal.

(v) Several layers of Shinkoh SN/4 water-proofing were applied. They were applied successively one after each previous layer had dried up.

(vi) Finally, a strip of vinyl mastic was placed over the gauge to provide mechanical resistance.

Fig. 2.6a illustrates the finished appearance of some strain gauges.

As mentioned in Sec. 2.2.2, the strain gauging on stirrups was carried out before fabrication so as to avoid difficulty and awkwardness in mounting such strain gauges as B and E (Fig. 2.8b).

The gauge factor for the strain gauge used was 2.1.

2.3.2 Dial Gauges for Measuring Curvature and Longitudinal Strains

The method of mounting the dial gauge frames on the two different sections was identical to that used in the two previous projects respectively. However, in the case of octagonal section, polystyrene pieces were used instead of soft plastic tubing to ensure independent movement of rod outside concrete cover (Fig. 2.6a). Care was taken to ensure that this movement would not be jammed when concrete spalled off during the test.

Except for specimen 1, six dial gauge pairs, the first four at 100 mm increments from the centre block and the next two at 200 mm increments, were placed at opposite faces in the direction of loading along both top and bottom plastic hinge regions. The set-up was the

same for Specimen 1 with the one furthest away from the centre block missing, Fig. 2.10a.

The four dial gauges nearest to the centre block (100 mm away) were 0.01 - 20 mm Mitutoyo gauges and the rest were 0.001 - 0.5" Mercer gauges.

2.3.3 Dial Gauges for Measuring Horizontal Displacement

Some modifications to the previous method of horizontal displacement measurements were made. Only two gauges were used instead of four. Replacing the two end dial gauges, two steel brackets were erected and fixed rigidly to the end blocks. A length of rectangular hollow section was then spanned across these two brackets. It was bolted to the top bracket and was allowed to travel vertically between two smooth rollers at the bottom bracket, Fig. 2.10b. This steel member was considered to be stiff enough to give accurate deflection measurements and not so heavy as to cause additional loading to the specimens. The two 0.01 - 50 mm Mitutoyo gauges were then mounted at the top and bottom edges of the centre block. (Fig. 2.10a).

2.3.4 Linear Potentiometer for Measuring Horizontal Displacement

During the testing of the first specimen, it was found that the two dial gauges for measuring horizontal displacement had to be re-set for ductility factor greater than two. It was troublesome and time consuming to re-set the dial gauges, particularly at higher ductilities, so a further modification was made for this displacement measurement. The two dial gauges were replaced by two 30LP200 Sakae linear potentiometers having a total range of travel of 200 mm (i.e. 100 mm in each direction) and sensitivity 0.04 mm. The dial gauge stand was stiffened with the addition of three bracing members as shown in Fig. 2.10b.

Using the new set-up, the horizontal displacements were obtained, through the digital display unit of a voltmeter, in terms of voltage. These readings were then converted to mm using a calibration factor obtained prior to the testing.

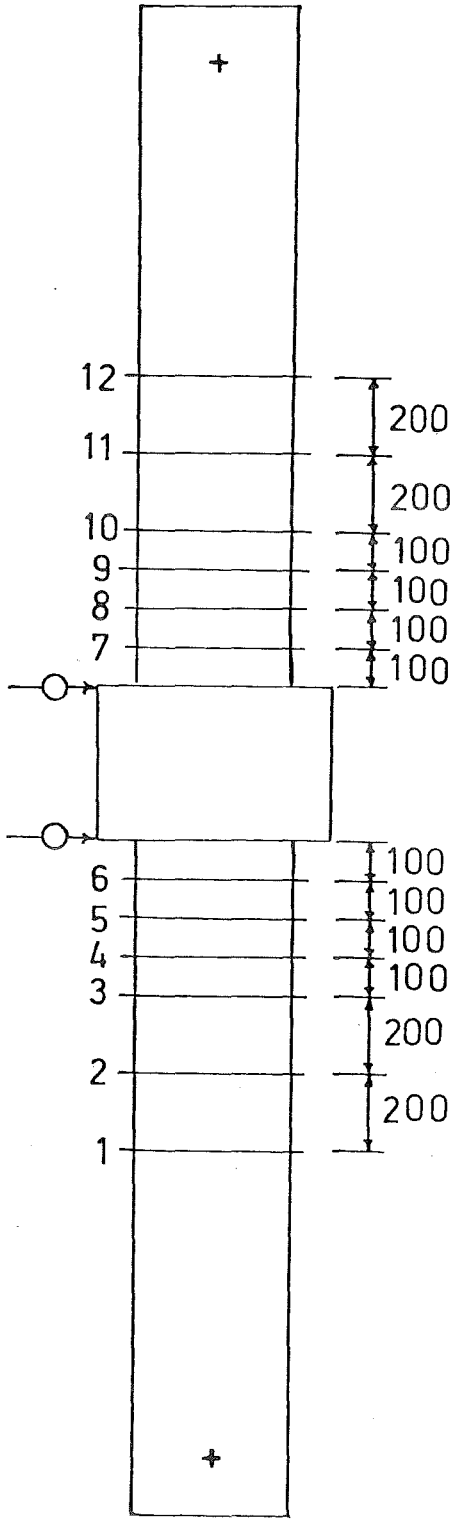

FIG. 2.10a
DIAL GAUGE POSITION

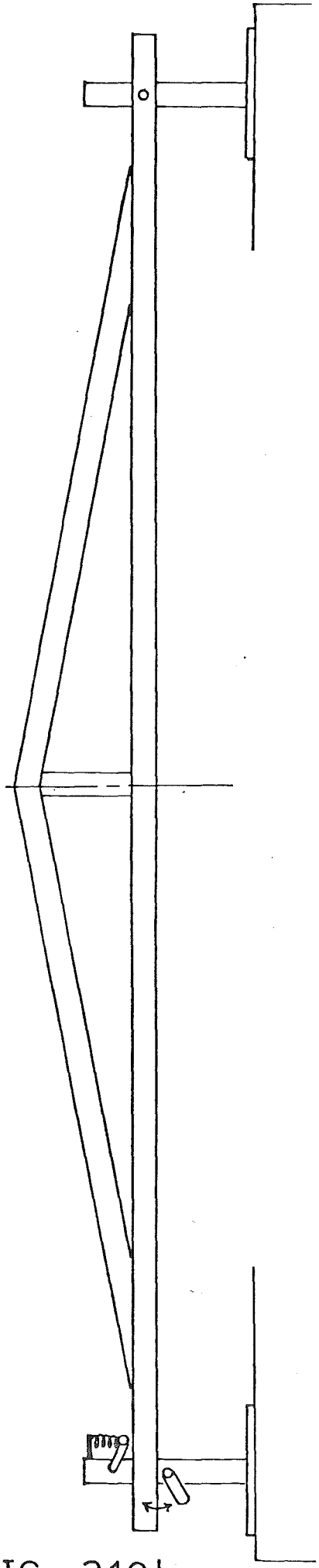

FIG. 2.10b
DIAL GAUGE STAND

CHAPTER THREE

TESTING PROCEDURE

3.1 LOADING FRAME

In view of the difficulty and awkwardness in erecting the existing test frame used for Potangaroa's and Gill's tests, and the cost and time required to extend it to fit the new test specimens, it was suggested that a new frame be built. In order to have an efficient way of applying the dynamic lateral loads, the frame was designed to have two inclined "arms" with the hydraulic jack along the line of angle bisection, Fig. 3.1. The two "arms" were made from 410 UB54 with plates welded at their ends. (For details see Fig. 3.2 a&b). Together with the jack, the two "arms" were connected with a 75 mm steel pin. At both ends of the specimen, a 50 mm steel pin passed through the arms and a steel circular hollow section cast at that end. By pinning the jack at both ends in such an arrangement, there was no danger of bending moment being applied to the specimen by the jack or vice versa. Unlike the previous arrangement, this set-up resulted in less wear and tear at the pins and required little effort in the erection process.

From the consideration of the force diagram Fig. 3.1b, it was evident that the loading pattern would introduce an additional axial component to the specimen. Hence, applied axial load was continuously adjusted during lateral loading to compensate for this effect and maintain the required axial load level.

At the ends a semi-circular steel cylindrical roller was welded to a steel plate which in turn was secured in position between two angle sections welded to the end plate. The matching scalloped plates were bolted to the Dartec loading platform. The roller and the scalloped plate at the ends acted as the axial loading points as well as allowing for the necessary end rotation.

The simulated lateral seismic load was applied through a 500 kN capacity MTS hydraulic jack which was connected to the loading plates via a 38 mm pin. The loading plates were held against the centre block by means of four 25 mm diameter high strength rods threaded through the plastic tubings cast in the concrete and bolted at both ends. The loading frame and the MTS jack were assembled as one unit with minor adjustment of jack level through the slotted hole connection in the two angle sections which kept the jack in position. The load cell was calibrated using an Avery Universal Testing Machine.

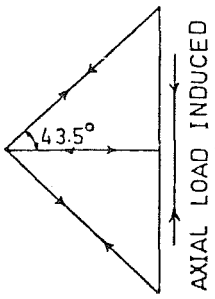

FIG. 3.1b FORCE DIAGRAM

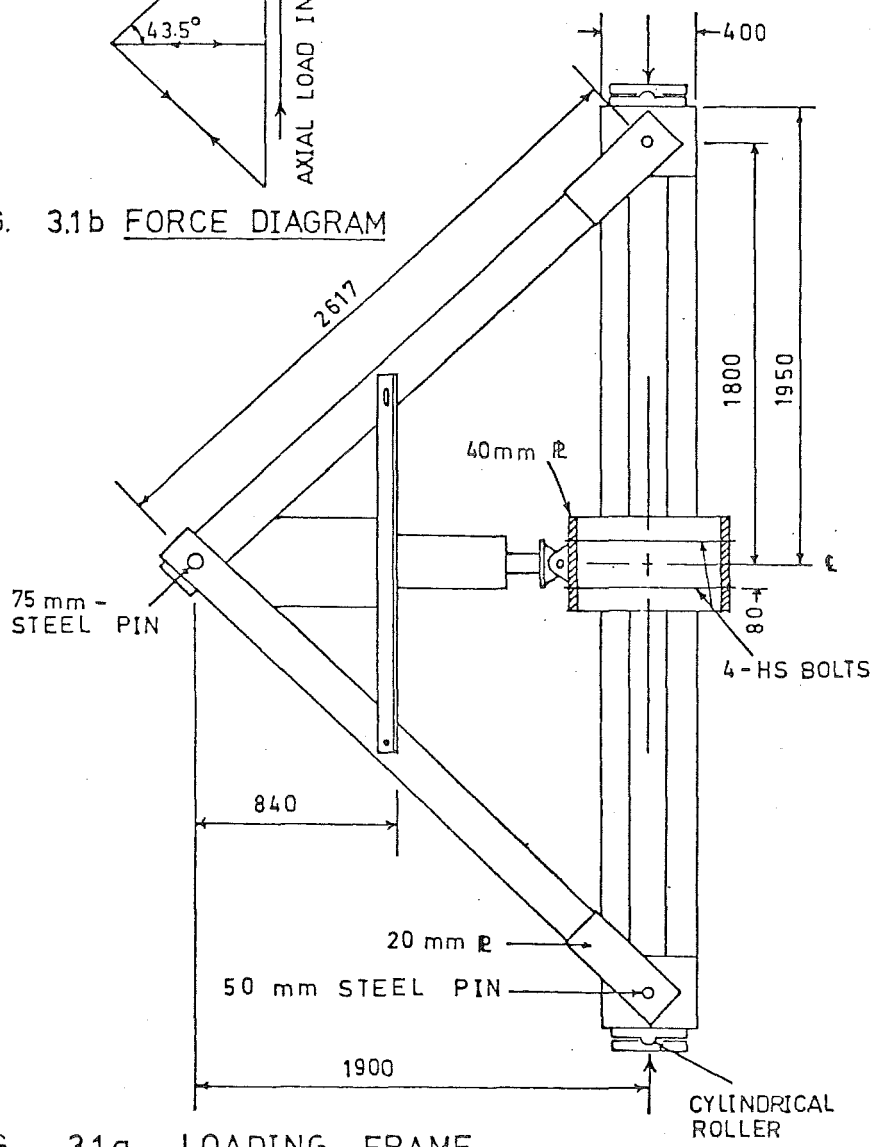

FIG. 3.1a LOADING FRAME

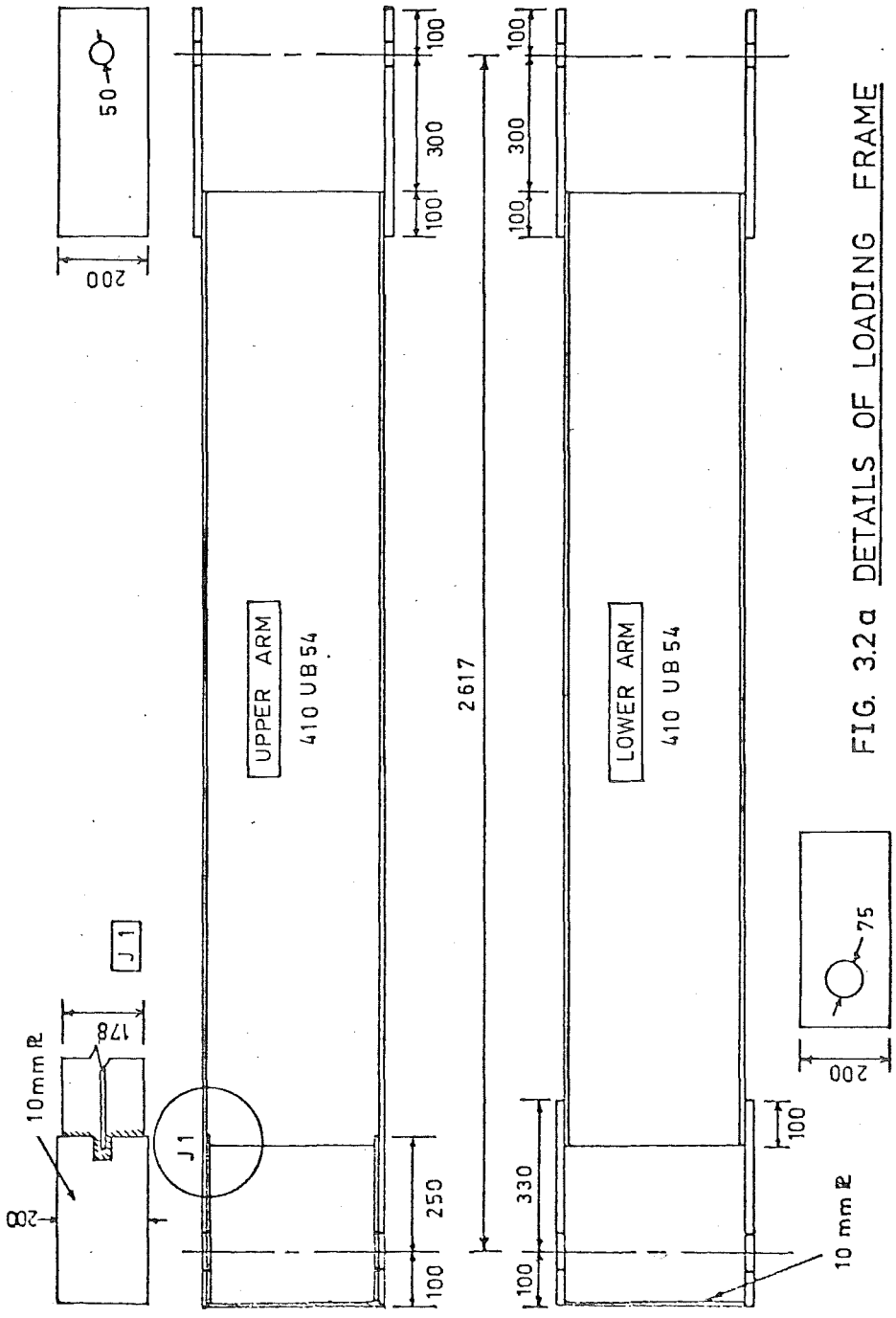

FIG. 3.2a DETAILS OF LOADING FRAME

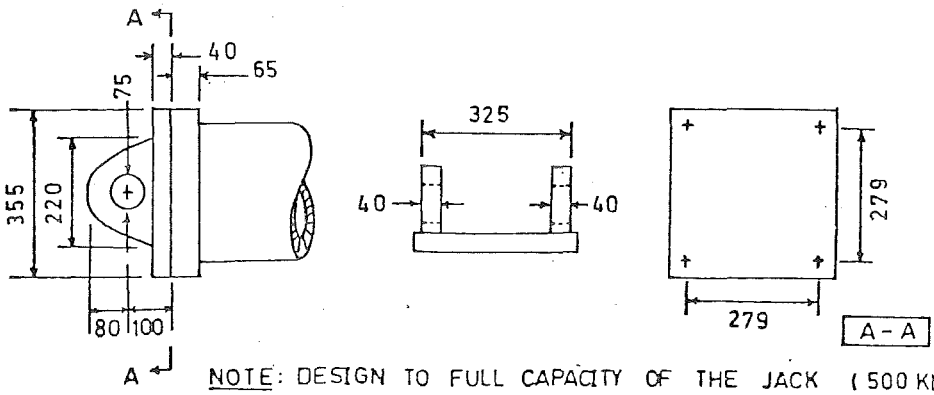

NOTE: DESIGN TO FULL CAPACITY OF THE JACK (500 KN)
USE 6 mm FILLET WELD FOR ALL CONNECTIONS

FIG. 3.2b

3.2 SPECIMEN INSTALLATION

Since the new loading frame occupied only one side of the test machine time was saved because there was no need to dismantle the frame to make way for the specimen during installation.

The column specimen was first aligned with the test machine and placed over a pair of trolleys. The column was then manually pulled towards the machine along a steel plate path used to protect the laboratory floor. Once the top end of the column was under the machine, two 3-tonne chain-block hooks permanently fixed to the cross head of the machine were attached to the lifting brackets near the top end of the specimen. The column was then winched and rotated into its vertical position with the bottom end riding in freely on its trolley. The bottom pair of rollers and scalloped plate was then fixed while the specimen was suspended by the chain-blocks. The top pair were fixed before the specimen was pulled into position. The plates were then adjusted and plastered. A small axial load was used to hold the machine while the loading frame-hydraulic jack unit was lifted and pinned to the specimen. When the process of installation was completed the chain-blocks were left suspending the frame and holding the specimen but they were slackened during testing.

3.3 TESTING PROPER

Just prior to commencement of testing, compression tests were carried out on the concrete cylinders to determine the as-tested concrete strength. Using the available data on material properties and reinforcing details the axial load was then adjusted to give the required level as governed by Cl. 6.4.4 of Second Draft of DZ 3101. As it was mentioned in Sec. 3.1, this axial load level was maintained by adjusting the applied axial load before every lateral load increment. However, this adjustment was not possible in the case of dynamic loading during the final part of the testing procedure. This discrepancy was taken into account in later analysis.

The lateral load was applied by a 500 kN capacity double acting MTS hydraulic jack operated by a servo-hydraulic closed-loop control system. Loading was under displacement control, with load being monitored by a straingauged load-cell between the jack and test specimen. Maximum velocity of ram operation was controlled by the size of the pumping unit [20 US gal/min] to 64 mm/s.

The horizontal static load sequence followed the same pattern used in previous projects. The initial horizontal load cycle to 75 per cent of

the predicted yield load was used to establish the first yield displacement, Δ_y . (For detailed computation refer to Chapter 4). Subsequently, two complete cycles to displacement ductility factors of two, four and six were carried out in turn. For ductility factor of eight, three complete cycles were carried out to check on any obvious strength and stiffness degradation, Fig. 3.3. This was followed up by dynamic loading to at least ten cycles of loading at the same ductility factor. The dynamic load was applied sinusoidally with a frequency of 0.13 Hz and the hysteresis loops of lateral load vs deflection were obtained on the HP X-Y plotter.

During each cycle of static loading, the initial part was controlled by load increments to some load level close to the theoretical ultimate load (neglecting the $P-\Delta$ effects) and then by displacement increments to the pre-determined value of ductility factor. Only the two horizontal displacement transducers were read at every increment. The complete set of readings (including strain gauge readings) was taken at each increment during the initial cycle and only at every new load level during subsequent cycles.

At the peak of each load cycle, both negative and positive peak values, all the cracks were marked and photographed.

During the later stage of laboratory testing, the dynamic cycles were filmed using a movie camera. This ensured a permanent record of the dynamic testing.

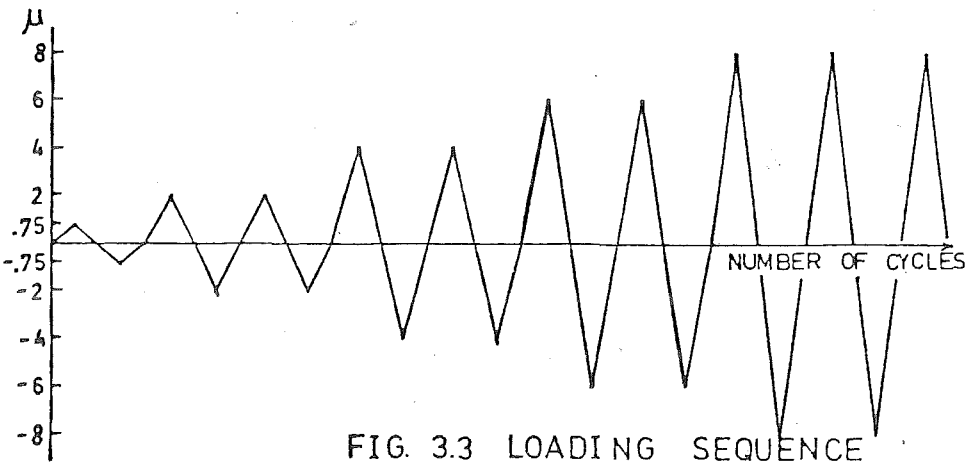

FIG. 3.3 LOADING SEQUENCE

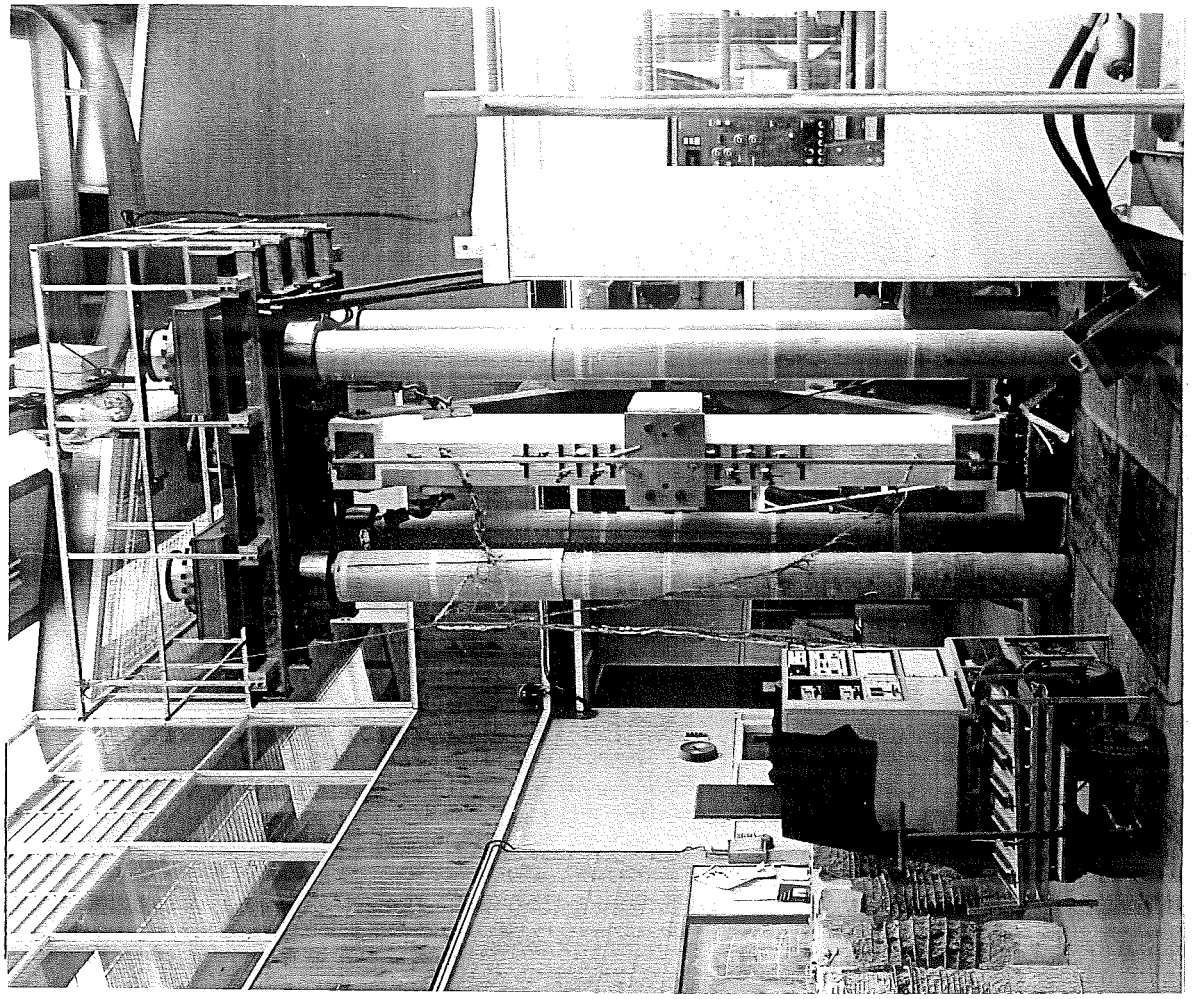

FIG. 3.4a GENERAL VIEW OF TEST SET-UP

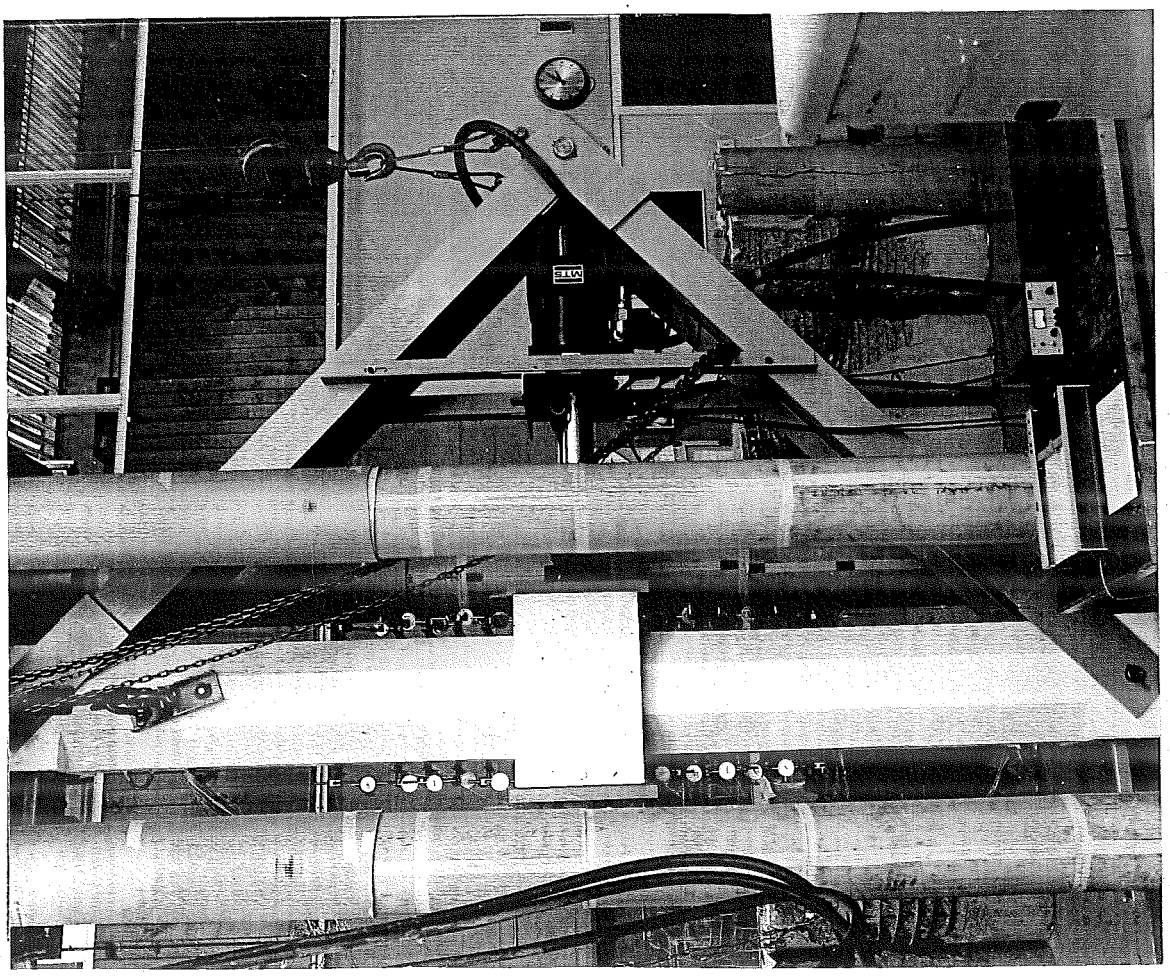

FIG. 3.4b GENERAL VIEW OF TEST SET-UP

CHAPTER FOUR

RESULTS AND OBSERVATIONS

4.1 SUMMARY OF MATERIAL PROPERTIES AND TEST UNIT DETAILS

Figs. 4.1a-d show the stress-strain curves for the reinforcing steel used. The average of three tests for every bar size was taken as representative. All the steel specimens tested showed a significantly higher yield strength than the specified values. The high strength steel showed a shorter yield plateau but considerably more stress increase during strain hardening than the mild steel. In the case of specimens of spiral steel which had been straightened after forming, since they had been yielded twice, the tensile tests did not give a definite yield point or yield plateau. Hence the test results from initially straight pieces were used for the calculations. Unfortunately, the complete stress-strain curve to failure was not obtained and consequently steel stresses for strains higher than 0.05 have to be estimated.

The test unit details are summarised in Table 4.1. For all units, the concrete strength was lower than the specified f'_c of 30 MPa. As discussed in Section 2.1.1(a), the actual axial load levls provided in the tests were to be adjusted to give an exact concordance with the DZ 3101 transverse steel requirements using the actual material properties. This was carried out in the first test and there was a considerable change in the axial load applied (from 0.12 $f'_c A_g$ to 0.2 $f'_c A_g$). Hence it was decided to maintain the original design axial load obtained for specified strength and to tolerate the difference between required and provided transverse steel content. For example, in Unit 2, design axial load $P_e = 0.53\ f'_c A_g$

Therefore, $P_e = 0.53 \times 30 \times 132.775$ kN

$= 2111$ kN

Actual f'_c at time of testing unit = 28.5 MPa

$$\therefore \frac{P_e}{f'_c A_g} = \frac{2111}{28.5 \times 132.775} = 0.56$$

and when substituted into Equation (2), it gave a required spiral steel content of 0.01466 which was 96% of the $\rho_s = 0.01527$ actually provided.

TABLE 4.1 : TEST UNIT DETAILS

UNIT	Concrete Strength f'_c (MPa)	Axial Load P_e (kN)	$\frac{P_e}{f'_c A_g}$	Longitudinal Reinforcement		Transverse Reinforcement			
				ρ_t %	Yield Strength f_y (MPa)	diameter d_s (mm)	spacing s_h (mm)	volumetric ratio, ρ_s (%)	yield strength, f_{yh} (MPa)
1	26.0	680	0.20	0.0243	308	6	40	0.00756	308
2	28.5	2111	0.56	0.0243	308	10	55	0.01527	280
3	23.6	1435	0.38	0.0151	427	12	100	0.02832	320
4	25.0	840	0.21	0.0151	427	10	90	0.02218	280

Note ρ_s required by Second Draft of DZ 3101 for Units 1 and 2 are 0.00760 and 0.01466, respectively and for Units 3 and 4 are 0.01918 and 0.01823, respectively.

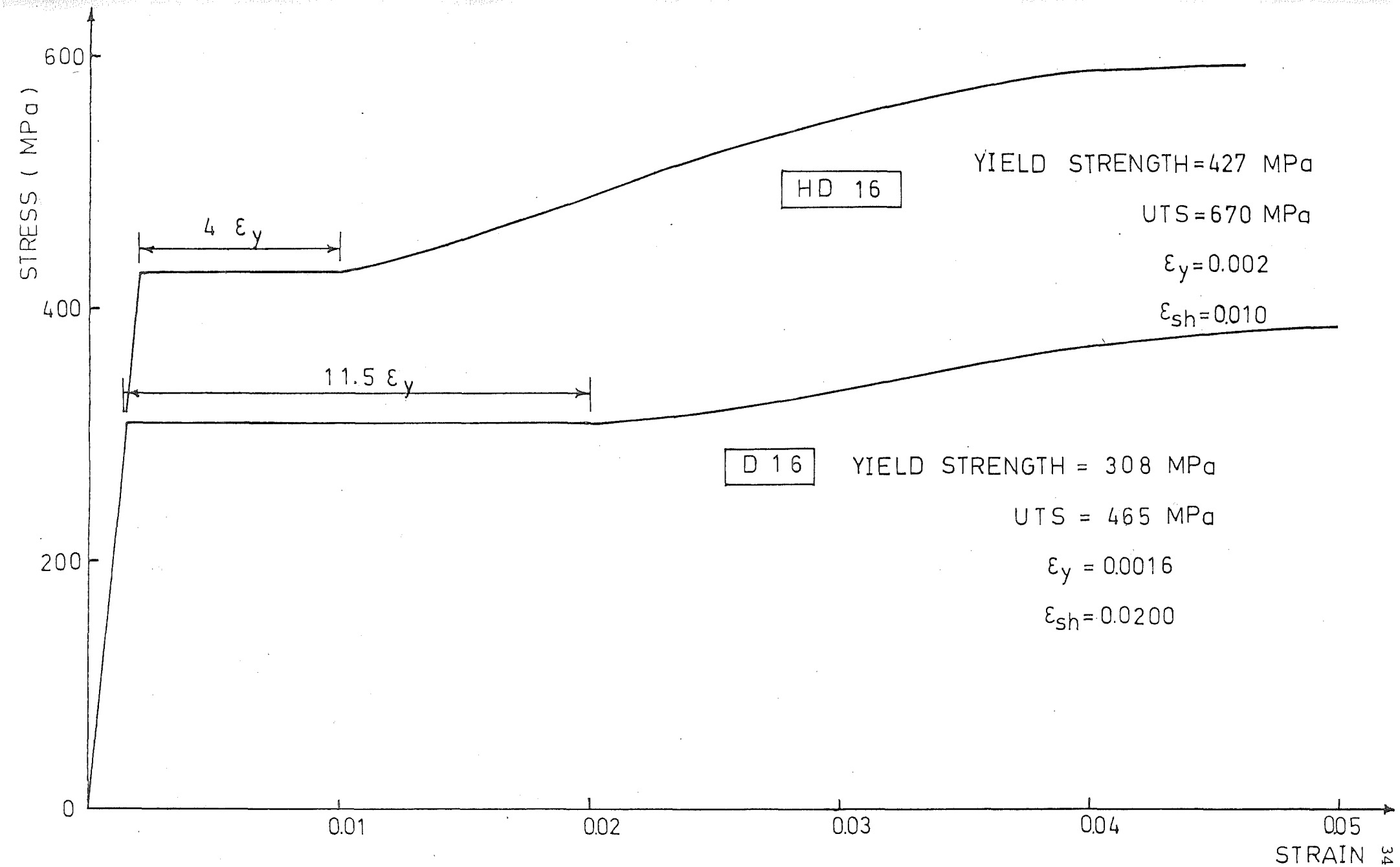

FIG. 4.1a STRESS-STRAIN CURVE FOR D16 & HD16 STEEL

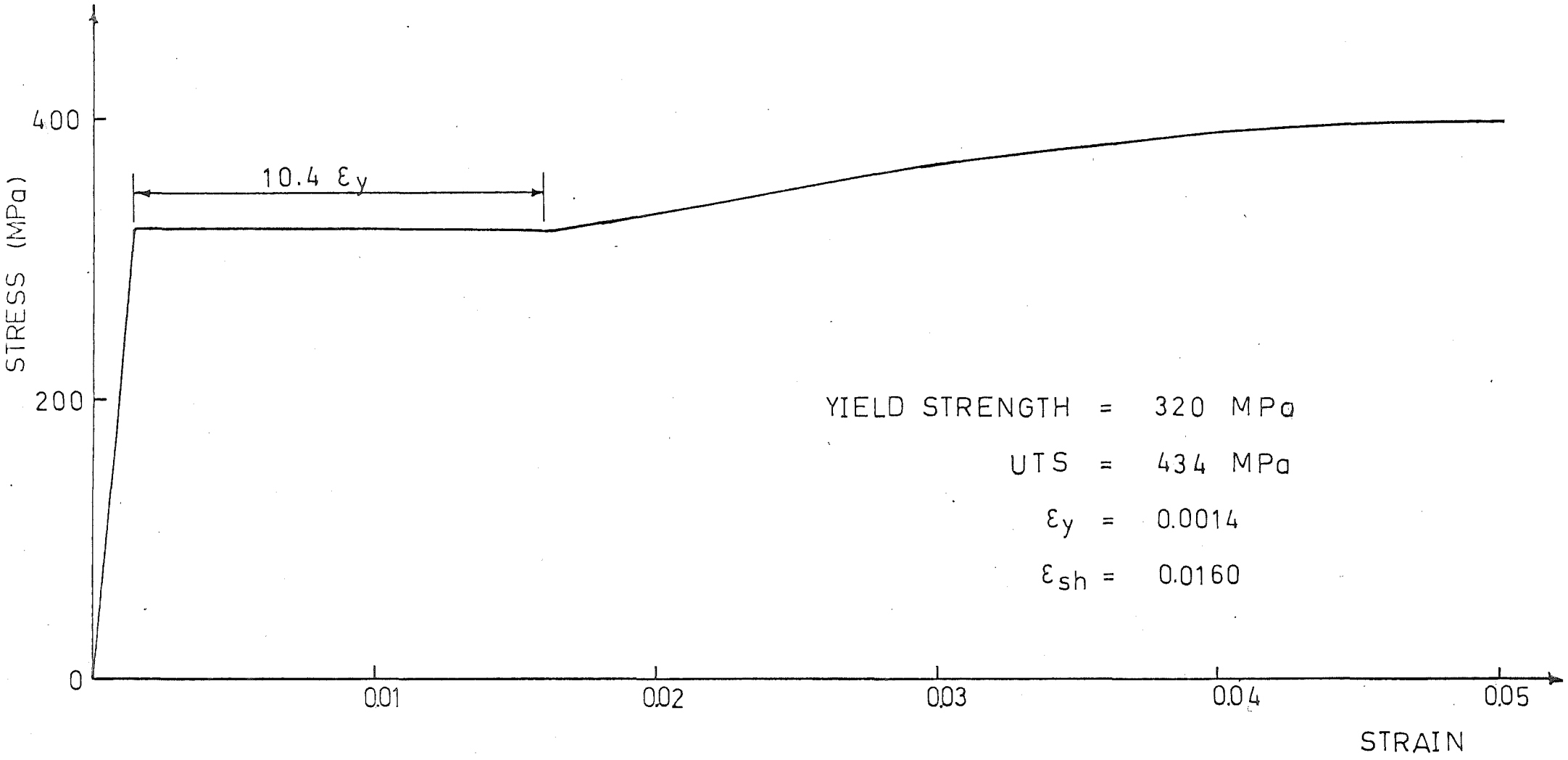

FIG. 4.1b STRESS-STRAIN CURVE FOR R12 STEEL

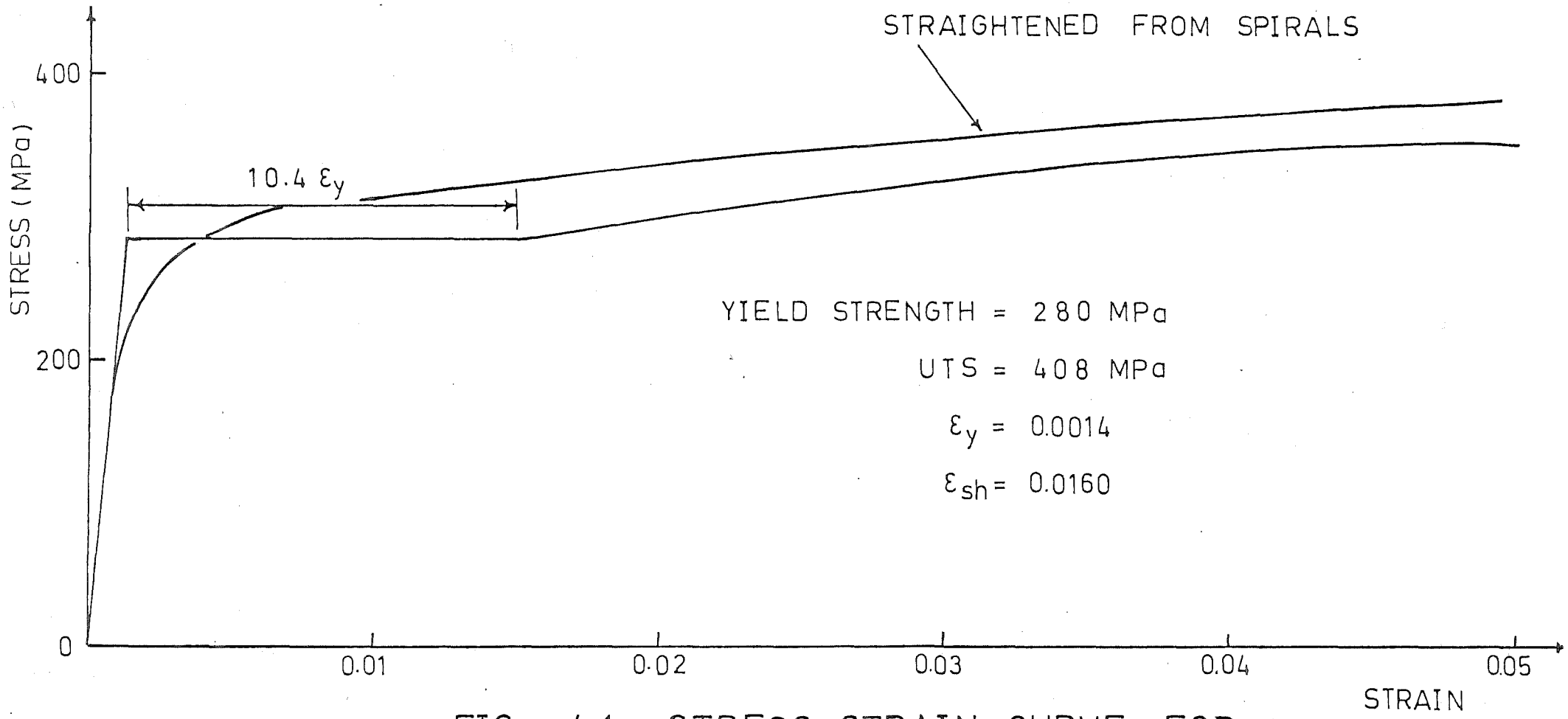

FIG. 4.1c STRESS-STRAIN CURVE FOR R10 STEEL

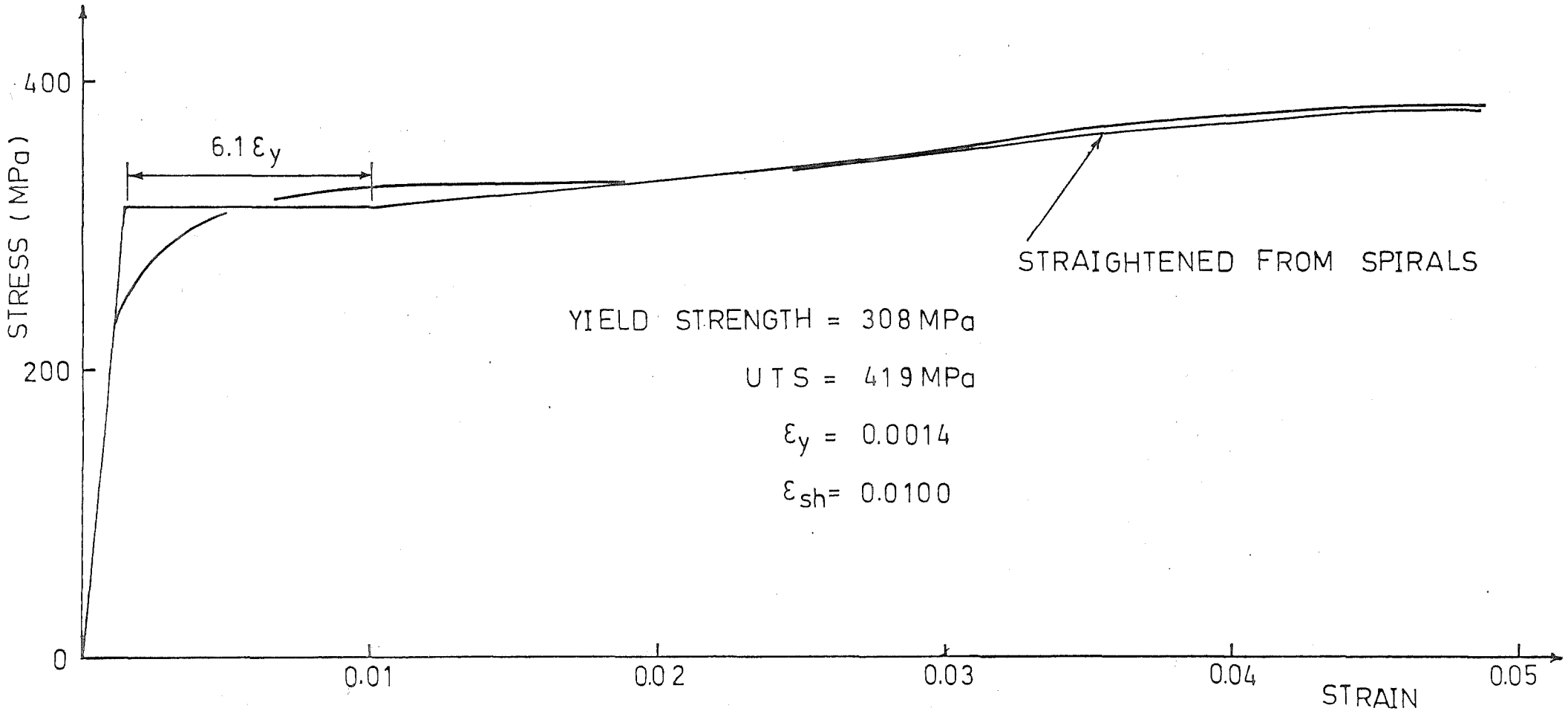

FIG. 4.1d STRESS-STRAIN CURVE FOR R6 STEEL

However, in the case of the square sections, due to the incorrect values of f'_c being used in calculating P_e, the actual P_e/f'_cA_g values were significantly lower than they should have been for exact concordance with the DZ 3101 transverse steel requirements. For example, in Unit 3

$$\text{Actual } \frac{P_e}{f'_cA_g} = 0.38$$

and when substituted into Eq. (10) it gave a required transverse steel content of 0.01918 which was 68% of the $\rho_s = 0.02832$ actually provided.

Similarly, in Unit 4,

$$\text{Actual } \frac{P_e}{f'_cA_g} = 0.21$$

and when substituted into Eq. (10) it gave a required transverse steel content of 0.01823 which was 82% of the $\rho_s = 0.02218$ actually provided.

4.2 RESULTS AND OBSERVATIONS

The following sections deal with the results and observations of individual test unit. Included in each section are the following aspects:

(a) the general description of the behaviour of the piers during testing,

(b) the derivation of yield displacement and yield curvature,

(c) lateral load-lateral displacement relationship, including dynamic test results,

(d) curvature profiles as well as curvature ductility factor,

(e) transverse steel strains, i.e. both confining and shear induced strains,

(f) maximum concrete compressive strains,

(g) equivalent plastic hinge lengths, and

(h) idealized stress-strain curve for the confined concrete core.

For the convenience of comparison and discussion, a summary of these results is presented in Chapter 5, and to differentiate from the μ values for individual hinge, the overall values were taken as μ_o.

4.2.1 Specimen One

(a) General description

In the elastic cycle, the lateral loading sequence was 50 kN, 100 kN, 140 kN and then 172 kN. All the subsequent cycles had 50 kN increments until the loading was controlled by predetermined displacements (i.e. μ_o= 1, 1.5, 2, 2.5 and so on).

Flexural cracks started to appear after the second load increment in the elastic cycle. At μ_o= 2 , these cracks deepened and showed inclination. During further loadings, they widened and crossed each other and the cracking extended to almost two-thirds of each column height.

No sign of crushing was observed until the specimen was displaced to μ_o= 2 . Concrete crushing became more extensive at bottom plastic hinge in later cycles. This resulted in the bottom plastic hinge undergoing more plastic rotation than the top, as demonstrated by the tilting of centre block (Fig. 4.2 a&c). Hence, the overall values of μ_o= 2, 4, 6 and 8 came more from the plastic rotation of the bottom hinge than from the top hinge. At μ_o= 4, crushing of concrete extended to about 200 mm from the centre block. At failure the spalling of concrete cover had occurred right back to the longitudinal bars.

The longitudinal steel showed signs of buckling when the unit was loaded to the third cycle of μ_o= 8. The unit finally failed by the fracture of these longitudinal bars and spiral steel in the bottom plastic hinge after 10 additional dynamic cycles at μ_o= 8 . (Fig. 4.2 a& b).

(b) Yield displacement and yield curvature derivation

The yield displacement for the specimen was determined by extrapolating the straight line joining the origin and 75% of the theoretical ultimate load on the load-displacement curve to the theoretical ultimate load of the column, taking into account the P-Δ effect. The average value of both the positive and negative cycles was taken as representative. This experimentally determined yield displacement was 7.5 mm as compared with the theoretical value of 5.1 mm computed using the I_{cr} value from the transformed section assuming a modular ratio of n = 10 and a triangular M/EI_{cr} distribution diagram.

The yield curvature (Fig. 4.3) for the individual plastic hinge regions were obtained experimentally in the same manner as the yield displacement, (Fig. 4.2), and were found to be about twice the value (8.8×10^{-6} rad/mm) calculated theoretically using the triangular bending moment distribution for cantilever, i.e.

$$\Delta_y = \left(\frac{1}{2} \times 1.6 \times \phi_y \right) \times \frac{2}{3} \times 1.6 \qquad (12)$$

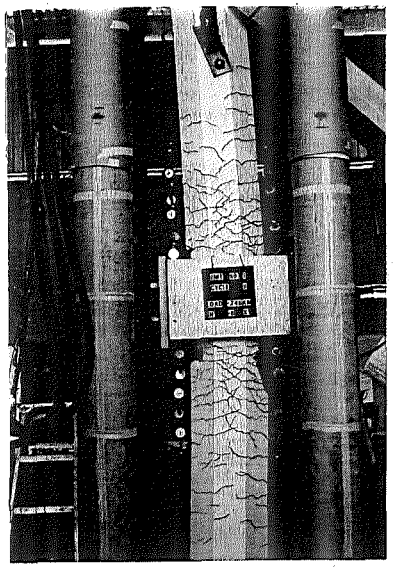

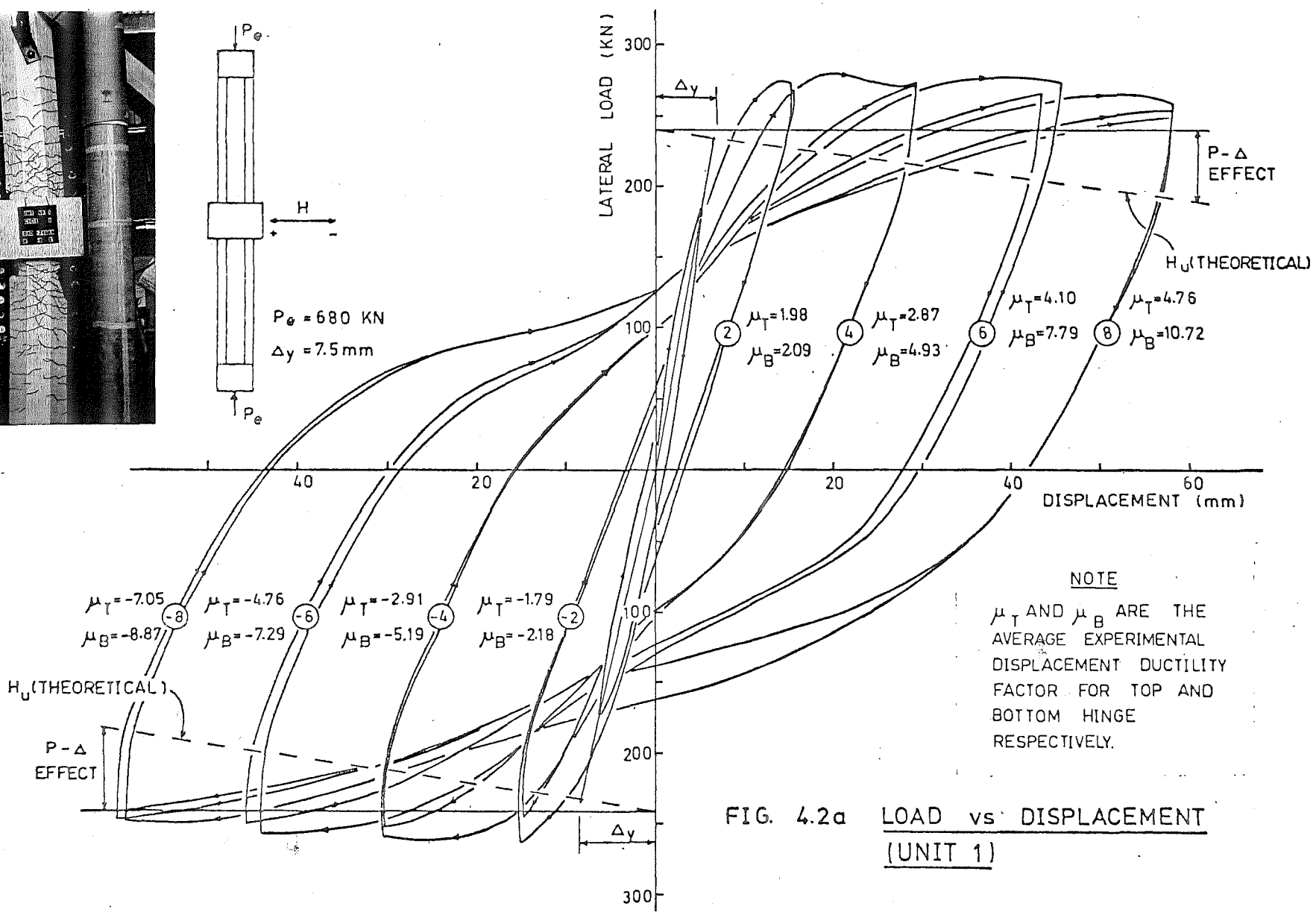

FIG. 4.2a LOAD vs DISPLACEMENT (UNIT 1)

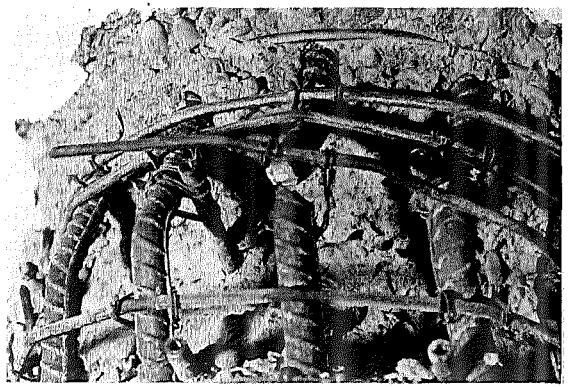

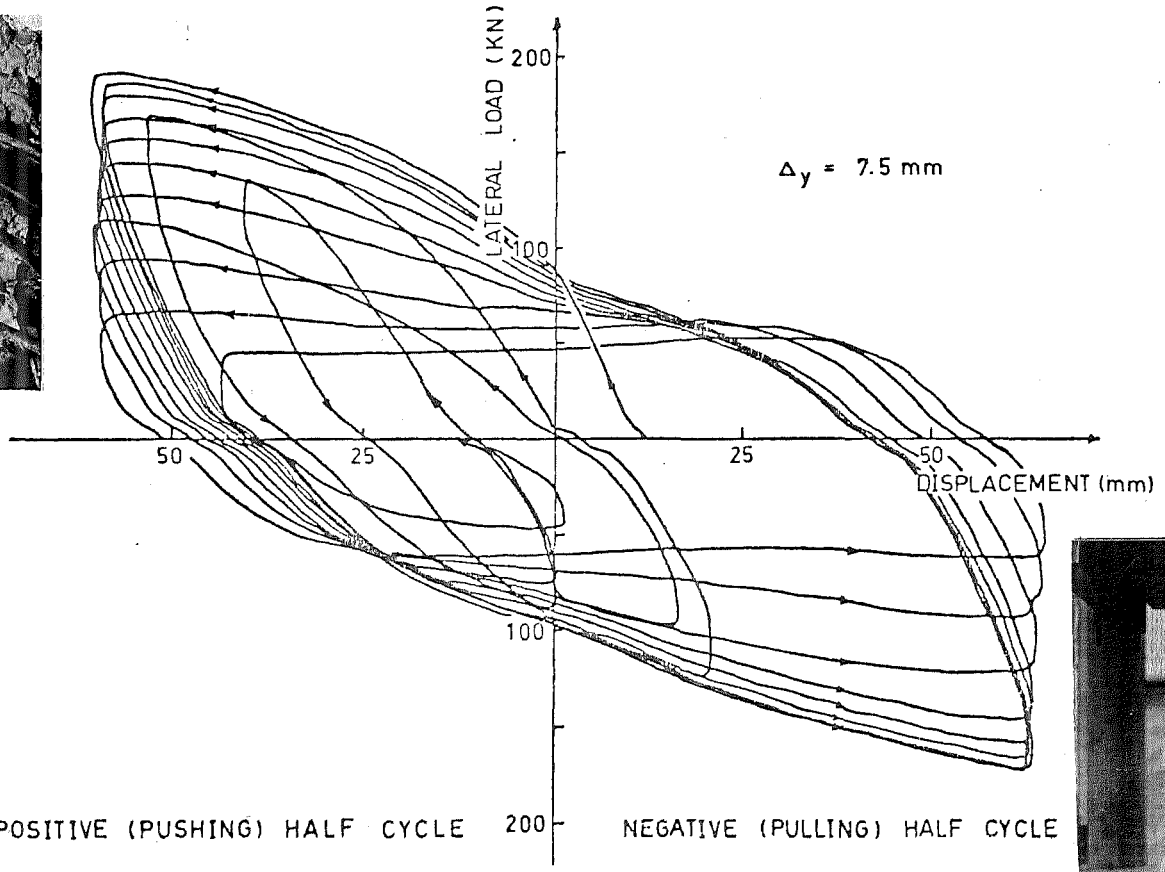

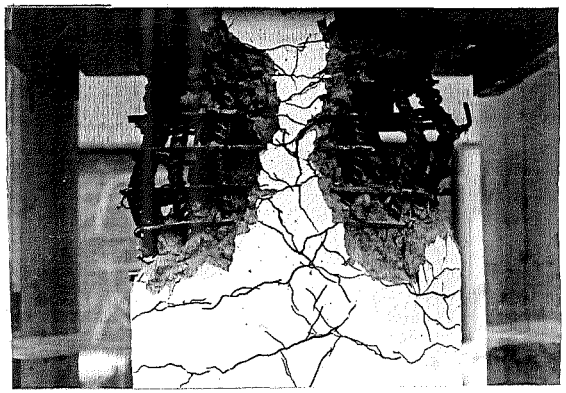

FIG. 4.2b DYNAMIC CYCLES AT μ_δ=8 (UNIT 1)

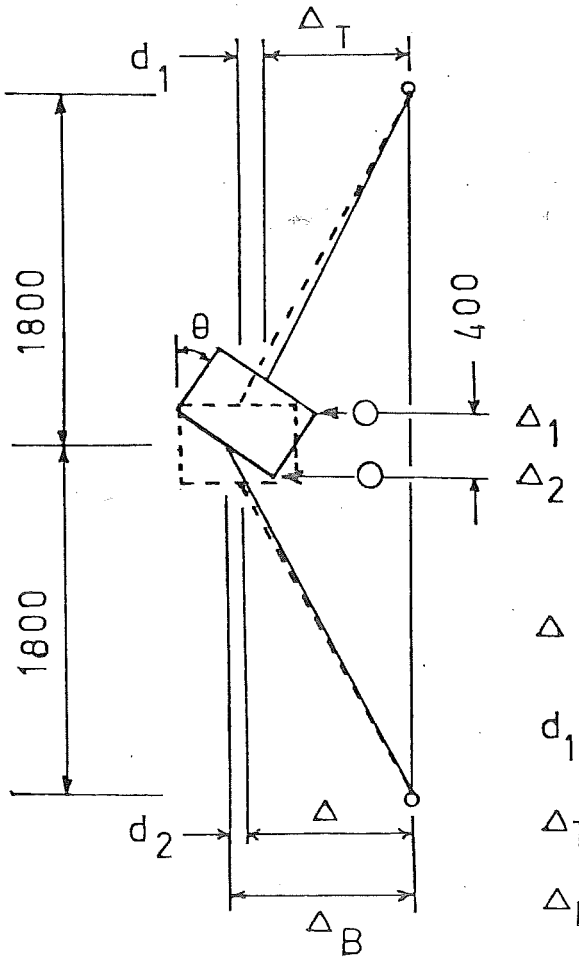

$$\Delta = \frac{\Delta_1 + \Delta_2}{2} \quad , \theta = \frac{\Delta_2 - \Delta_1}{400}$$

$$d_1 = d_2 = 1800 \times \theta$$

$$\Delta_T = \Delta - d_1$$

$$\Delta_B = \Delta + d_2$$

FIG. 4.2 c DISPLACEMENT COMPUTATION

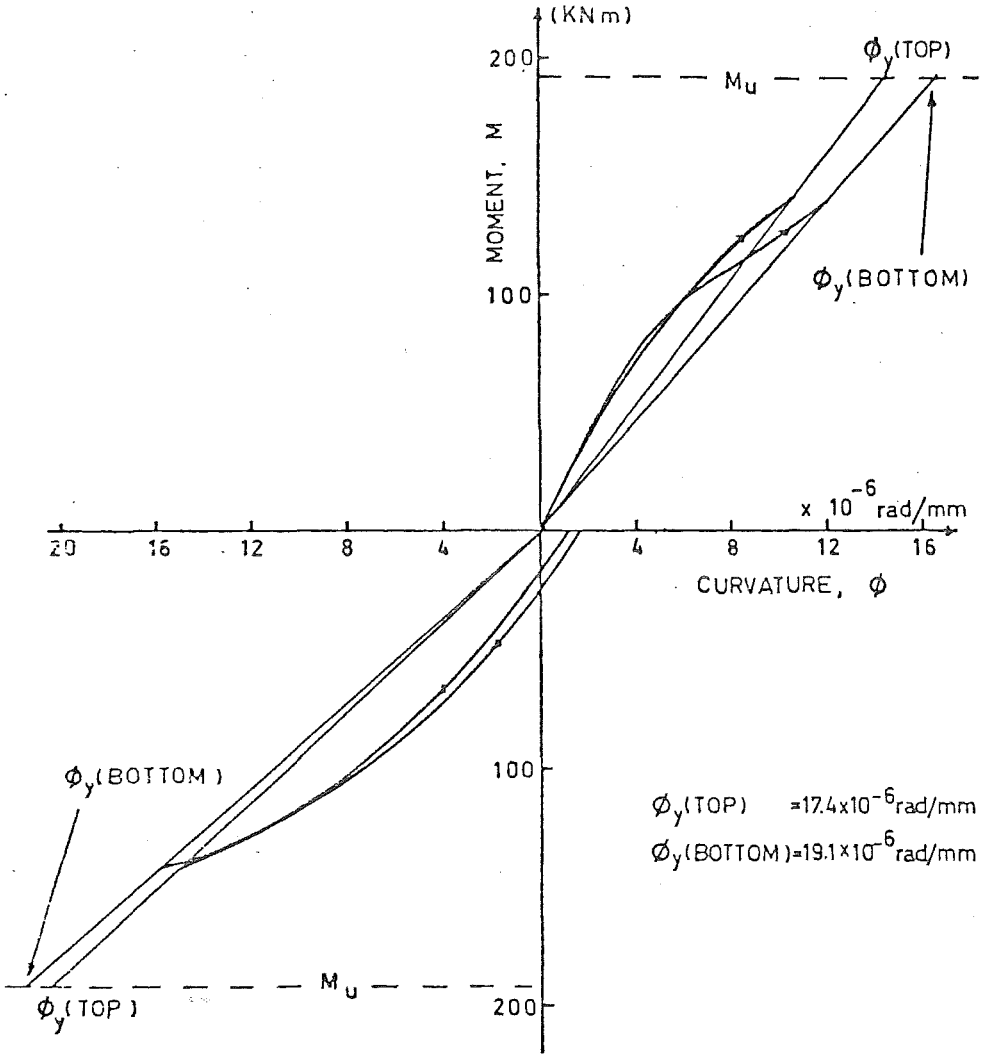

FIG. 4.3 YIELD CURVATURE (UNIT 1)

$$\therefore \phi_y = \frac{3 \times \Delta_y}{1.6 \times 1.6} , \qquad (13)$$

using the Δ_y obtained earlier. Hence, these two different ϕ_y values gave rise to two different curvature ductility values.

(c) Lateral load vs displacement curves

As mentioned in Section 2.1.1(g), using the ACI column design charts with capacity reduction factor $\phi = 1$, the theoretical ultimate moment of resistance was found to be 192 kNm. This agreed quite well with the value of 222 kNm calculated by trial and error method using ACI stress block and an extreme fibre concrete compressive strain of 0.003. The theoretical ultimate load was plotted as a dashed line which drops as the displacement increases owing to the P-Δ effect of the axial load. (Fig. 4.2a).

The load-displacement curves were plotted with total mid-height lateral load against the average midheight displacement. These curves show good energy dissipating characteristics with some stiffness degradation but no obvious strength degradation. In fact the peak loads remained practically constant, exceeding the theoretical ultimate loads. The stiffness degradation, characterised by the 'pinching' of the curves, is characteristic of columns subjected to axial compression.

During the dynamic loading cycles, strength degradation became more pronounced. The strength degraded more in the positive (i.e. pushing) half cycles than the negative (i.e. pulling) half cycles. This feature can be attributed to the structure of the loading frame; the axial load increased in positive half cycles and vice versa. Towards the last three half cycles, the specimen was so badly damaged that it did not have much stiffness. However, it still maintained a considerable load carrying capacity.

(d) Curvature profiles and curvature ductility

For each curvature dial gauge position the curvature was computed by dividing the numerical sum of compression and tensile strains by the distance between each pair of dial gauges (i.e. 500 mm). This value was then plotted at the mid point between successive pairs of dial gauges. Curvature distributions were calculated for both plastic hinge regions and plotted by joining with straight lines the points at the mid point of each curvature dial gauge length. (Fig. 4.4).

The general pattern for the curvature profiles was an increase in

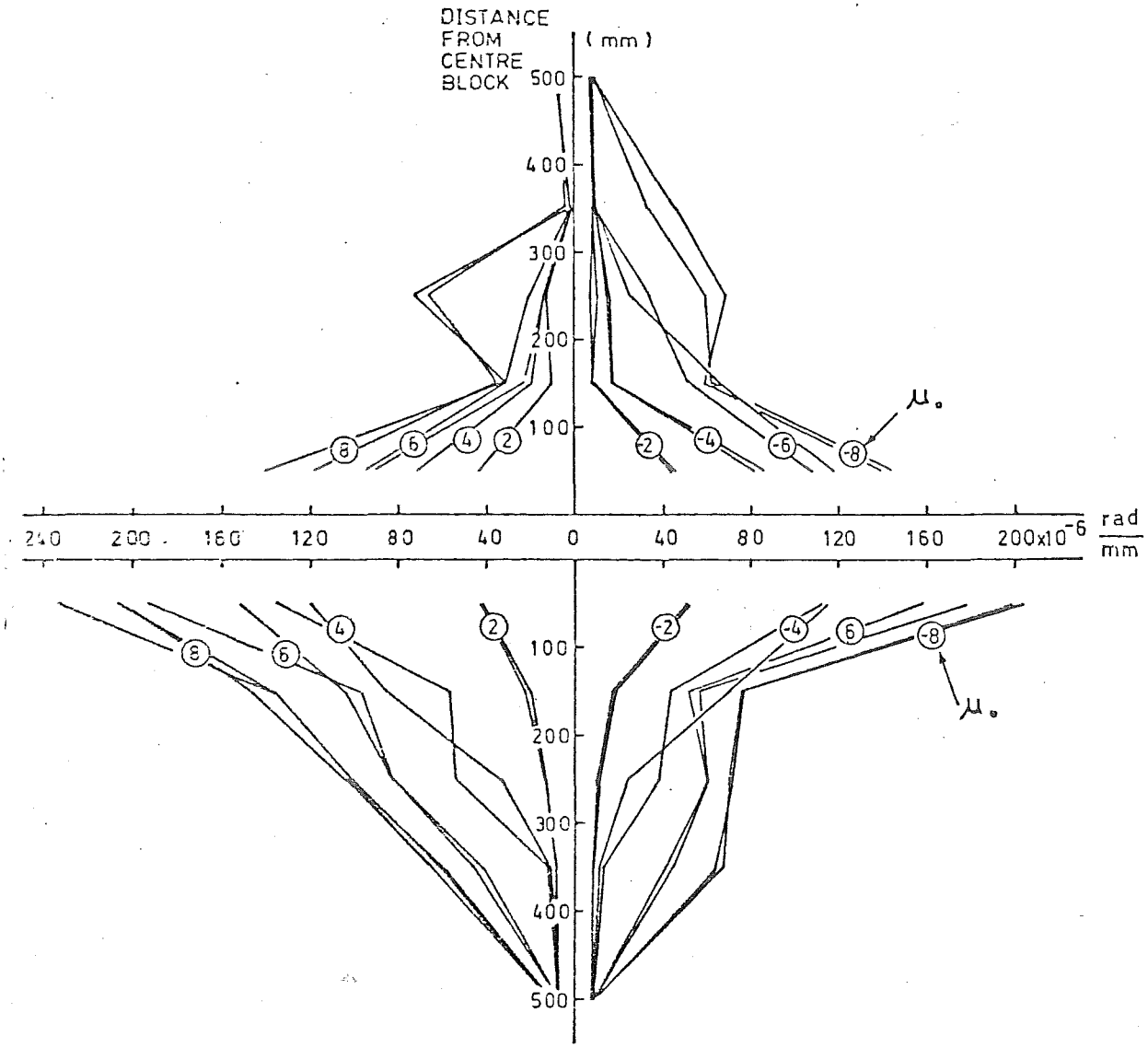

FIG. 4.4 MEASURED CURVTURE PROFILE (UNIT 1)

curvature as the displacement ductility level increased and a decrease in curvature as the distance from the centre block increased. In fact, much of the rotation was concentrated in the regions adjacent to the centre block. Also, there was generally not much variation in curvature distribution between the first and second cycles of loadings at same displacement ductility. Some local maximum value can also be noted in Fig. 4.4. This could be due to diagonal shear cracks spreading the region of tension steel yield away from the centre block.

Due to the tilting of the centre block, the bottom plastic hinge experienced more rotation than the top plastic hinge resulting in a higher curvature value at the bottom hinge than at the top hinge, especially at higher displacement ductility values.

The maximum curvature ductility, ϕ_u/ϕ_y, using the measured value for ϕ_y was found to be 12 (at the bottom plastic hinge) but if the theoretical value of ϕ_y was used, this value would be doubled, i.e. $\phi_u/\phi_y = 24$.

(e) Transverse steel strain

The strain gauge readings were taken by a 200 channel Solartron Data Transfer Unit. However, due to a large number of gauges having open circuit or being short-circuited to earth, the reliability of the remaining ones was questionable. With this uncertainty in mind, the confining steel strains and shear steel strains were plotted in Fig. 4.5 and 4.6 respectively. ("Confining steel strains" are those spiral steel strains measured perpendicular to the direction of lateral loading; "shear steel strains" are those spiral steel strains measured parallel to the direction of lateral loading).

Since most of the strain gauges were located in the top plastic hinge region, which was less severely damaged, it was not surprising to notice that the confining steel did not yield, except at $\mu_o = 8$. Furthermore, the yielding only occurred at some distance from the centre block, as a result of the confining effect of this block. (Fig. 4.2b shows the conical zone of influence of it very clearly). In the bottom plastic hinge region, the only operational strain gauge gave a much higher strain reading and showed earlier yielding (at $\mu_o = 6$) than all the others. Towards the end of the test this gauge did not show any sign that the spiral was in the strain hardening region.

In the case of shear strain, the results were quite consistent. Again, only a small number of the gauges indicated spiral yielding at $\mu_o = 8$.

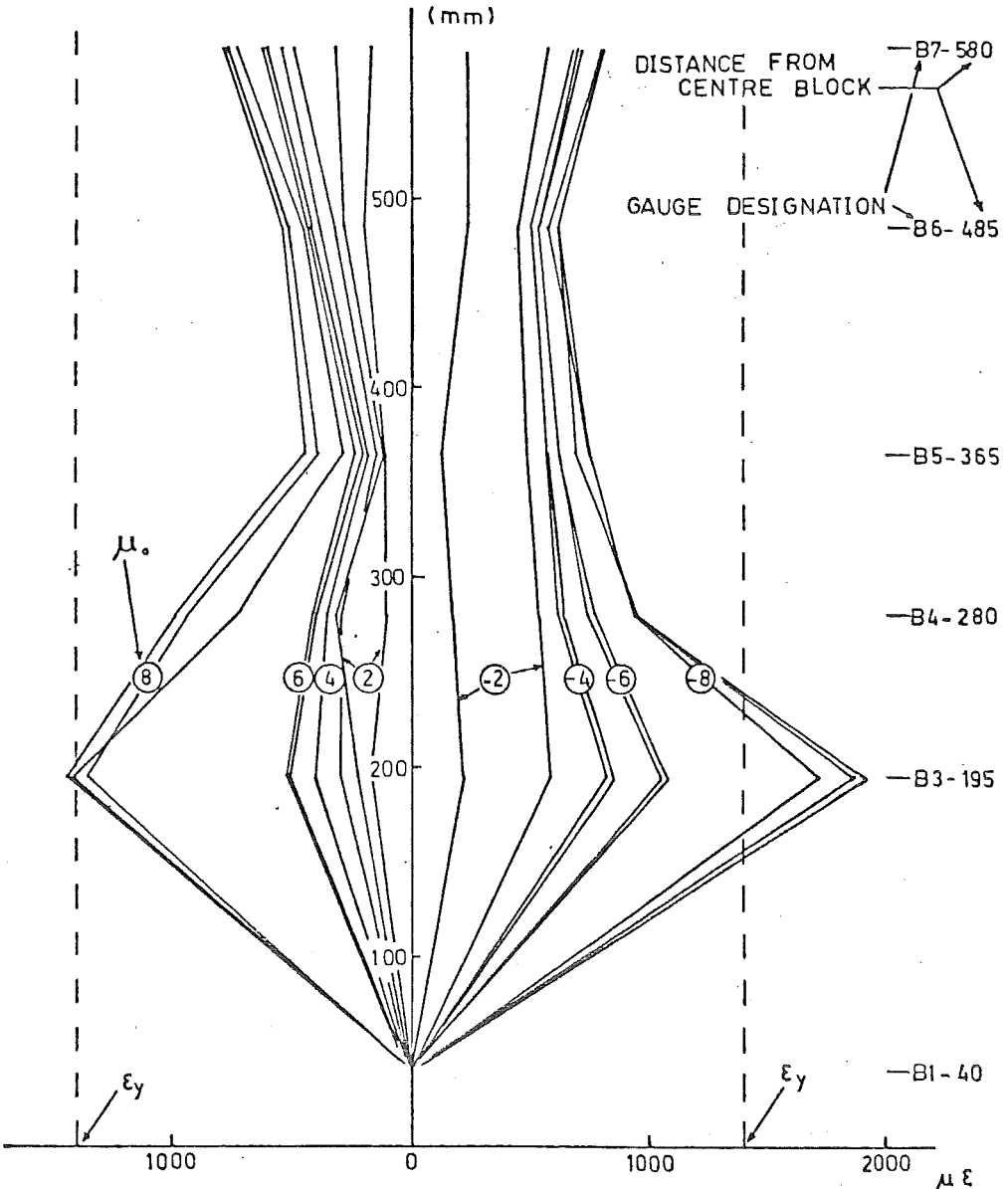

FIG. 4.5 MEASURED CONFINEMENT STRAIN DISTRIBUTION (UNIT 1)

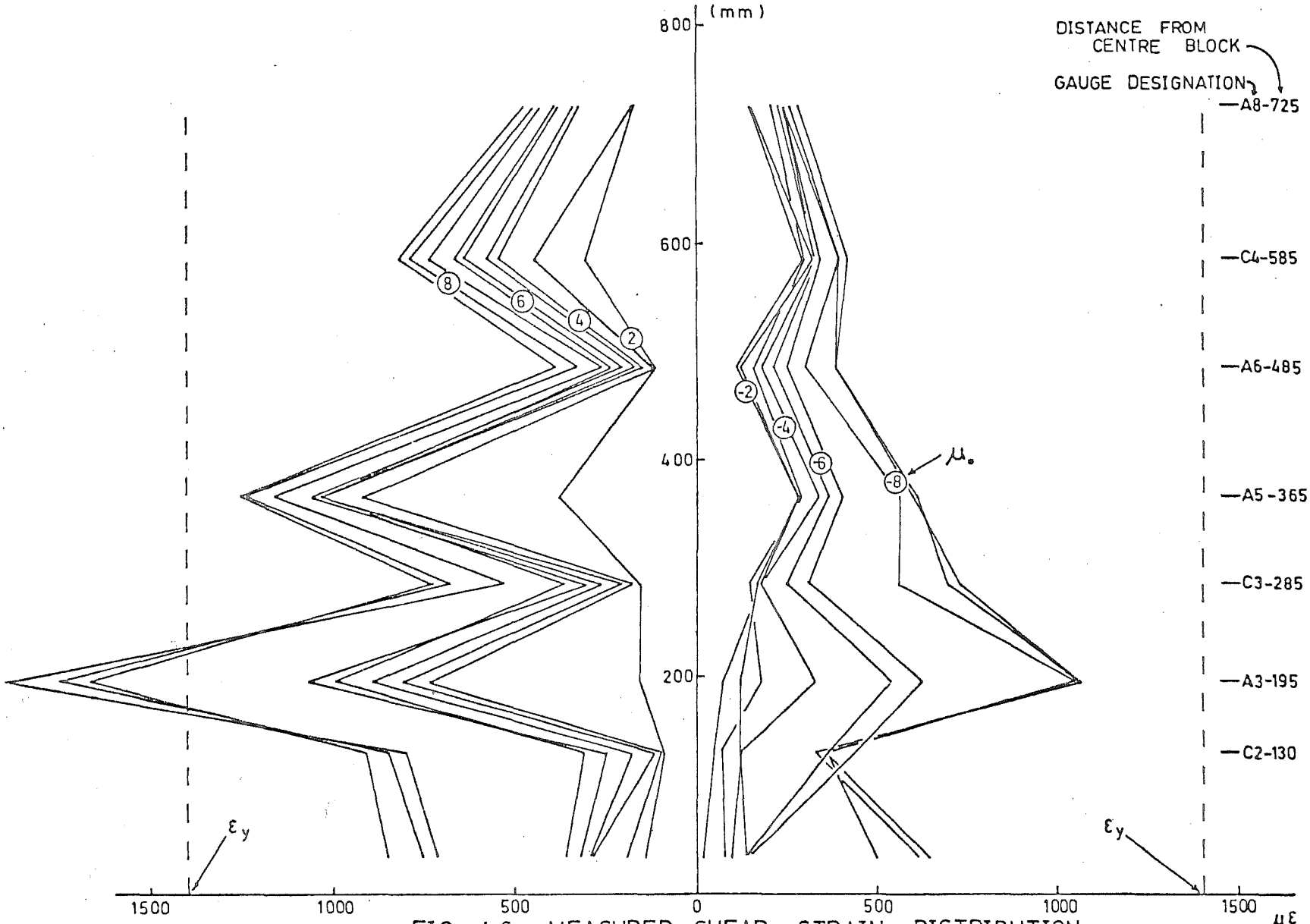

FIG. 4.6 MEASURED SHEAR STRAIN DISTRIBUTION (UNIT 1)

This plot was used to determine the maximum shear force carried by the spiral steel at every peak displacement and hence, conservatively, the shear force carried the concrete.

(f) Maximum concrete compression strain

Compression strains were calculated for the extreme compression fibre of the concrete core of the pier adjacent to the centre block for the peak displacement ductilities. Referring to Fig. 4.7, ε_B gives the compression strain for positive loadings and ε_A for negative loadings. These values were then plotted against the ductility factor for individual hinge. By inspection, a straight line was fitted through these points. Towards the higher concrete strains, this line was curved to pass through the maximum measured concrete compressive strain of 0.0405.

(g) Equivalent plastic hinge length

An equivalent plastic hinge length was calculated from the maximum curvature values, ϕ_{max}, for peak displacement ductility levels. The idealized plastic curvature was replaced by a trapezium of equal area and the same maximum curvature, Fig. 4.8. Hence the rotation in the plastic hinge is

$$\theta_p = (\phi_{max} - \phi_y) L_p \qquad (14)$$

where L_p is the length of the equivalent plastic hinge zone, and the plastic displacement, Δ_p, is the moment of the trapezium about A

$$\text{i.e. } \Delta_p = \theta_p \left(1 - \frac{L_p}{2}\right) \qquad (15)$$

$$\text{So } (\mu - 1)\,\Delta_y = (\phi_{max} - \phi_y) L_p \left(L - \frac{L_p}{2}\right) \qquad (16)$$

Rearranging Equation 16 resulted in a quadratic equation in the unknown, L_p. So with all other parameters being known, L_p can be determined. These values were then plotted against the displacement ductility factor, μ, for individual plastic hinge. (Fig. 4.9).

From the plot, it can be seen that the equivalent plastic hinge length L_p was quite independent of the displacement ductility factor, especially when $\mu < 4$ where the plasticity was not fully developed. An average value of L_p (216 mm) was taken for all the points in the region where $\mu > 4$ and the upper and lower bounds for the values were included as well (Fig. 4.9).

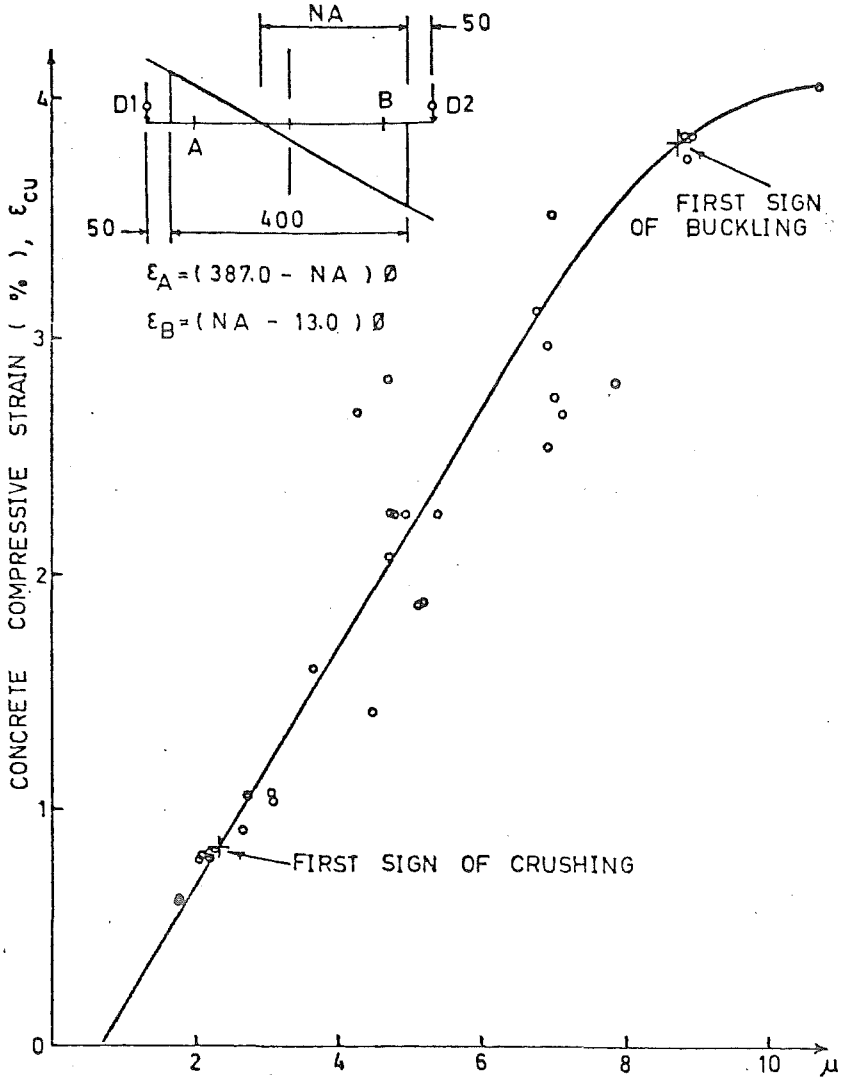

FIG. 4.7 ε_{cu} vs μ (UNIT 1)

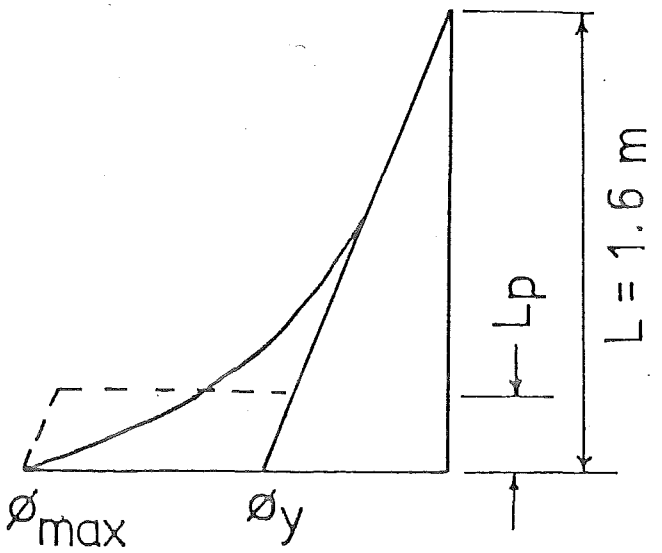

FIG. 4.8 EQUIVALENT PLASTIC HINGE LENGTH

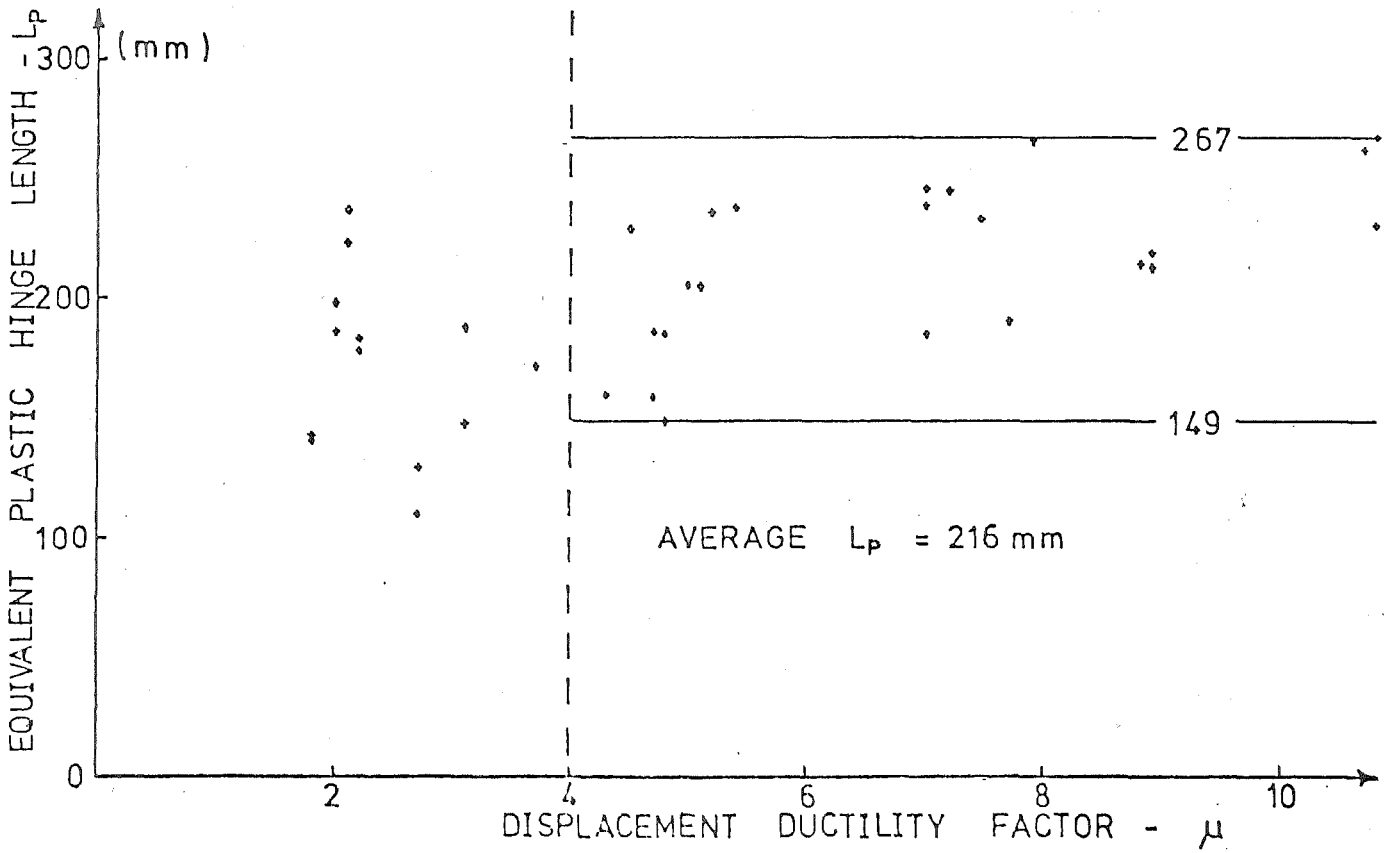

FIG. 4.9 L_p vs μ (UNIT 1)

(h) Idealized stress-strain curve

The analytical confinement models for spirally confined sections proposed by Park and Leslie (9) has four regions, Fig. 4.10 a .

Region AB: $0 \leq \varepsilon_c \leq 0.002$. A second degree parabola is assumed, following the curve for unconfined concrete.

$$f_c = f'_c \left[\frac{2\varepsilon_c}{0.002} - \left(\frac{\varepsilon_c}{0.002} \right)^2 \right] \qquad (17)$$

Region BC: $0.002 \leq \varepsilon_c \leq \varepsilon_{cc}$. The region of increasing strength due to confinement is represented by a further second degree parabola.

$$f_c = f'_c \; (f'_{cc} - f'_c) \left[\frac{2(\varepsilon_c - 0.002)}{\varepsilon_{cc} - 0.002} - \left[\frac{\varepsilon_c - 0.002}{\varepsilon_{cc} - 0.002} \right]^2 \right] \qquad (18)$$

where

$$f'_{cc} = f'_c \left[1 + 2.3 \; (\rho_s - \bar{\rho}_s) \frac{f_{yh}}{f'_c} \right] \qquad (19)$$

$$\varepsilon_{cc} = 0.002 \left[1 + 23 \; (\rho_s - \bar{\rho}_s) \frac{f_{yh}}{f'_c} \right] \qquad (20)$$

ρ_s is the ratio of volume of spiral steel to volume of concrete core, and $\bar{\rho}_s$ is the value of ρ_s when the spiral pitch equals the spiral diameter. Also, if $\rho_s \leq \bar{\rho}_s$ then $(\rho_s - \bar{\rho}_s) = 0$.

Region CD: $\varepsilon_{cc} \leq \varepsilon_c \leq \varepsilon_{20c}$. A linear falling branch is assumed.

$$f_c = f'_{cc} \left[1 - z \; (\varepsilon_c - \varepsilon_{cc}) \right] \qquad (21)$$

where

$$z = \frac{107}{f'_{cc}} \left[\frac{f'_c}{\rho_s \; f_{yh}} \right]^{1.13} \qquad (22)$$

was found from a statistical analysis of the test data of Iyengar, et al, (23) for spiral bars with $f_y = 319$ MPa.

Region DE: $\varepsilon_c > \varepsilon_{20c}$. It is assumed that concrete can sustain a compressive stress of $0.2 \; f'_c$ indefinitely.

For specimen one, $f'_{cc} = 30.8$ MPa,

$\varepsilon_{cc} = 0.00568$

and $z = 53.08$.

From these parameters the idealized stress-strain curve was plotted in Fig. 4.11. Using this stress-strain curve, the ultimate moments

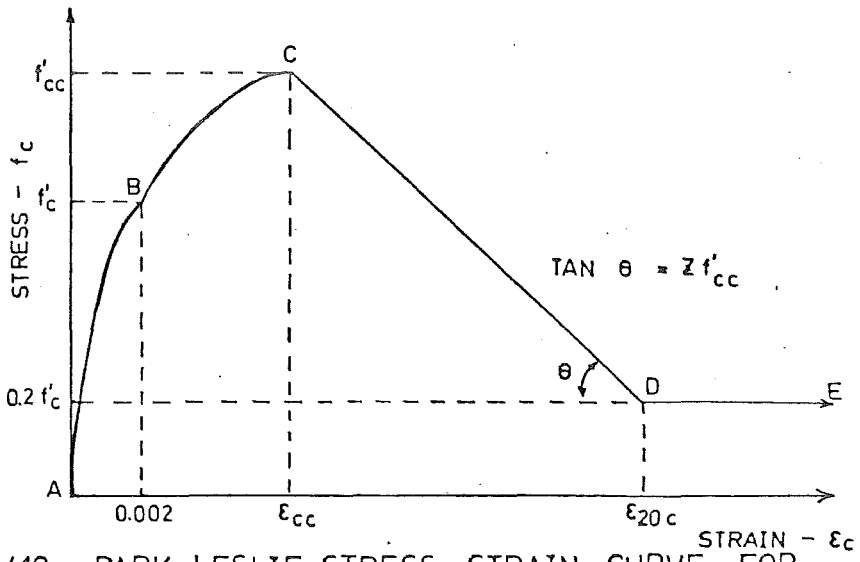

FIG. 4.10 a PARK-LESLIE STRESS-STRAIN CURVE FOR CONFINED CONCRETE

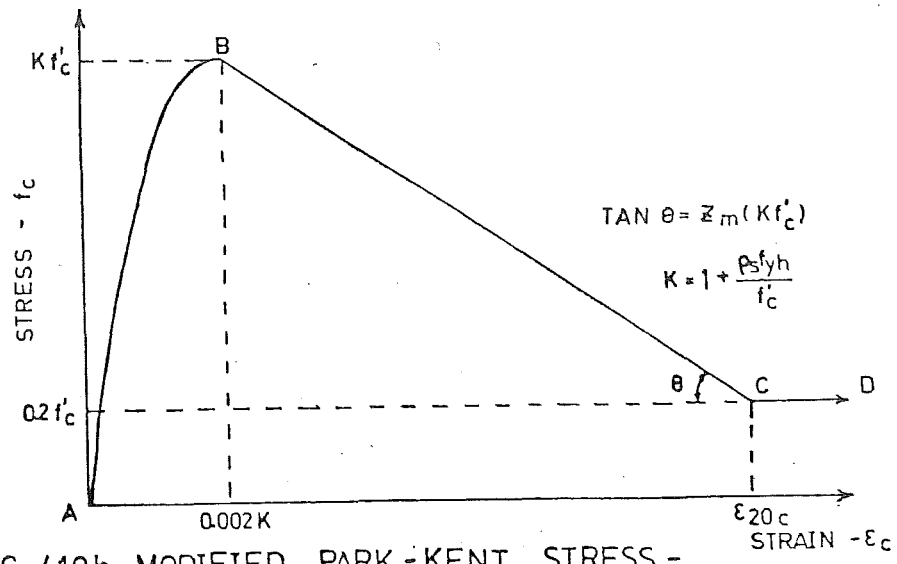

FIG. 4.10 b MODIFIED PARK-KENT STRESS-STRAIN CURVE FOR CONFINED CONCRETE

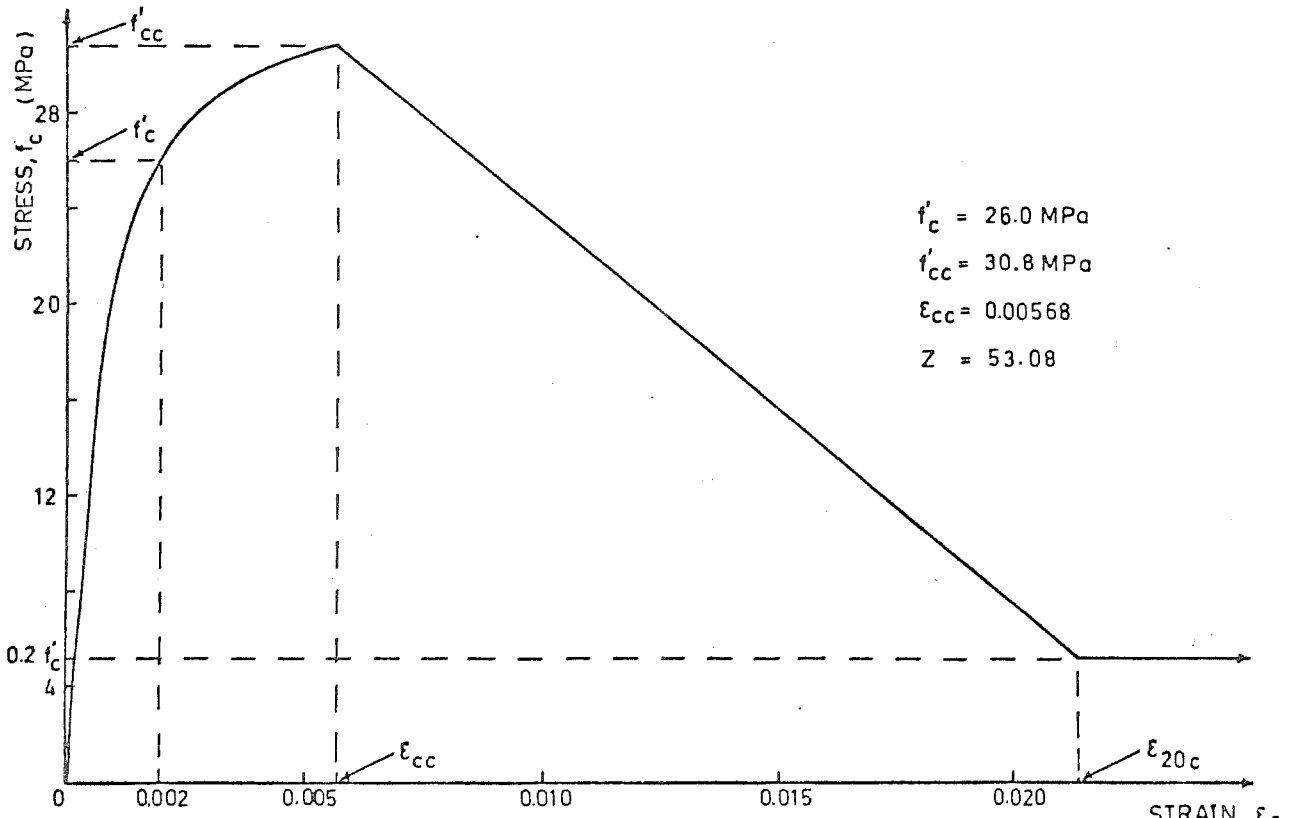

FIG. 4.11 ANALYTICAL STRESS-STRAIN CURVE FOR CIRCULAR CONFINED CONCRETE (UNIT 1)

corresponding to extreme confined concrete compression strain of maximum experimental ε_{cu} and 0.02 were calculated using the iterative procedure summarised in the flow chart in Fig. 4.12. The values were 163 kNm and 194 kNm for maximum ε_{cu} and $\varepsilon_{cu} = 0.02$, respectively.

To serve as a comparison with the f'_{cc} value obtained above, a f''_{cc} value was computed assuming that stress f''_{cc} acts uniformly over the compression zone, based on core dimensions only, and with maximum ε_{cu} at the extreme core fibre. A trial and error process using the complete steel stress-strain curve and strain compatibility was used to give an exact balance of measured and predicted ultimate loads. The value found for f''_{cc} was 44.9 MPa compares with the f'_{cc} of 30.8 MPa found from Equation 19.

4.2.2 Specimen Two

(a) General description

In the elastic cycle, the lateral loading sequence was 60 kN, 120 kN and 160 kN. All the subsequent cycles had 60 kN increments to $\mu_o = 1$ followed by displacement controlled loadings.

Cracks appeared in the top and bottom plastic hinges during the negative elastic half cycle at -160 kN. At $\mu_o = 2$, the cracking zone extended to about 500 mm from the centre block. On further loading to $\mu_o = 4$, the cracks showed inclination but no sign of the cracking zone being extended further away from the centre block. The less extensive pattern of cracking compared with Unit 1 was due to the higher axial load.

Minor crushing started at $\mu_o = 1.5$ (289 kN) and became extensive on loading to $\mu_o = 2$, extending 200 mm from the centre block in both plastic hinge regions. The crushing zones concentrated one side only in each plastic hinge region and those sides were opposite in the two hinges. On further loading crushing zone extended sideways to the centroidal axis and lengthwise to about 800 mm from the centre block. The crushed concrete started to spall at $\mu_o = 4$ and higher and this occurred right back to the longitudinal steel.

The concentration of crushing on two different sides of the plastic hinge regions resulted in one hinge rotating more than the other in one direction and vice versa in the opposite direction. This behaviour became more and more obvious at higher displacement ductilities, so much so that the unit formed an 'S' shape at failure.

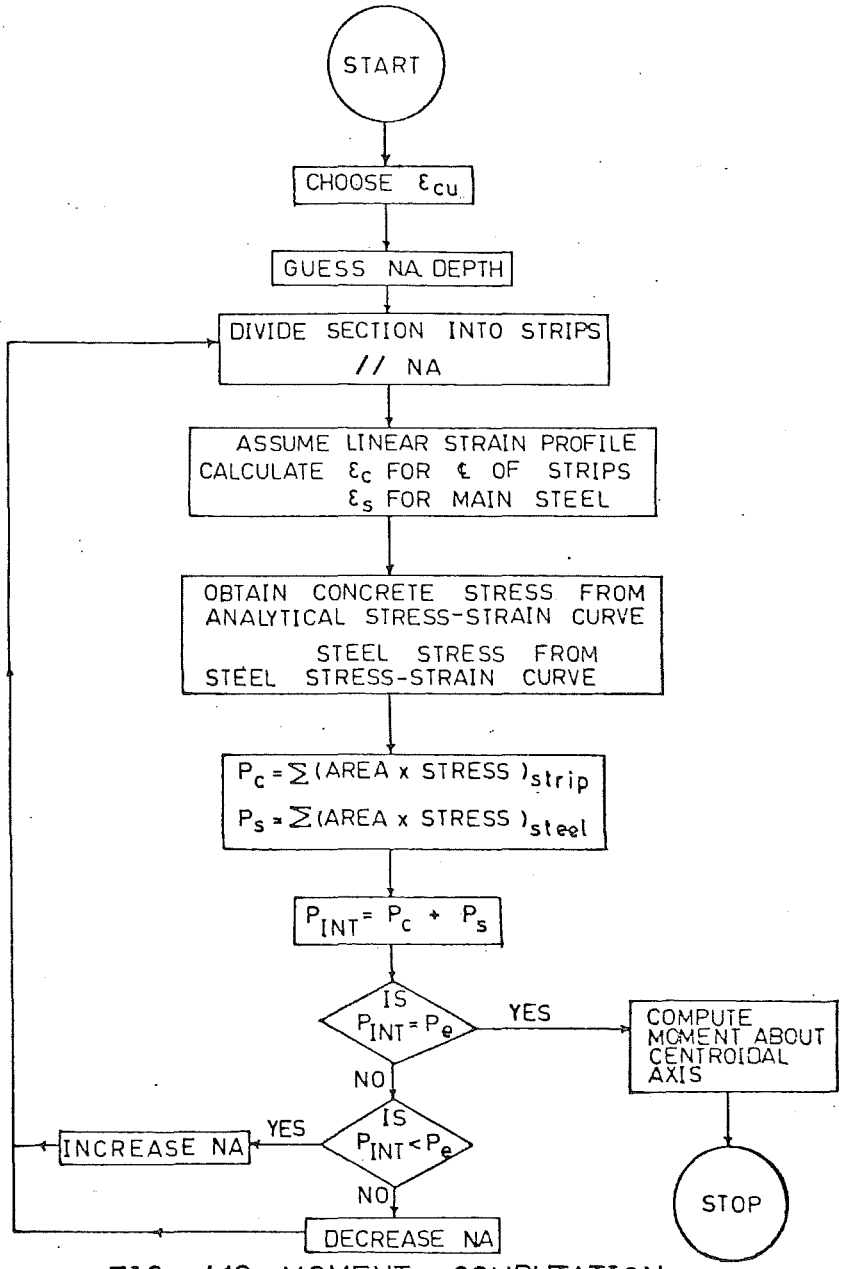

FIG. 4.12 MOMENT COMPUTATION

At $\mu_o = 8$, the spiral commenced to straighten indicating the onset of longitudinal bar buckling. At this stage, under such a high axial load, the specimen was found to have shortened by 20 mm. After the second cycle of $\mu_o = 8$, the specimen was so badly damaged that it was decided to forego the dynamic testing but instead to complete the test by deflecting the unit continuously in the negative direction without taking any further readings. (Fig. 4.13 and 4.14). The specimen eventually failed by fracture of spiral in the top plastic hinge.

(b) Yield displacement and yield curvature derivation

The derivation for yield displacement and yield curvature was the same as described in Section 4.2.1(b). The measured Δ_y was found to be 6.5 mm as compared to the theoretically determined value of 5.6 mm. Fig. 4.15 gives the moment vs curvature curves in the elastic cycle and the measured ϕ_y values for the two hinges. The value of ϕ_y obtained using Equation 13 was 7.6×10^{-6} rad/mm, which was about 60% of the experimental value.

(c) Lateral load vs displacement curves

A similar procedure as for Unit 1 was used to find the ACI theoretical ultimate load (200 kNm). The trial and error method gave the value of 219 kNm, indicating quite a good agreement. Due to the high axial load the $P-\Delta$ effect was very pronounced as can be seen in Fig. 4.13. Though the load carrying capacity of the specimen kept on diminishing, it still remained above the predicted theoretical ultimate load even at $\mu_o = 8$. There was not much stiffness degradation and thus the energy dissipating characteristics were good. It is also interesting to note that in the last cycle of loading, the curve was nearly a circular loop, Fig. 4.14.

(d) Curvature profiles and curvature ductility

Due to the peculiar behaviour, the rotation was concentrated at one plastic hinge for loading in one direction and at the other for loading in the other direction. As can be seen in Fig. 4.16, on the positive (pushing) direction, the rotation was concentrated in the bottom plastic hinge (therefore the crushing on the face nearer to the jack was more severe for this hinge) and vice versa in the top hinge. As a whole, the bottom plastic hinge also had a higher curvature value giving a maximum $\frac{\phi_u}{\phi_y}$ value of 30, using the measured ϕ_y value. If the theoretical value of ϕ_y was used, the value became 50.

(e) Transverse steel strain

For this specimen the majority of the strain gauges were located at

Pe = 2111 KN

Δy = 6.5mm

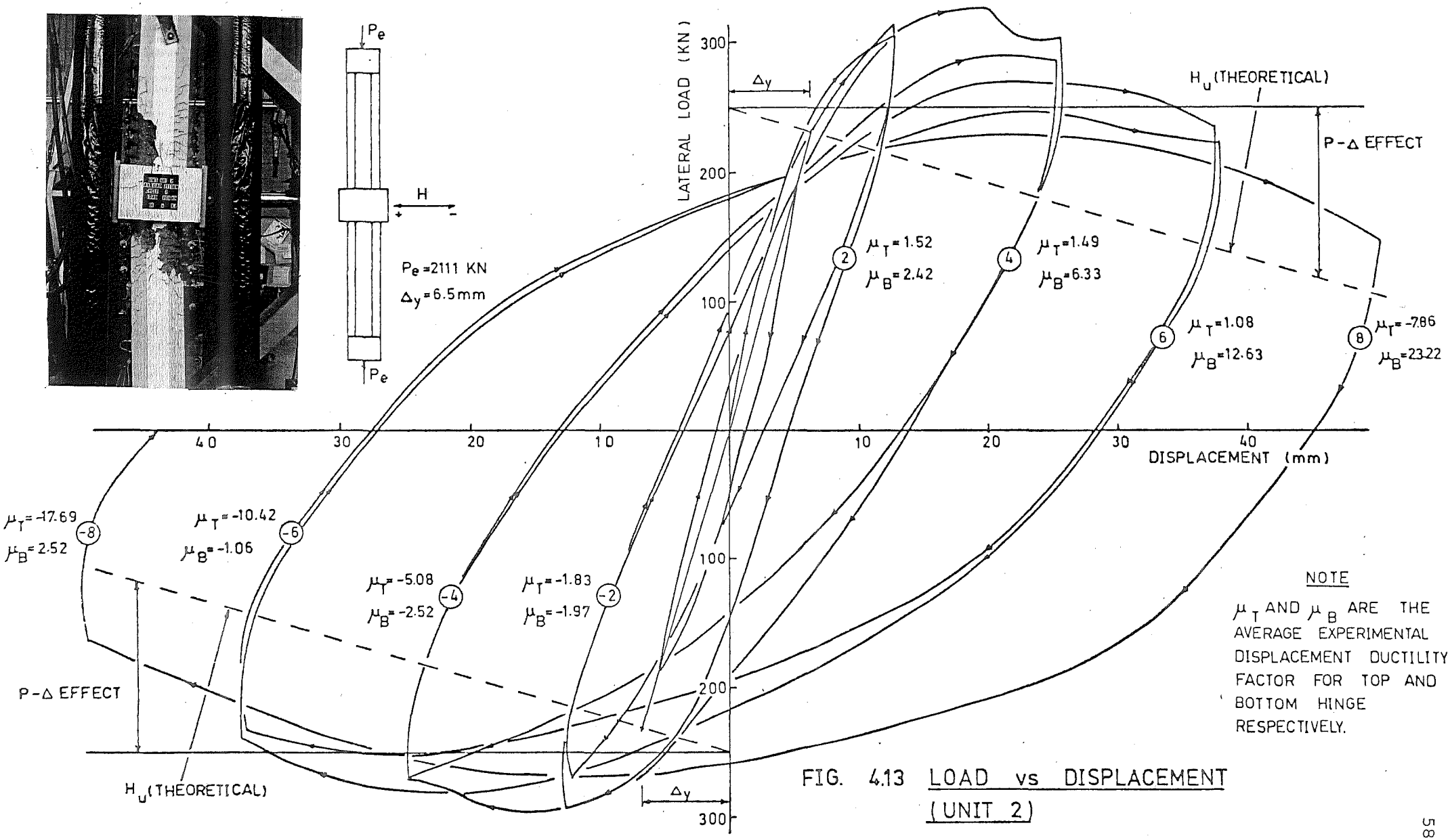

NOTE

μ_T AND μ_B ARE THE AVERAGE EXPERIMENTAL DISPLACEMENT DUCTILITY FACTOR FOR TOP AND BOTTOM HINGE RESPECTIVELY.

FIG. 4.13 LOAD vs DISPLACEMENT (UNIT 2)

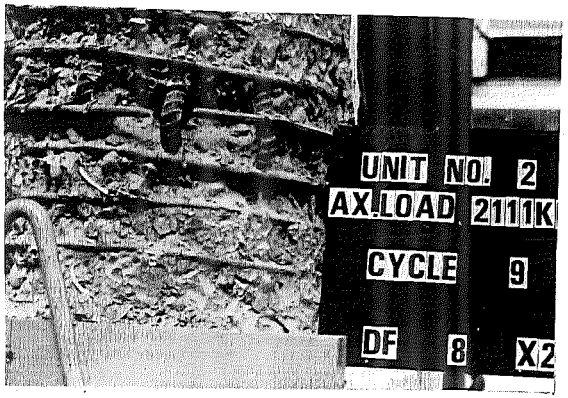

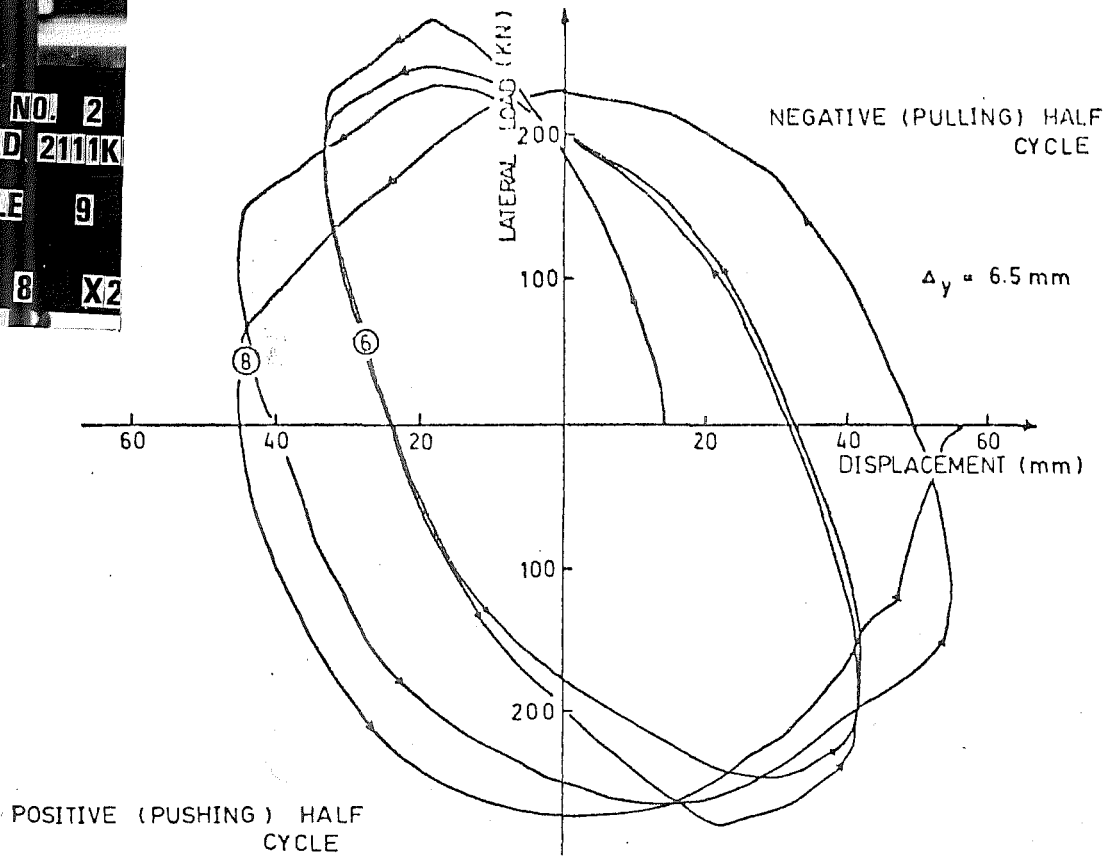

FIG. 4.14 HYSTERESIS LOOPS AT $\mu_\circ = 6$ & $\mu_\circ = 8$

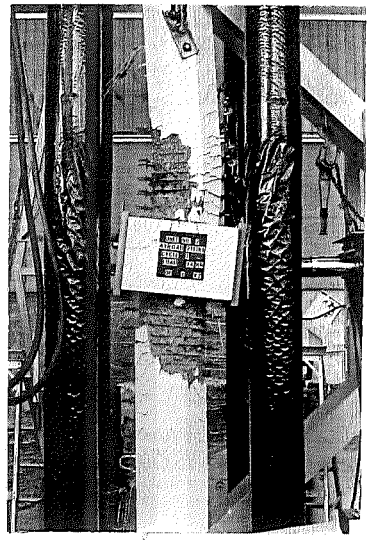

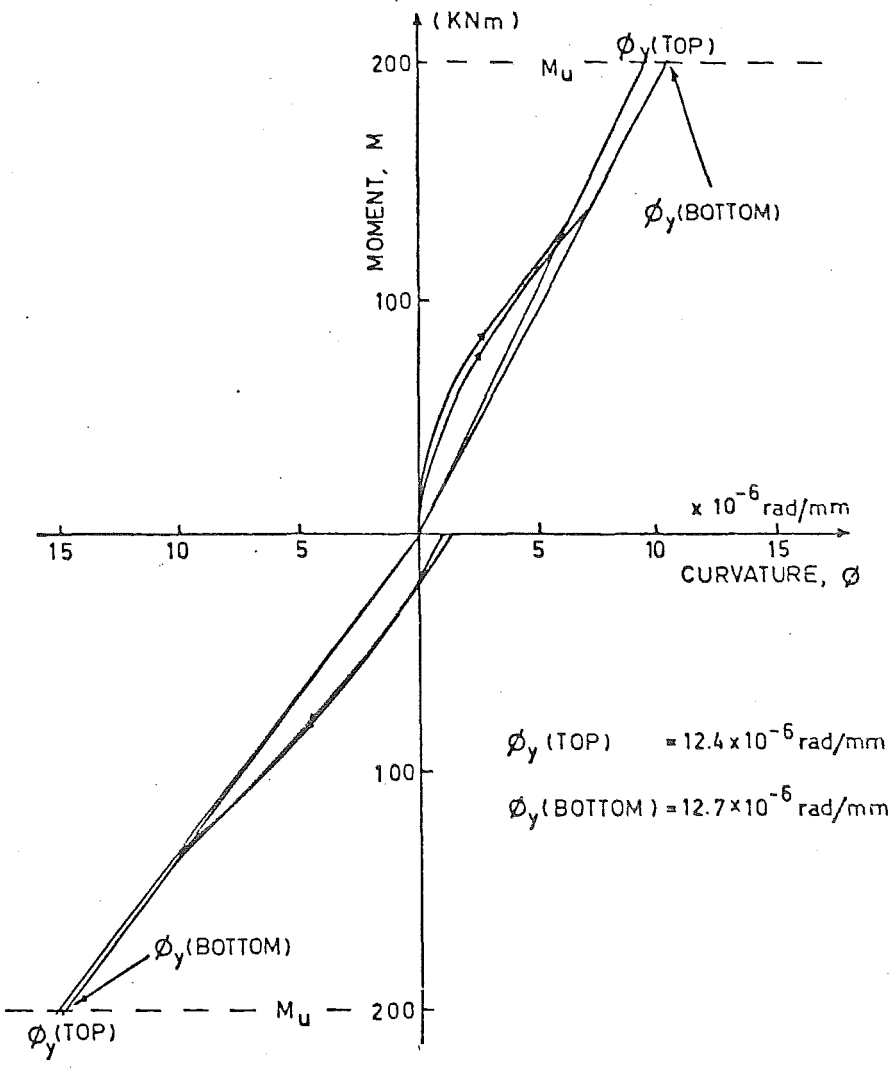

FIG. 4.15 YIELD CURVATURE (UNIT 2)

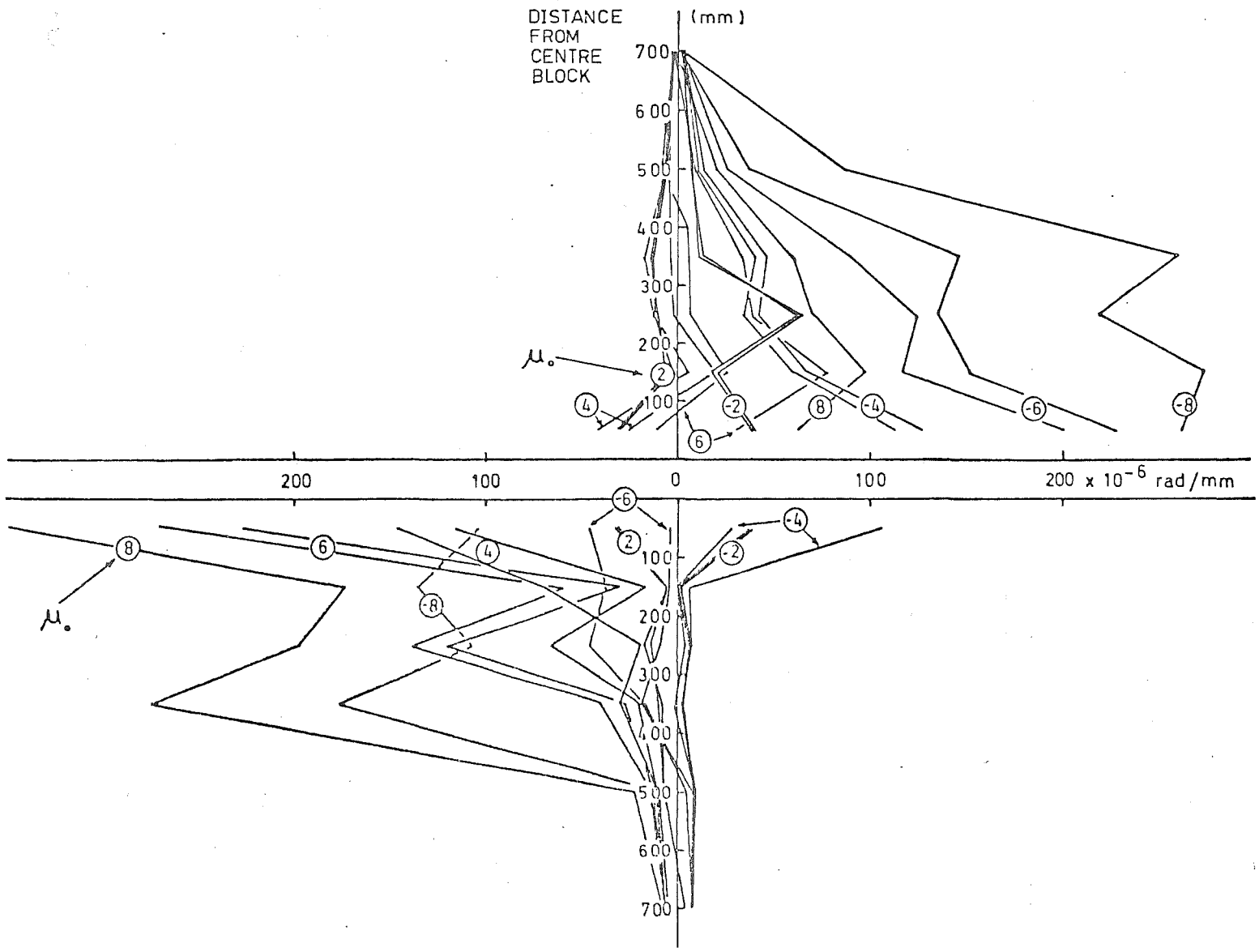

FIG. 4.16 MEASURED CURVATURE PROFILE (UNIT 2)

the bottom plastic hinge and their readings were taken manually by 50 - Channel Budd Bridge.

Starting from $\mu_o = 4$, there was considerable yielding of confining steel. However, since the strain gauges were situated opposite the severe crushing zone the strains measured were not as high as those check gauges in the top hinge in which the gauges were situated in the severe crushing zone. Some of the gauges measured as high as 20000 με (i.e. in the strain hardening region) in that hinge at $\mu_o = 6$ and higher (Fig. 4.17).

The shear strains measured on the spirals were significantly higher than the confining strains. Almost all the spirals in the plastic hinge region yielded and some spirals (in the region 300-400 mm away from the centre block) experienced strain hardening at $\mu_o = 8$ (Fig. 4.18).

Again, the plot was used to find the maximum shear force carried by the spirals, and from the difference between this and the applied shear, the shear force carried by the concrete was obtained.

(f) Maximum concrete compression strain

In the similar manner the compression strains were calculated for the extreme compression fibre of the concrete core. These strains were then plotted against displacement ductility factor. A straight line which later curved to pass through the maximum ε_{cu} (0.1271) was fitted by inspection. (Fig. 4.19).

(g) Equivalent plastic hinge length

The average value of the equivalent plastic hinge lengths at $\mu > 4$ was 242 mm. However, this value might not be representative as the points plotted were much more scattered than that for Unit 1, as can be seen in Fig. 4.20. The points were closer to the lower bound than the upper one.

(h) Idealized stress-strain curve

Following Park and Leslie's proposal, for this specimen,

$$f'_{cc} = 36.9 \text{ MPa}$$
$$\varepsilon_{cc} = 0.00788$$
$$z = 24.73$$

and using this idealized stress-strain curve (Fig. 4.21), the ultimate moment at $\varepsilon_{cu} = 0.02$ was 223 kNm. However, due to the peculiar behaviour of the specimen, i.e. the absence of a definite yield plateau, especially at high displacement ductility, the value of ultimate moment at maximum experimental ε_{cu} was incredibly small. Similarly, the

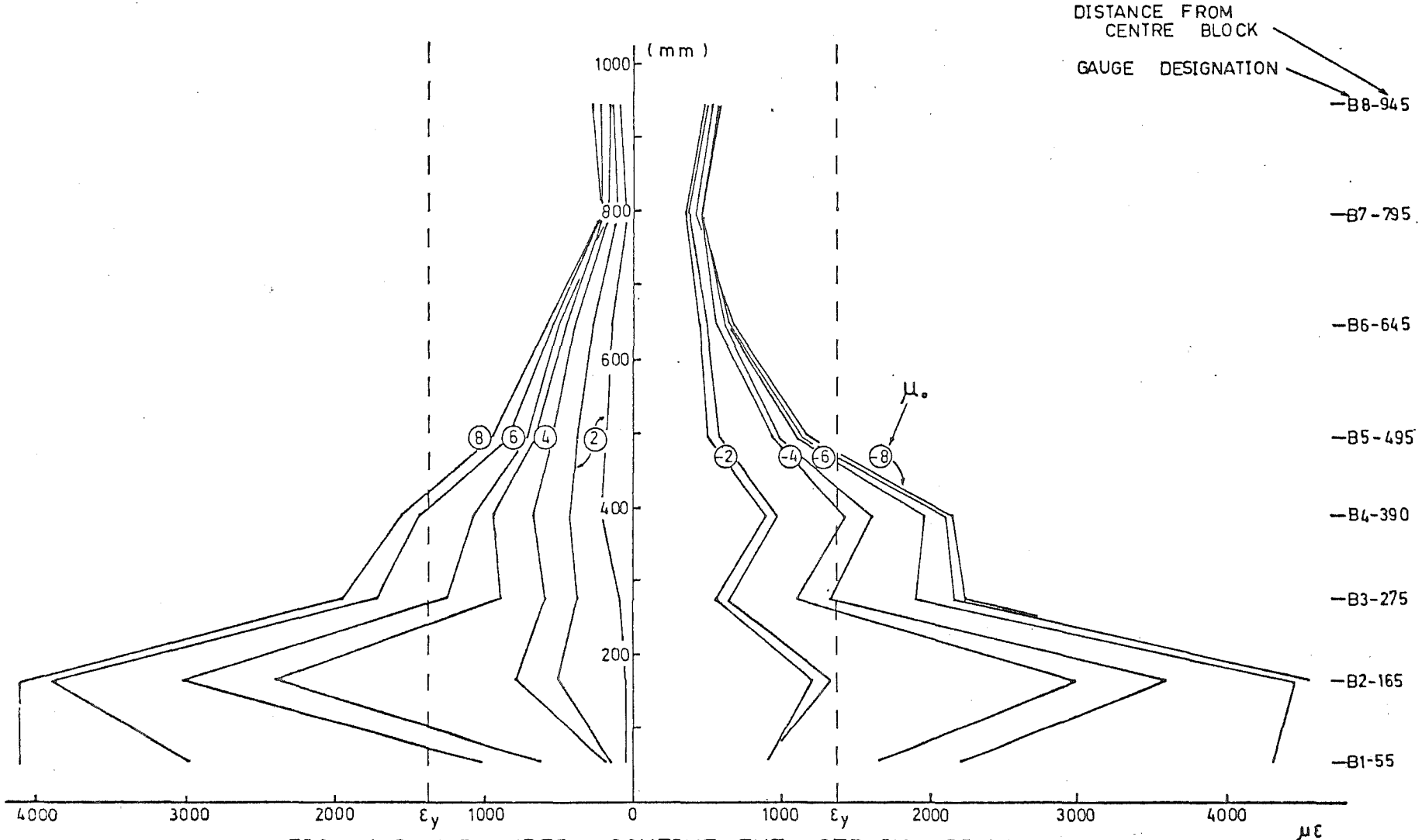

FIG. 4.17 MEASURED CONFINEMENT STRAIN DISTRIBUTION (UNIT 2)

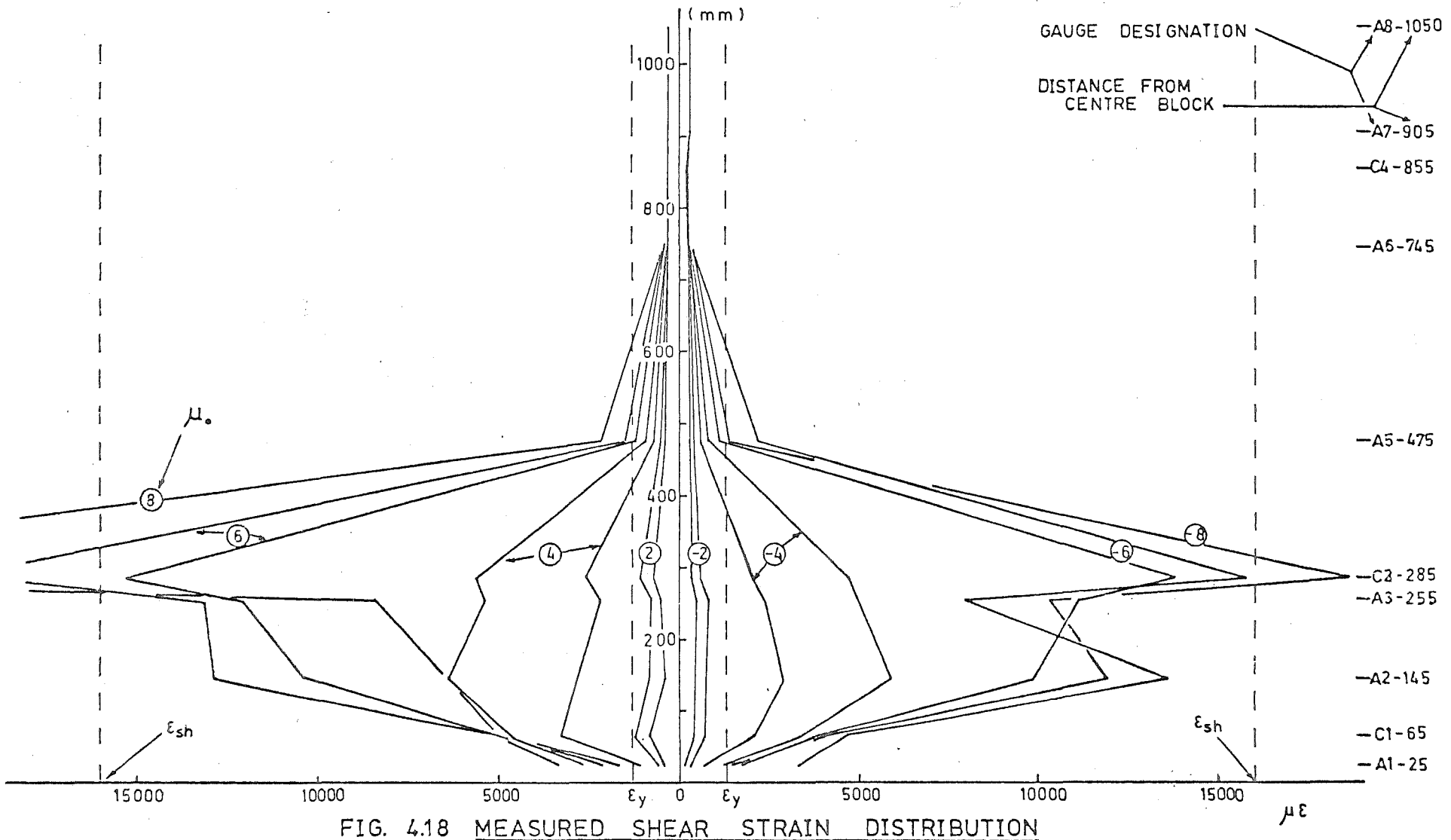

FIG. 4.18 MEASURED SHEAR STRAIN DISTRIBUTION (UNIT 2)

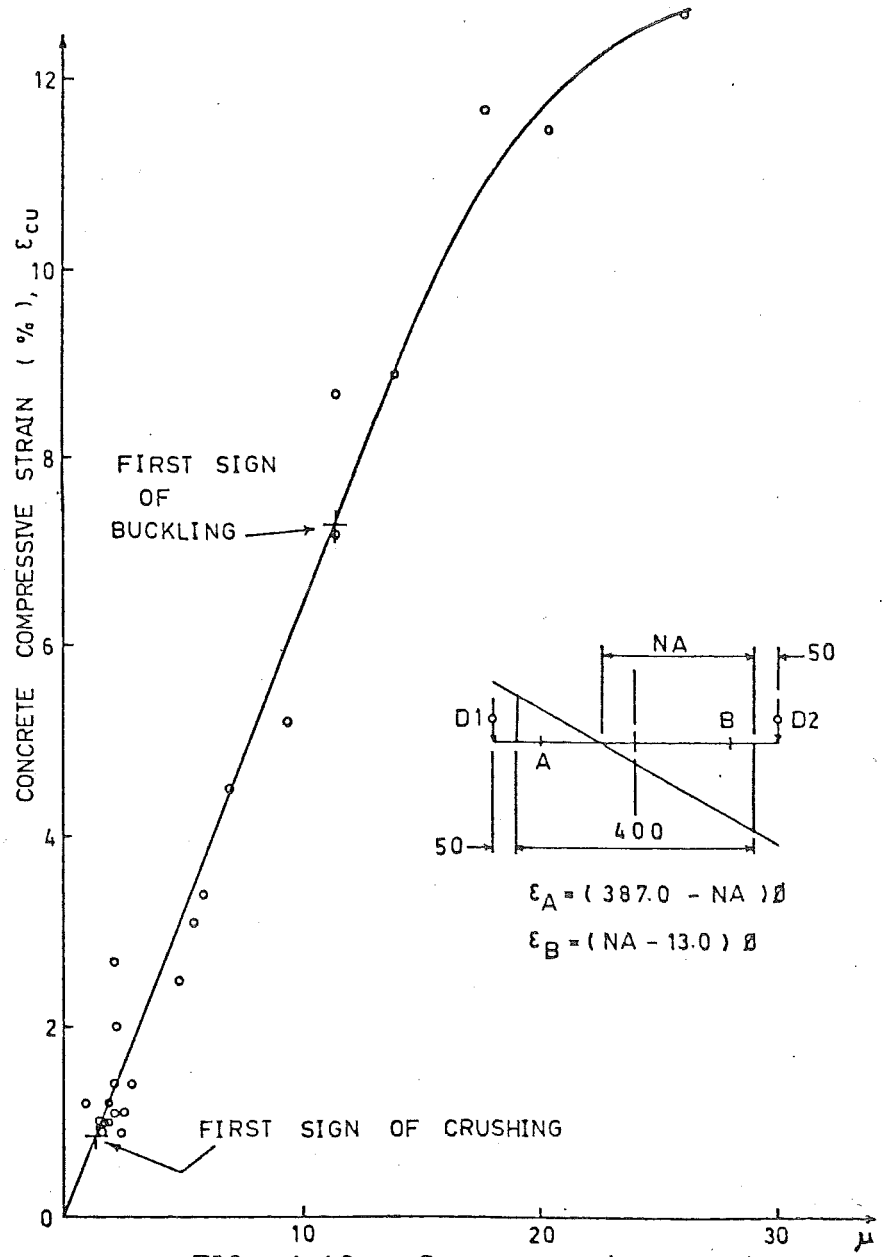

FIG. 4.19 ε_{cu} vs μ (UNIT 2)

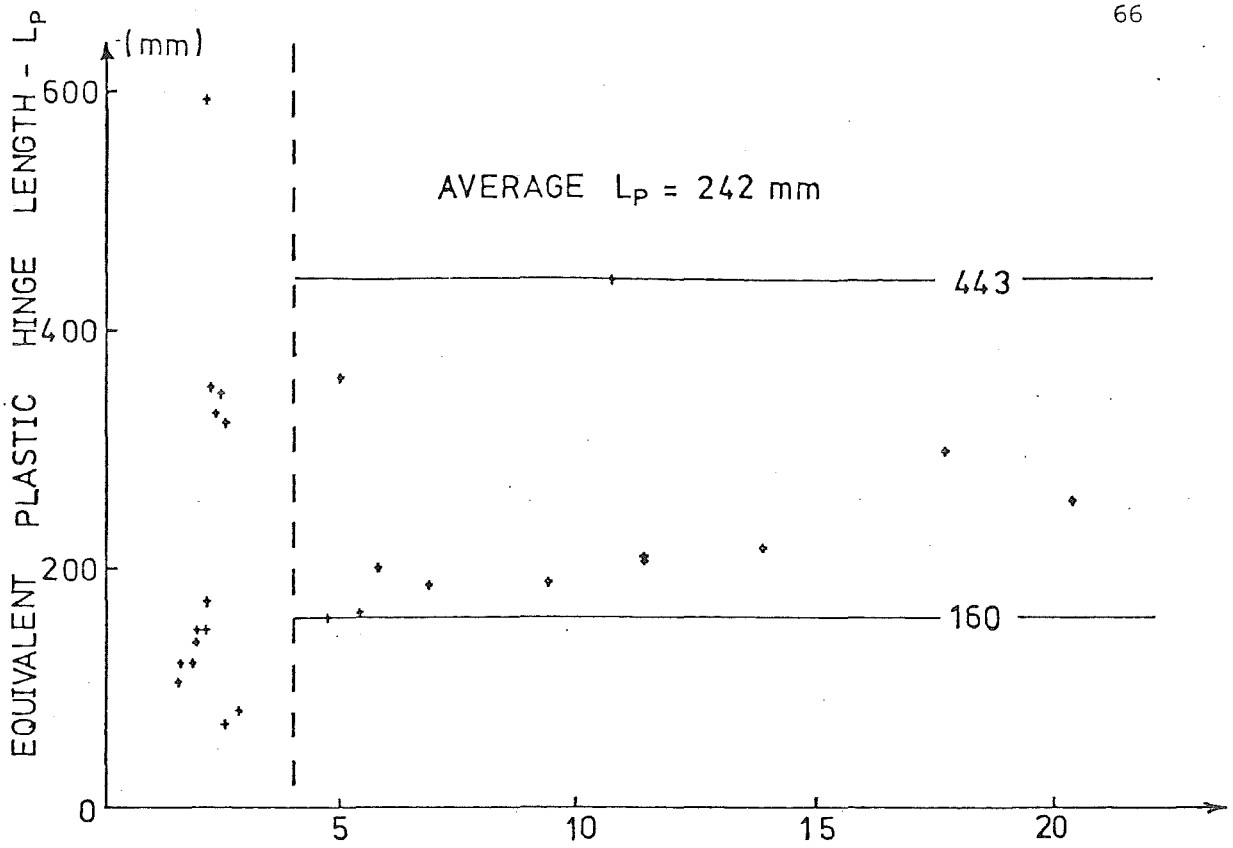

FIG. 4.20 L_p vs μ (UNIT 2)

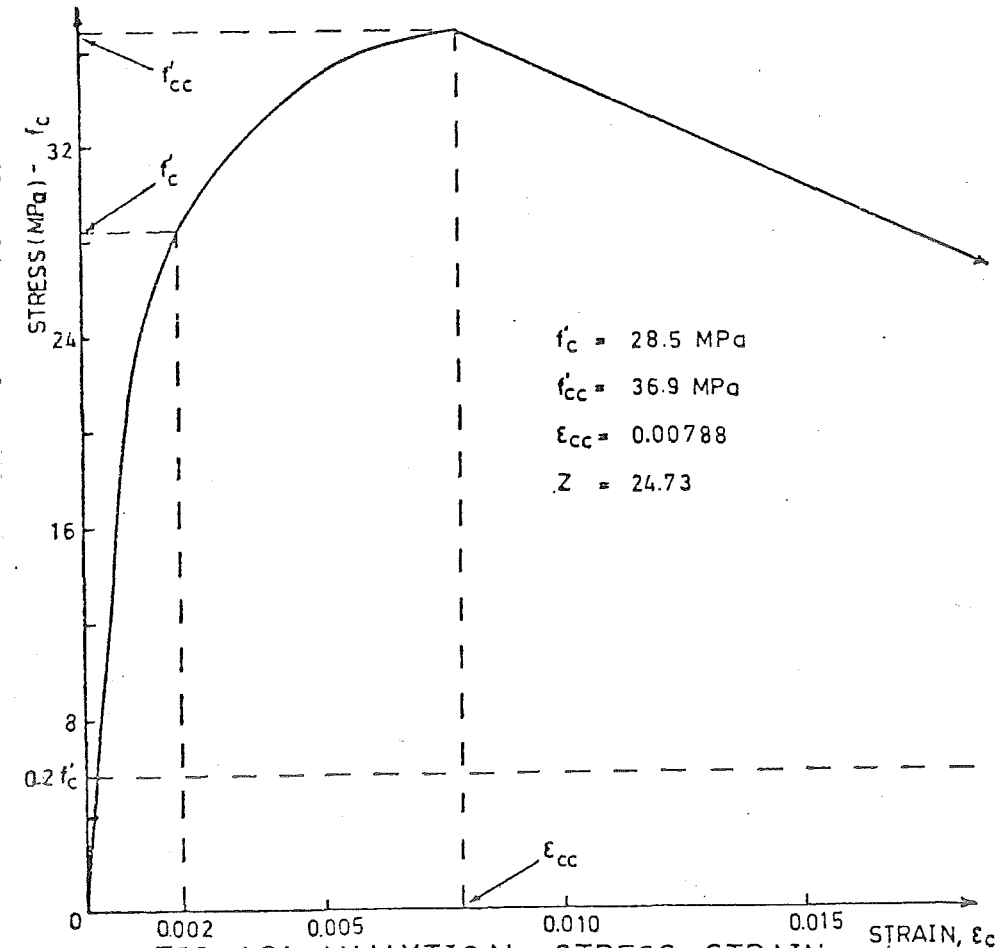

FIG. 4.21 ANALYTICAL STRESS STRAIN CURVE FOR CONFINED CONCRETE — UNIT 2

calculation of f''_{cc} (as spelt out in Section 2.2.1 (h)) gave quite meaningless results as well. This strange behaviour may be due to the fact that the assumption on "the plane sections remain plane" was no longer valid.

4.2.3 Specimen Three

(a) General description

The lateral loading sequence in the elastic cycle was 60 kN, 120 kN, 180 kN and then 207 kN. After the first cycle, all other cycles had 60 kN increments in their initial load controlling stage before $\mu_o = 1$. Due to an initial error in calculating the theoretical ultimate moment, the Δ_y initially measured was smaller than it should have been. The displacement ductility factors were later corrected by using the correct measured Δ_y value. Hence the overall values for μ_o were 1.53, 3.06, 4.59, 6.12 and 7.65 instead of 2, 4, 6, 8 and 10, (Fig. 4.22a).

Cracks started to appear in the elastic cycle at 207 kN and by $\mu_o = 1.53$, more cracks appeared and started to show inclination. On further loading, the cracks deepened and crossed each other. The cracking zone extended to about 800 mm from the centre block after $\mu_o = 3.06$.

Crushing commenced at $\mu_o = 1.53$. It was more extensive at the bottom plastic hinge than on top. By $\mu_o = 3.06$ crushing extended to 250 mm from the centre block and on the following reversed cycle it extended to 400 mm. The crushing zone also extended sideways to the centroidal axis at $\mu_o = 6.12$ while lengthwise it extended to 500 mm at the bottom plastic hinge and 300 mm on top.

At the last cycle of $\mu_o = 7.65$ incipient sign of buckling of longitudinal bars was observed at the bottom plastic hinge and the fracture of these bars under dynamic loading (five cycles at $\mu_o = 6.12$ and three cycles at $\mu_o = 7.65$, Fig. 4.22b) brought about the failure of this specimen.

(b) Yield displacement and yield curvature derivation

The same method was employed in the derivation of the measured yield displacement and yield curvature, except that the 75% ultimate load level was found by extrapolating the experimentally obtained curves (Fig. 4.22a). By doing so, the correct measured Δ_y was found to be 6.6 mm as compared to the calculated theoretical value of 7.1 mm, showing good agreement.

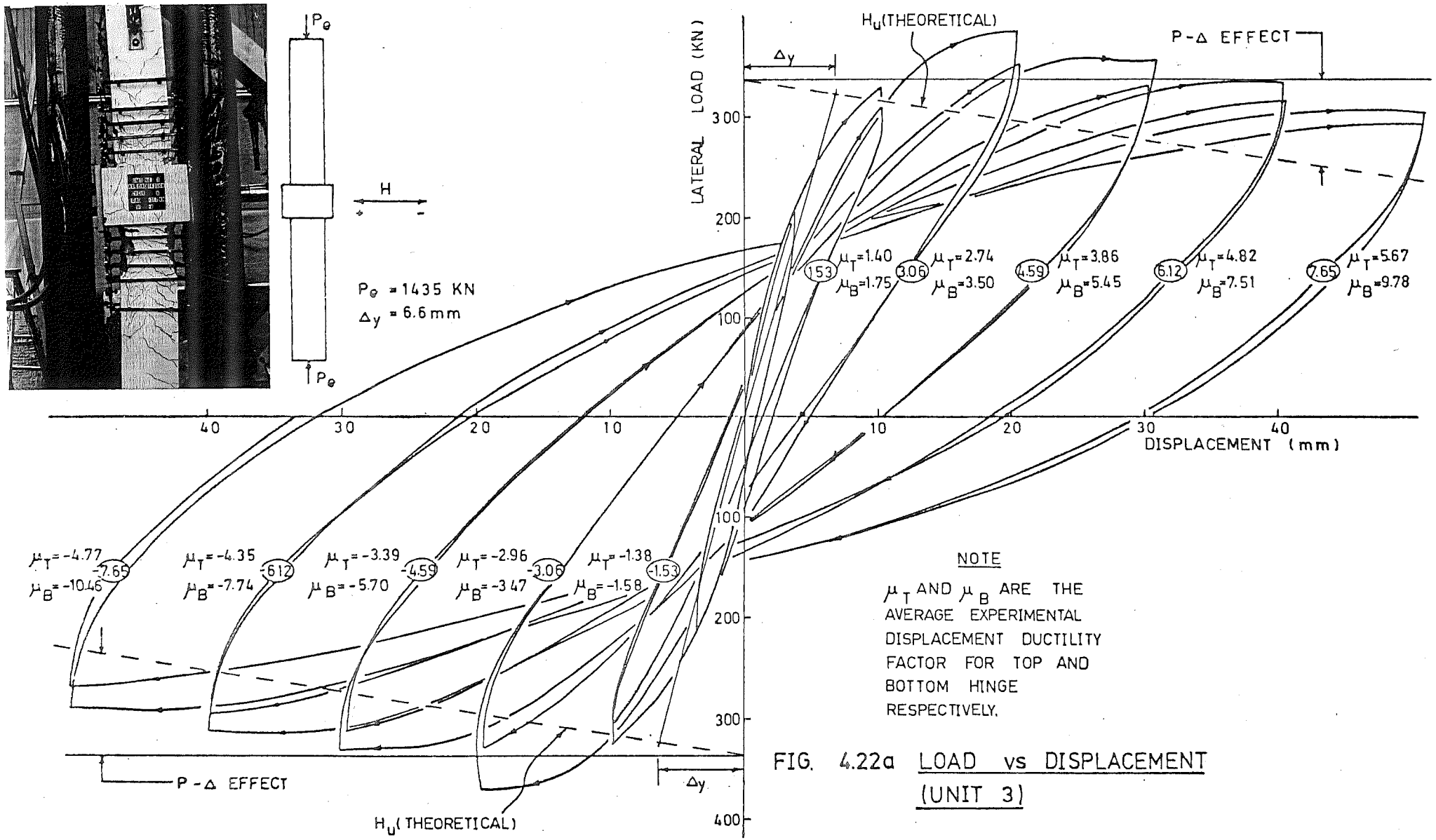

FIG. 4.22a LOAD vs DISPLACEMENT (UNIT 3)

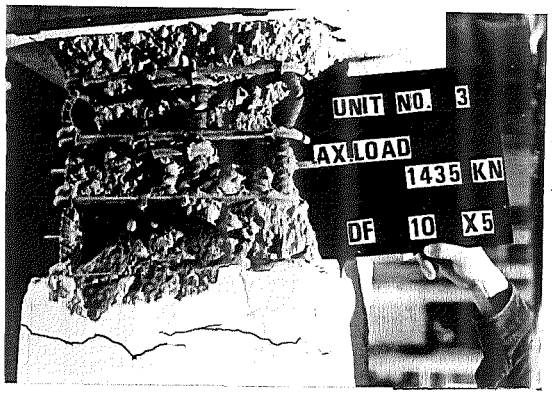

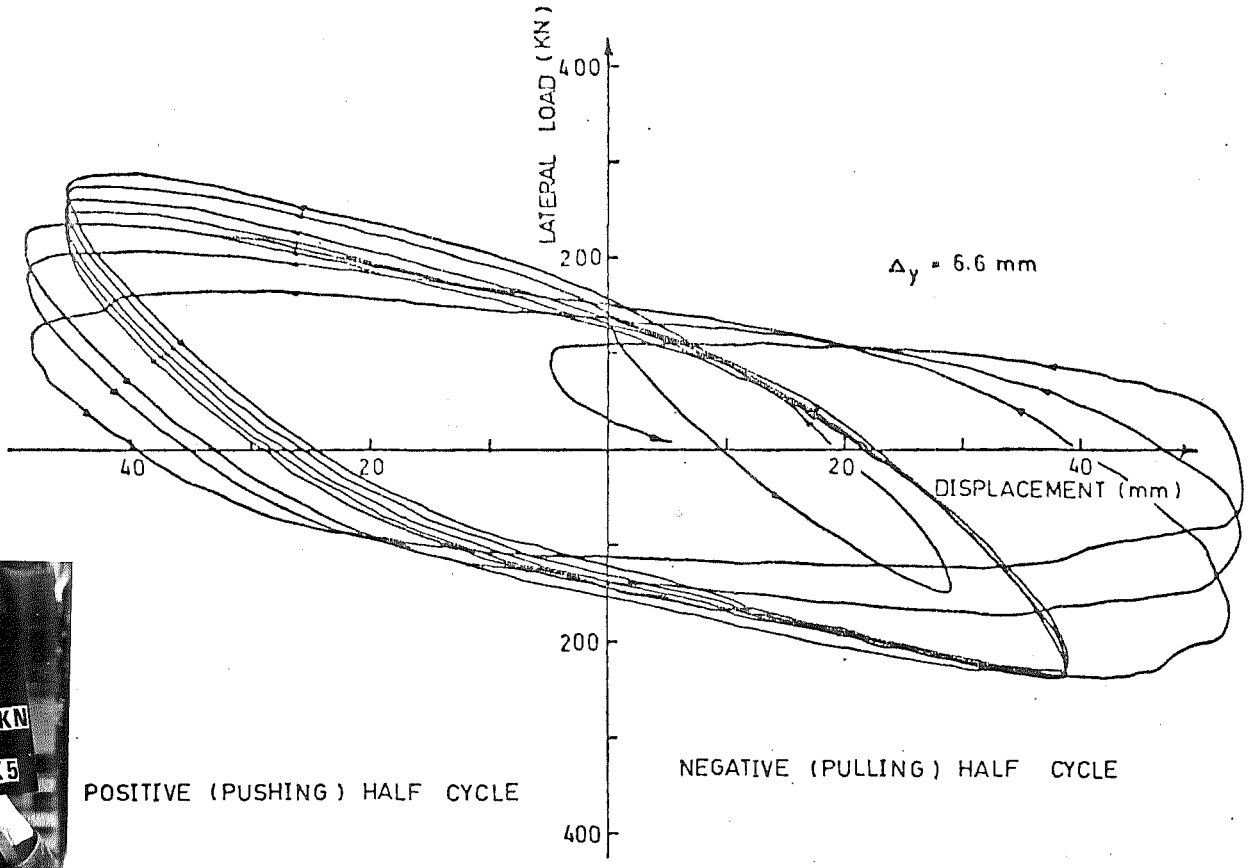

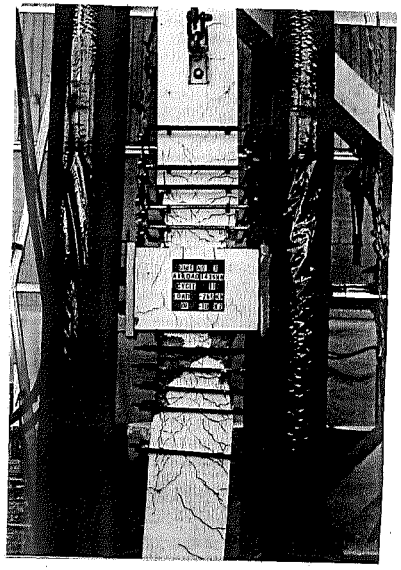

FIG. 4.22b DYNAMIC CYCLES AT $\mu_\circ$=6.12 & 7.65 (UNIT 3)

The measured yield curvature was again found to be about twice the theoretical value (7.7×10^{-6} rad/mm) obtained by using Equation 13. Fig. 4.23.

(c) Lateral load vs displacement curves

Since the longitudinal bars were not equally spaced, ACI design charts were not used in the determination of ultimate moment. The trial and error approach gave value for ultimate moment of 270 kNm.

As this is the high axially loaded specimen of the two square sections the P-Δ effect was quite significant. However, as expected the peak loads were still greater than the theoretical values. The degradation of stiffness was not significant during the static loading stage. Even in the dynamic loading stage much of the stiffness degradation occurred only at the last three cycles of $\mu_o = 7.65$ (see Fig. 4.22b). Nevertheless, there was still a significant load carrying capacity.

(d) Curvature profiles and curvature ductility

The curvatures were calculated in the same way as stated in section 4.2.1(d) except that the distance between a pair of gauges was 600 mm instead of 500 mm. As it was felt that not much information would be gained from the sixth gauges furthest away from the centre-block, they were not used in the test. The general pattern (Fig. 4.24) shows that most of the rotation was concentrated near the centre block. However, in the case of the bottom plastic hinge which had relatively higher curvature, there was not so much concentration and the region of high curvature extended to about 400 mm from the centre block.

The maximum curvature ductility was found to be 10 (at bottom plastic hinge) using the measured ϕ_y, as compared to 19 by using the ϕ_y calculated theoretically.

(e) Transverse steel strain

The readings were taken manually using the Budd bridge. Referring to Fig. 2.8(b), the average of the three shear strain readings of strain gauges A, B and C was taken as representative. Due to their locations, the strain gauges for measuring confining strains were in tension zone when the specimen was under positive lateral loadings. Hence, for clarity, their readings for positive μ_o values were neglected. (Fig. 4.25).

Only during the last three cycles (i.e. at $\mu_o = 7.65$), did the hoop

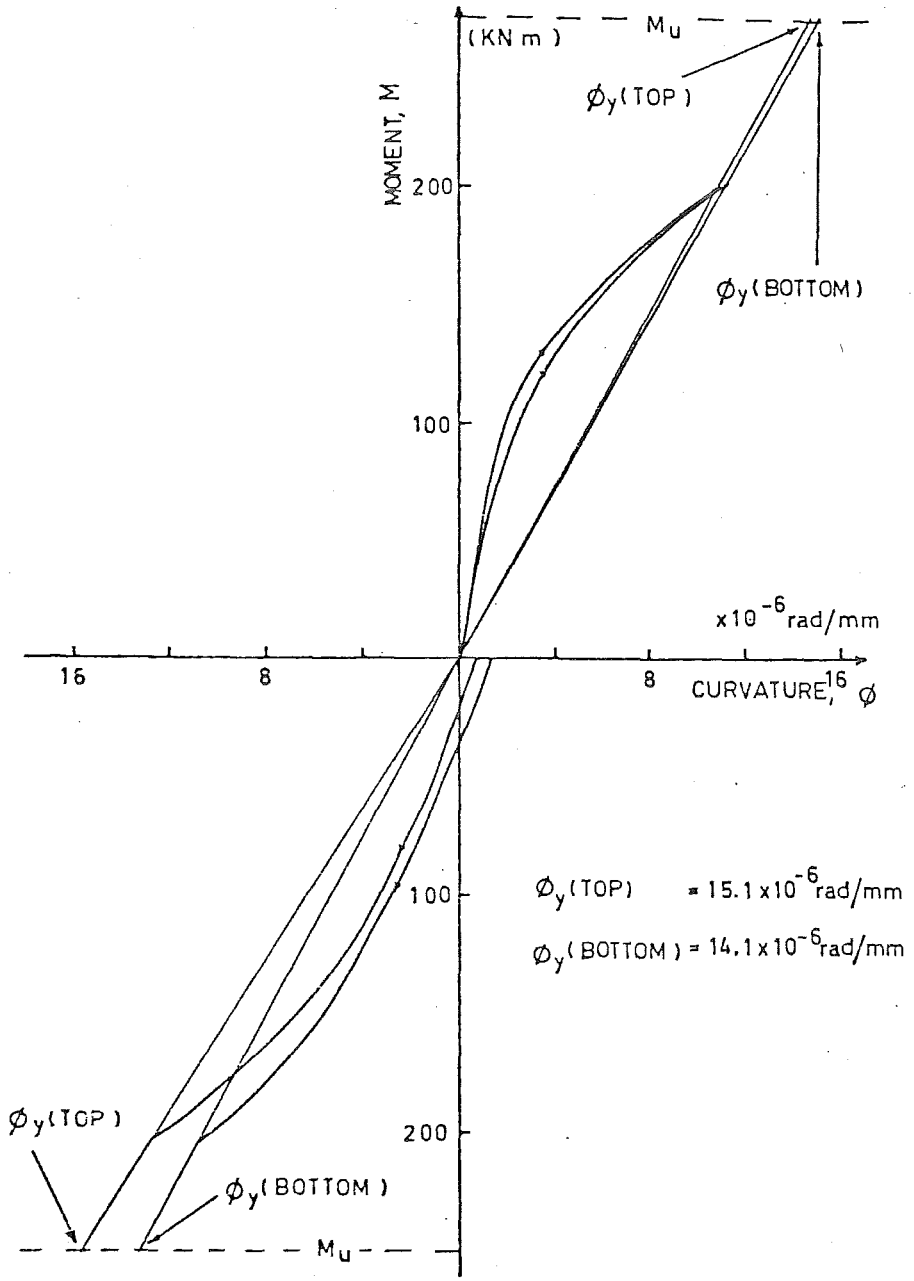

FIG. 4.23 YIELD CURVATURE (UNIT 3)

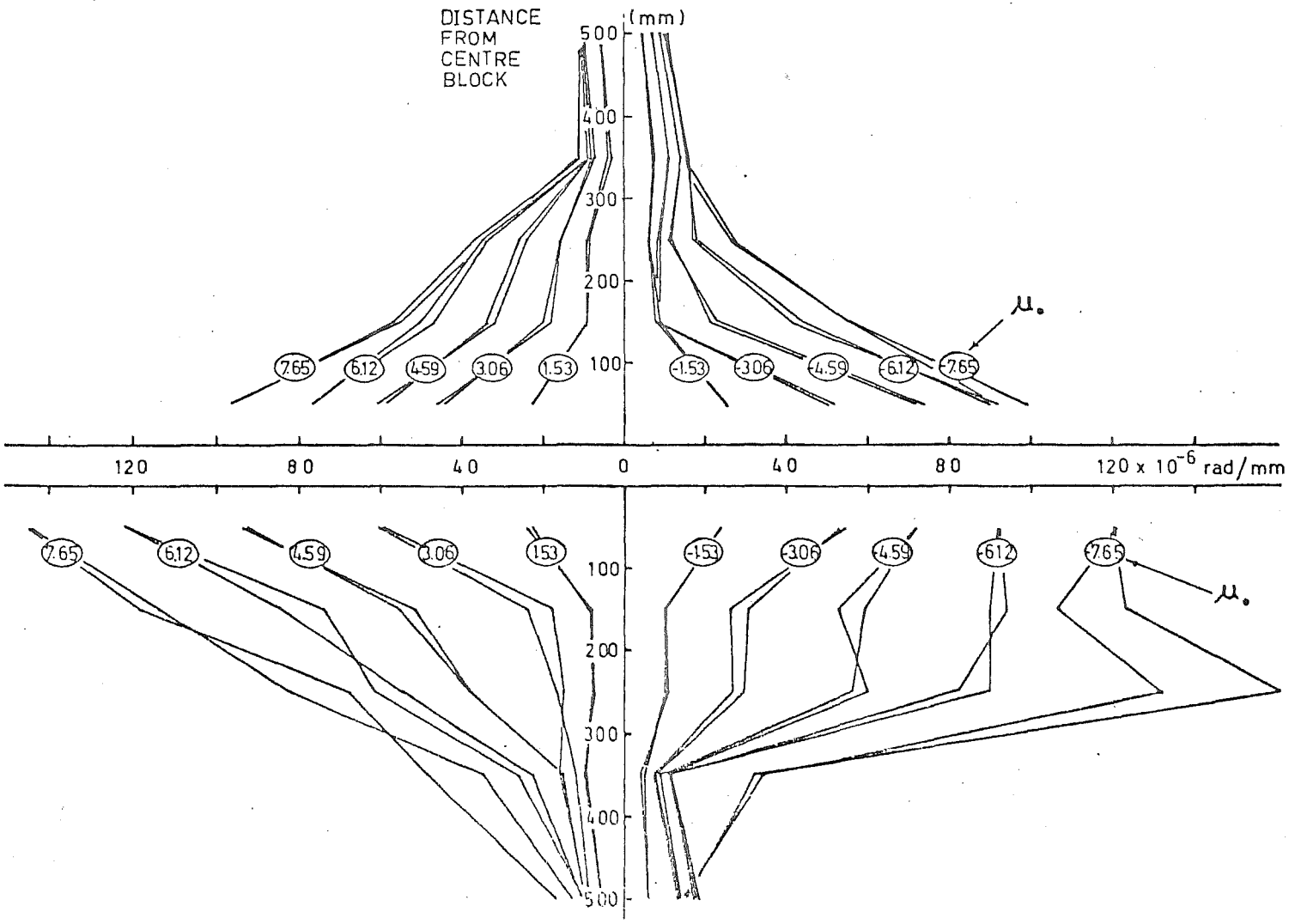

FIG. 4.24 MEASURED CURVATURE PROFILE (UNIT 3)

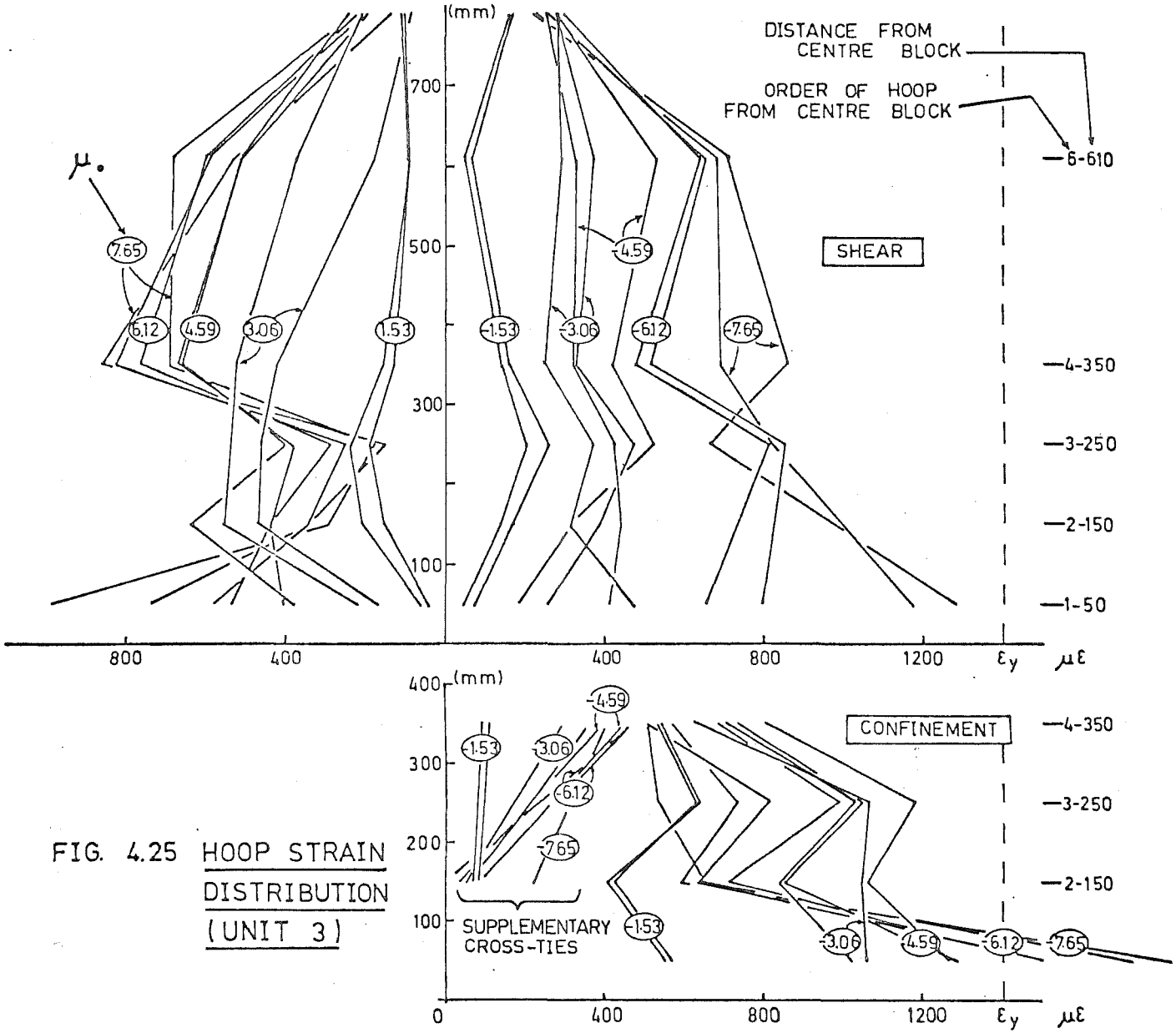

FIG. 4.25 HOOP STRAIN DISTRIBUTION (UNIT 3)

nearest to the centre block yield. For all other earlier cycles, there was hardly any yielding at all. This was particularly so for the supplementary cross-ties whose main function was not for confinement at such early stage of loading.

The shear strains were more evenly distributed but still none of the hoops did yield. Anyway, this shear strain distribution was used to determine the maximum shear force carried by the transverse steel so as to find the shear carrying capacity of the concrete.

(f) Maximum concrete compression strain

The extreme fibre concrete compression strains were measured and plotted against μ. The curve was fitted as shown in Fig. 4.26 and the maximum concrete compression strain was found to be 0.0232.

(g) Equivalent plastic hinge length

The plastic hinge lengths calculated were plotted against μ and the average value (295 mm) and the upper and lower bounds for the points in the region where $\mu > 4$ were noted (Fig. 4.27). In fact, even for those points outside the region, the majority of them still came within the two bounds. Hence, indicating a more uniform distribution than that of other specimens.

(h) Idealized stress-strain curve

Only the modified analytical confinement models proposed by Park and Kent (3) was considered in this investigation. Fig. 4.10 b shows the idealized stress-strain curve of the model and the characteristics of the curve are described below.

Region AB: $0 \leq \varepsilon_c \leq 0.002K$. A second degree parabola is assumed taking into account the enhancement of concrete strength by confinement.

$$f_c = Kf'_c \left[\frac{2\varepsilon_c}{0.002K} - \left(\frac{\varepsilon_c}{0.002K} \right)^2 \right] \qquad (23)$$

where $$K = 1 + \frac{\rho_s f_{yh}}{f'_c} \qquad (24)$$

Region BC: $0.002K \leq \varepsilon_c \leq 20c$. A linear falling branch is assumed.

$$f_c = Kf'_c \left[1 - z_m (\varepsilon_c - 0.002K) \right] \qquad (25)$$

where $$z_m = \frac{0.5}{\frac{3 + 0.29f'_c}{145f'_c - 1000} + \frac{3}{4}\rho_s\sqrt{\frac{h''}{s_h}} - 0.002K} \qquad (26)$$

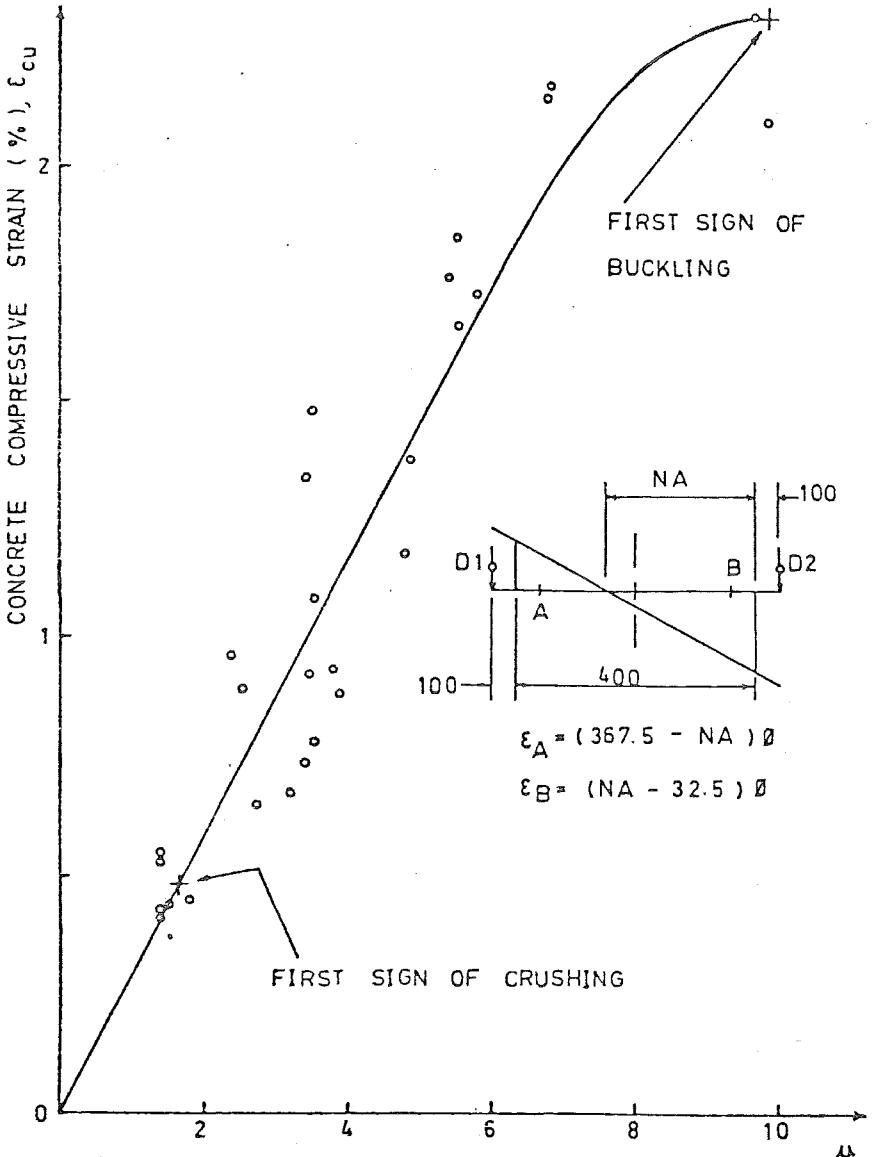

FIG. 4.26 ε_{cu} vs μ (UNIT 3)

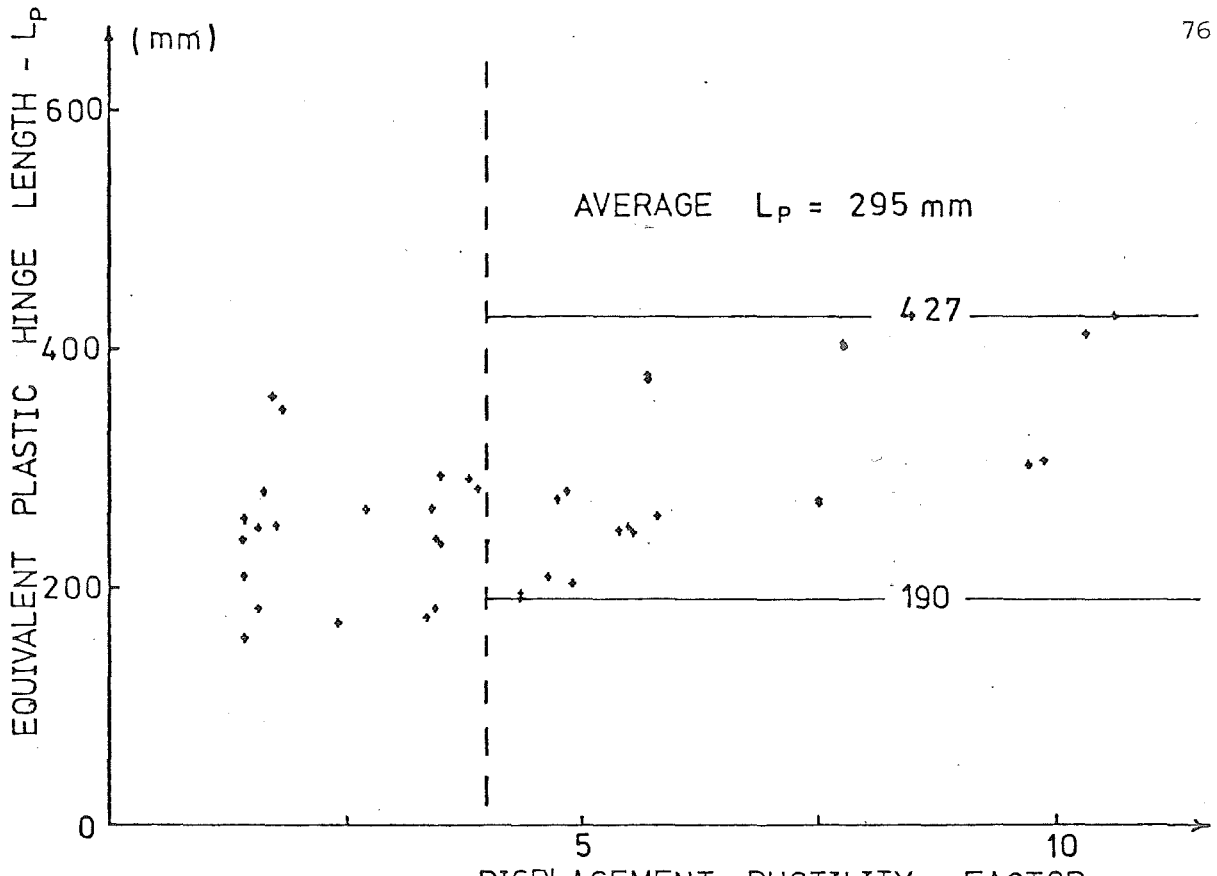

FIG. 4.27 L_p vs μ (UNIT 3)

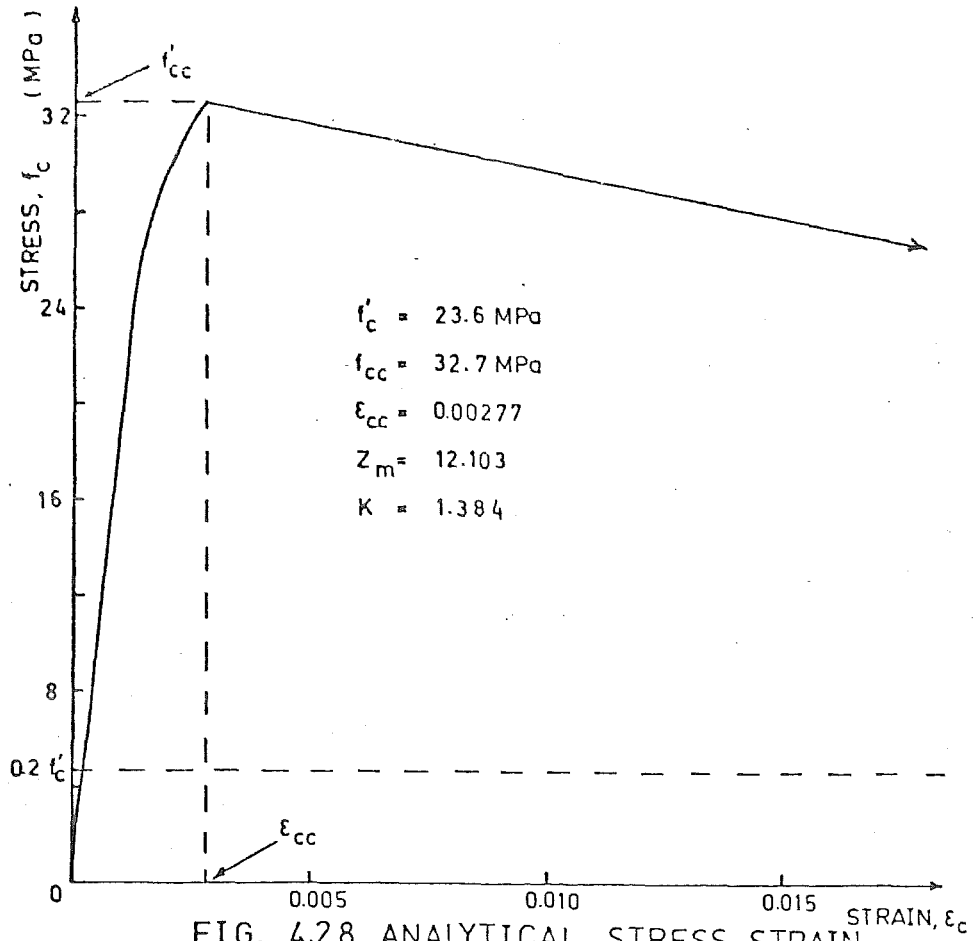

FIG. 4.28 ANALYTICAL STRESS-STRAIN CURVE FOR CONFINED CONCRETE (UNIT 3)

Region CD: $\varepsilon_c > \varepsilon_{20c}$. It is assumed that concrete can sustain a compressive stress of $0.2f'_c$ indefinitely.

For specimen three, K = 1.384, z_m = 12.103 (Fig. 4.28). By using this idealized stress-strain curve the moment corresponding to $\varepsilon_{cu} = 0.02$ was 292 kNm and that corresponding to maximum experimental ε_{cu} (0.0232) was 296 kNm.

The modified Park-Kent stress-strain curve assumed the efficiency of rectangular hoops in confinement to be about half that of circular spirals. Thus

$$f'_{cc} = Kf'_c$$

$$= \left(1 + \frac{\rho_s f_{yh}}{f'_c}\right) f'_c \qquad (27)$$

and f'_{cc} was 32.7 MPa (ε_{cc} = 0.00277) in this case. However, if the approach outlined in Section 4.2.1(h) was used this value would be 38.0 MPa.

4.2.4 Specimen Four

(a) General description

In the elastic cycle, the lateral loading sequence was 60 kN, 120 kN, 180 kN and 241 kN. All the subsequent cycles had 60 kN increments until the loading was controlled by predetermined displacements at μ_o= 1, 1.5, 2, 2.5 and so on.

Cracks appeared during the third increment, i.e. at 190 kN. They lengthened and showed inclination at μ_o= 2 . The zone of cracking occupied a region of about 800 mm adjacent to the centre block.

Crushing of concrete first occurred at μ_o= 2 and it became more extensive in the top hinge during subsequent loadings. After the first cycle of μ_o= 4, the crushing zone at the top hinge had extended to 450 mm from the centre block. Spalling occurred right back to the main bars.

By the end of the second cycle of μ_o= 6 , the longitudinal steel in the top plastic hinge buckled and this continued in the following cycles. The fracture of these bars during dynamic loadings ended the test. Six cycles of dynamic loading at μ_o= 6 were carried out and the hysteresis loops were as shown in Fig. 4.29b.

(b) Yield displacement and yield curvature derivation

The Δ_y obtained experimentally was 9.3 mm whereas that obtained theoretically was only 6.8 mm.

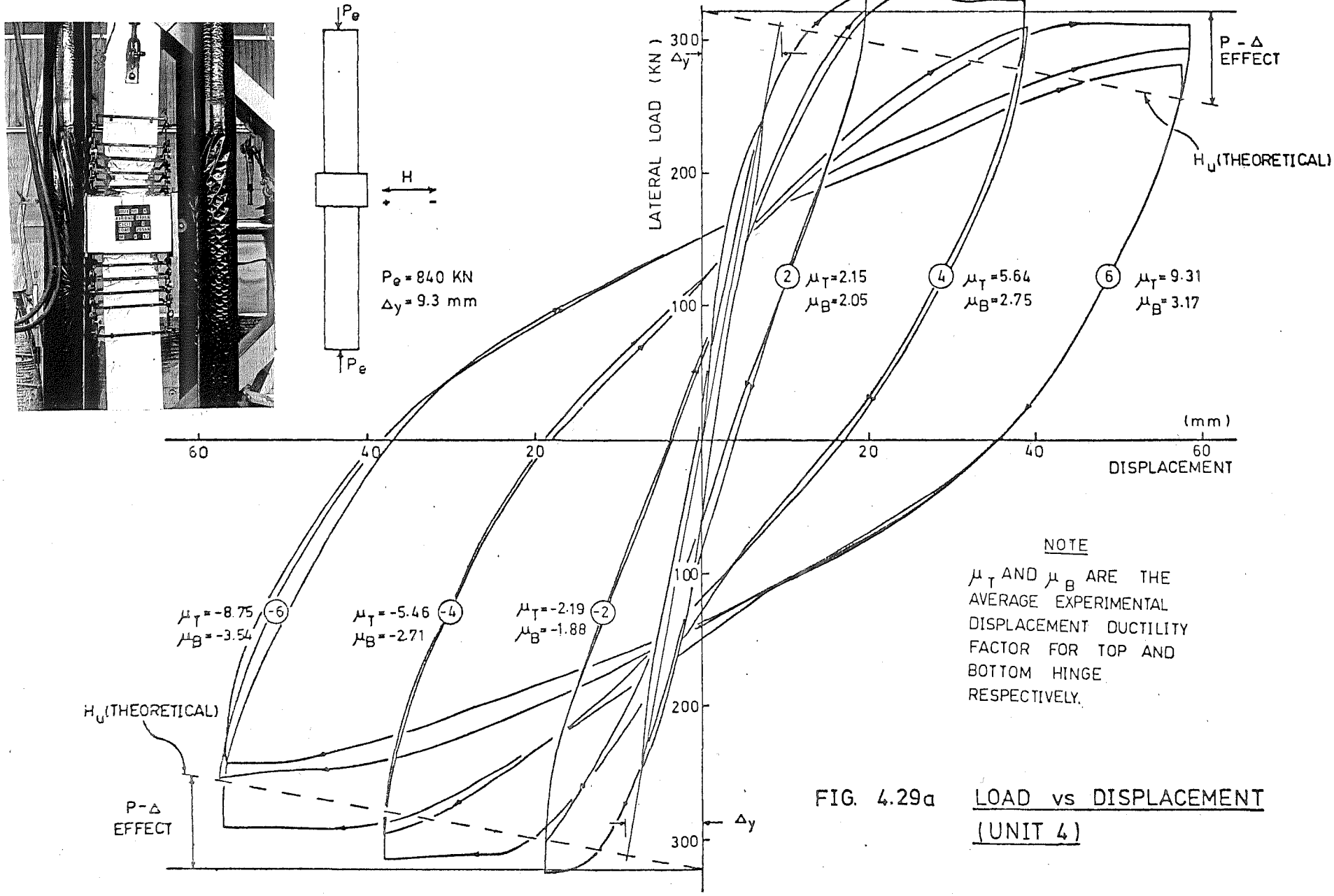

FIG. 4.29a LOAD vs DISPLACEMENT (UNIT 4)

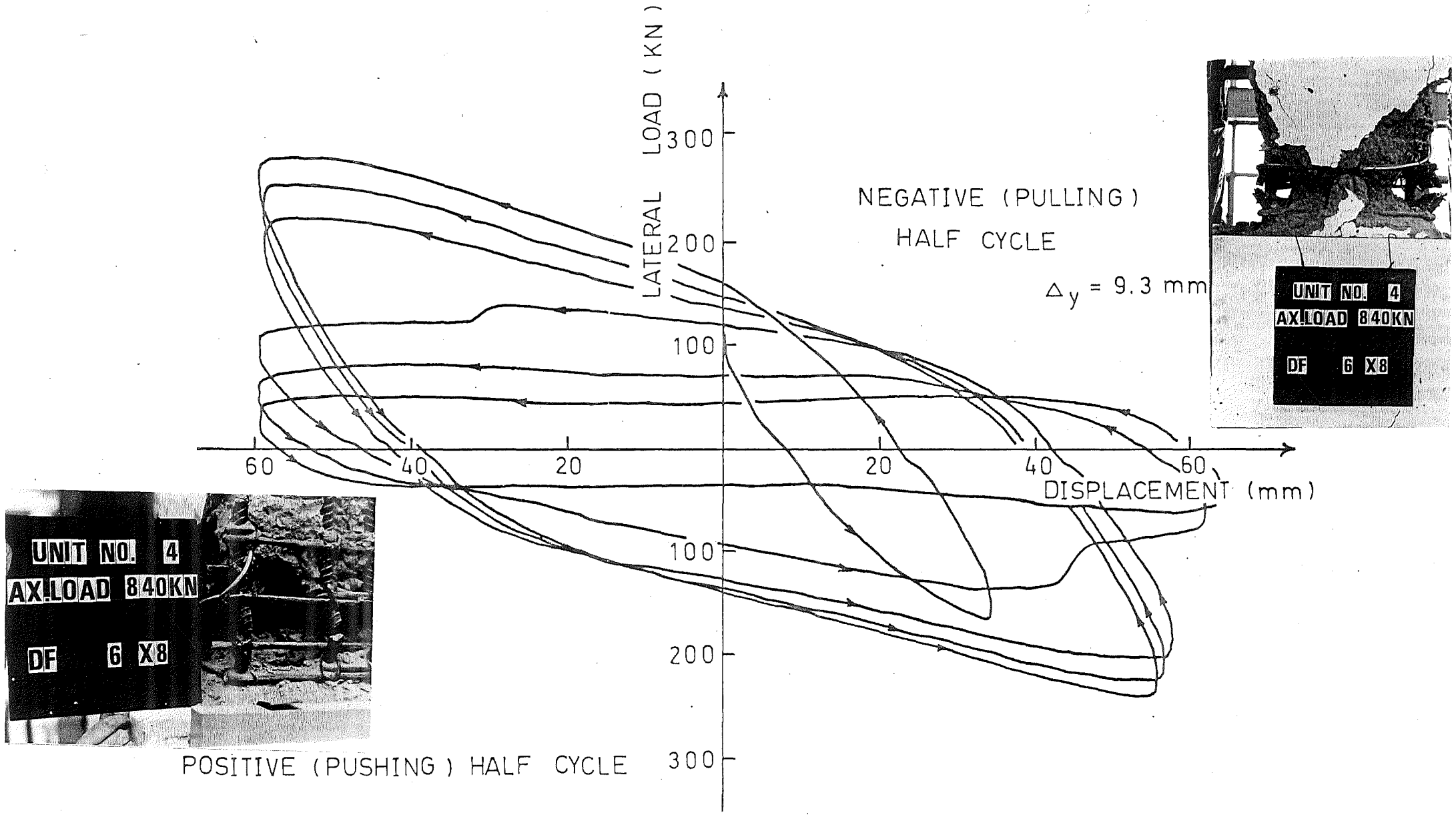

FIG. 4.29 b DYNAMIC CYCLES AT $\mu_\circ = 6$ (UNIT 4)

Also, the discrepancy between the experimentally obtained ϕ_y (Fig. 4.30) value and the calculated value (10.9×10^{-6} rad/mm) was again a factor of 2, i.e. the former is twice the latter.

(c) Lateral load vs displacement curves

Due to the large Δ_y value and the limited travel of the hydraulic jack, only lateral loading to $\mu_o = 6$ was achieved.

The theoretical ultimate moment of resistance was 257 kNm which when taken into account of the $P\text{-}\Delta$ effect gave rise to a dropping theoretical load, Fig. 4.29a. This drop was gradual because of low axial load.

All the curves demonstrated good energy dissipating capacity with little strength and stiffness degradation. The $P\text{-}\Delta$ effect was not so pronounced in this case and the peak loads were well above the theoretical load.

The first three cycles of dynamic loading at $\mu_o = 6$ still showed a very good performance but the last three cycles showed the degradation of stiffness while the specimen still retained some load carrying capacity. Fig. 4.29.

(d) Curvature profiles and curvature ductility

Only 5 pairs of dial gauges in each plastic hinge were used. Contrasting to the other units, the fourth specimen had most of its rotation concentrated at the top plastic hinge (Fig. 4.31). The general pattern was still similar to that of specimen one and three, with curvature increasing towards the centre block.

The difference in the theoretical and experimental ϕ_y values gave rise to two different curvature ductility factors; $\frac{\phi_u}{\phi_y} = 22$ for the former and $\frac{\phi_u}{\phi_y} = 11$ for the latter. The new instrumentation for curvature measurement (section 2.3.1) failed to give a good correlation in the results with existing procedure. It did not show any variation in curvature as the value of μ was increased.

(e) Transverse steel strain

Not surprisingly, the transverse hoops were far from reaching yield because the strain gauges monitoring the strains were located in the bottom plastic hinge which remained intact while the top plastic hinge was loaded to destruction.

It was evident in Fig. 4.32 that the supplementary cross-ties were hardly stressed whereas the peripheral hoops were stressed with an

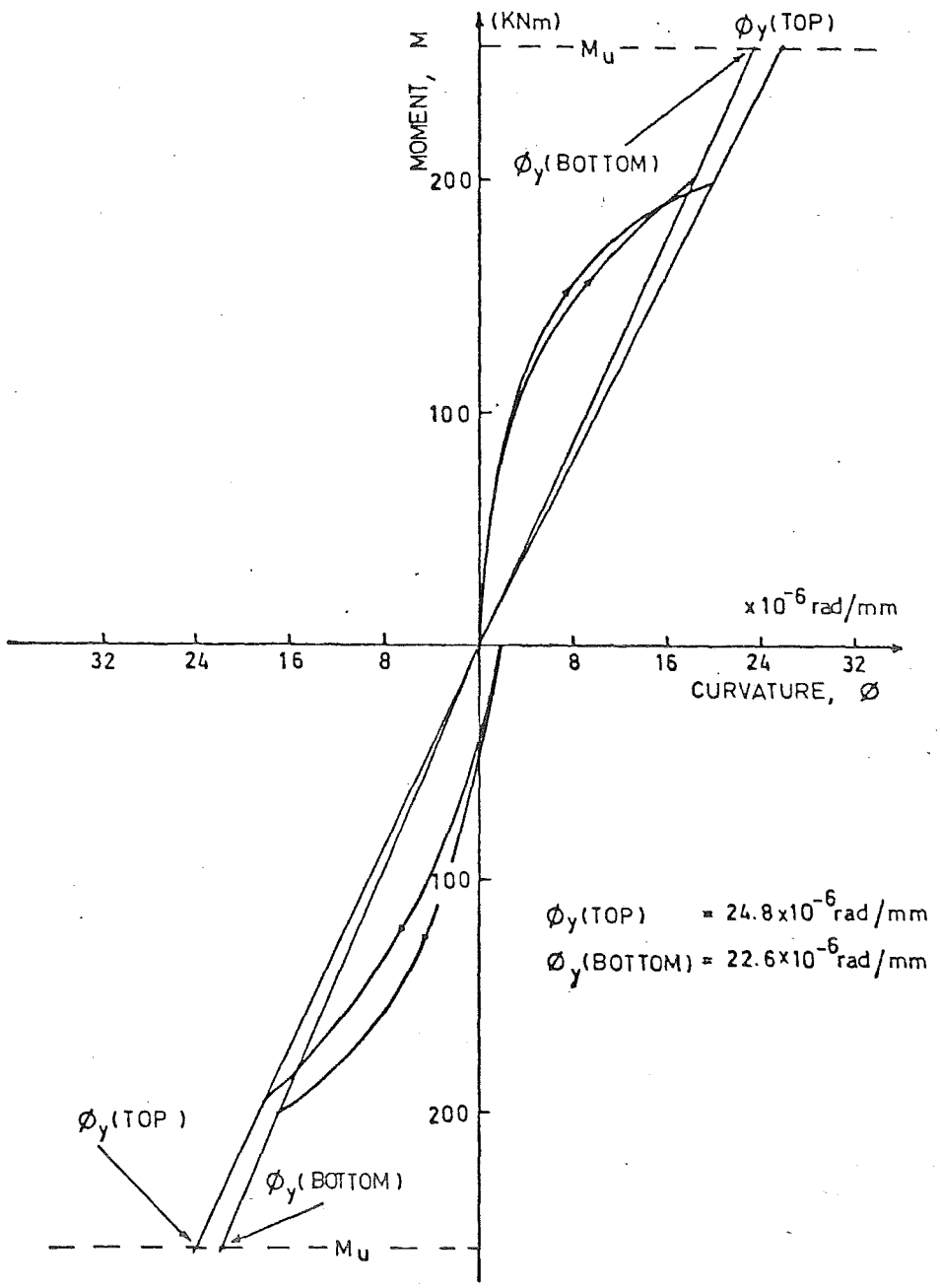

FIG. 4.30 YIELD CURVATURE (UNIT 4)

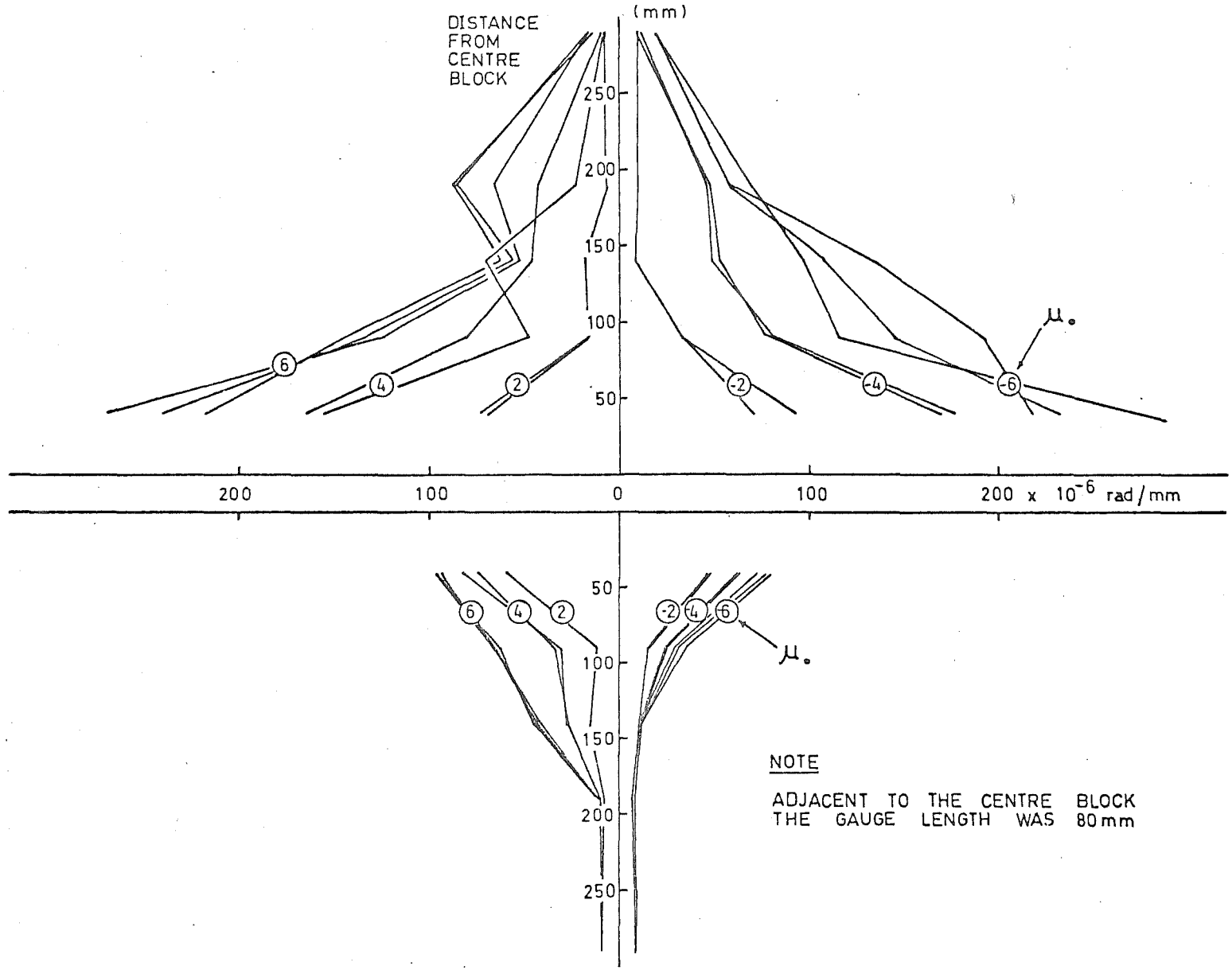

FIG. 4.31 MEASURED CURVATURE PROFILE (UNIT 4)

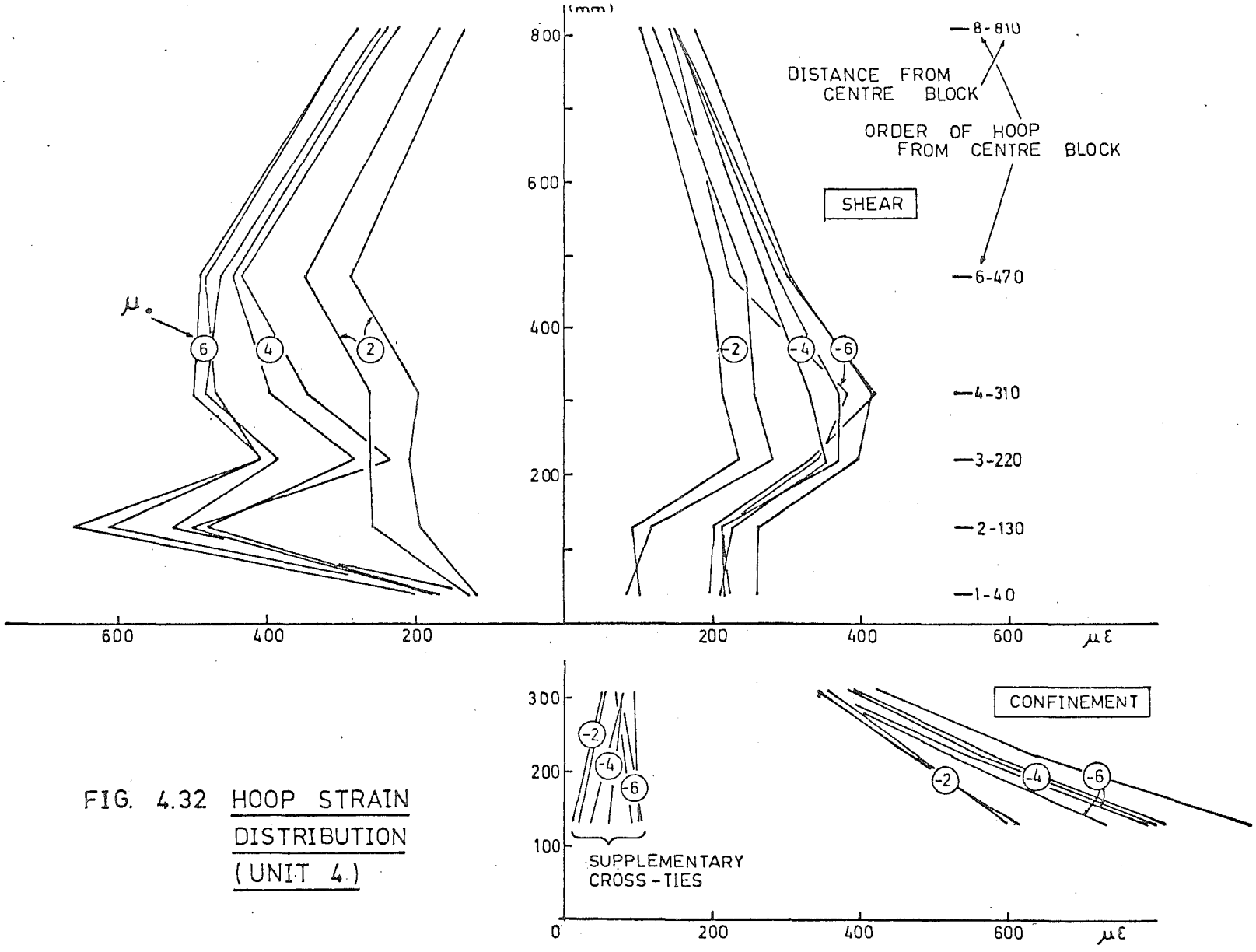

FIG. 4.32 HOOP STRAIN DISTRIBUTION (UNIT 4)

approximately linearly decreasing intensity away from the centre block. As there was no strain gauge for measuring confining strain nearer to the centre block, the confining effect of the centre block cannot be further confirmed. Nevertheless, it was quite obvious in Fig. 4.29b which shows up clearly the conical zone of influence of the centre-block.

The shear strain results were quite consistent. None of the shear steel had yielded. Even in the top plastic hinge the check gauge indicated a maximum strain of only 1100 με during the last cycle of loadings. Anyhow, these shear strain results were used in the determination of shear distribution between concrete and steel.

(f) Maximum concrete compression strain

The plot of ε_{cu} vs μ is as shown in Fig. 4.33. The relation was approximated by a straight line followed by a curve to maximum ε_{cu} of 0.0359.

(g) Equivalent plastic hinge length

Without exception, the plot of equivalent plastic hinge length against μ did not show any dependence of plastic hinge length on the displacement ductility level. The average of those points in the region where $\mu > 4$ was 220 mm. The upper and lower bounds were also drawn in Fig. 4.34 as well.

(h) Idealized stress-strain curve

Following Park and Kent's proposal, for this specimen,

$$k = 1.248$$
$$z_m = 14.596$$
$$f'_c = 31.2 \text{ MPa}$$
$$\varepsilon_{cc} = 0.00250$$

but the f''_{cc} value calculated using the other method (section 4.2.1(h)) was 40.2 MPa.

The idealized stress-strain curve of this specimen is given in Fig. 4.35.

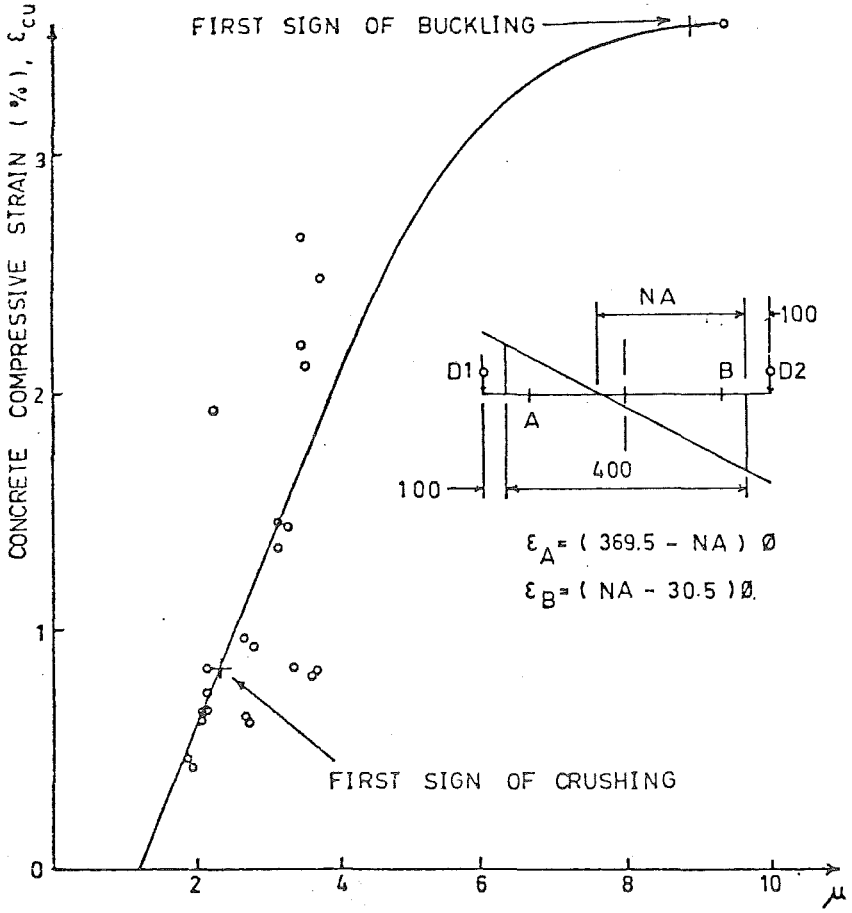

FIG. 4.33 ε_{cu} vs μ (UNIT 4)

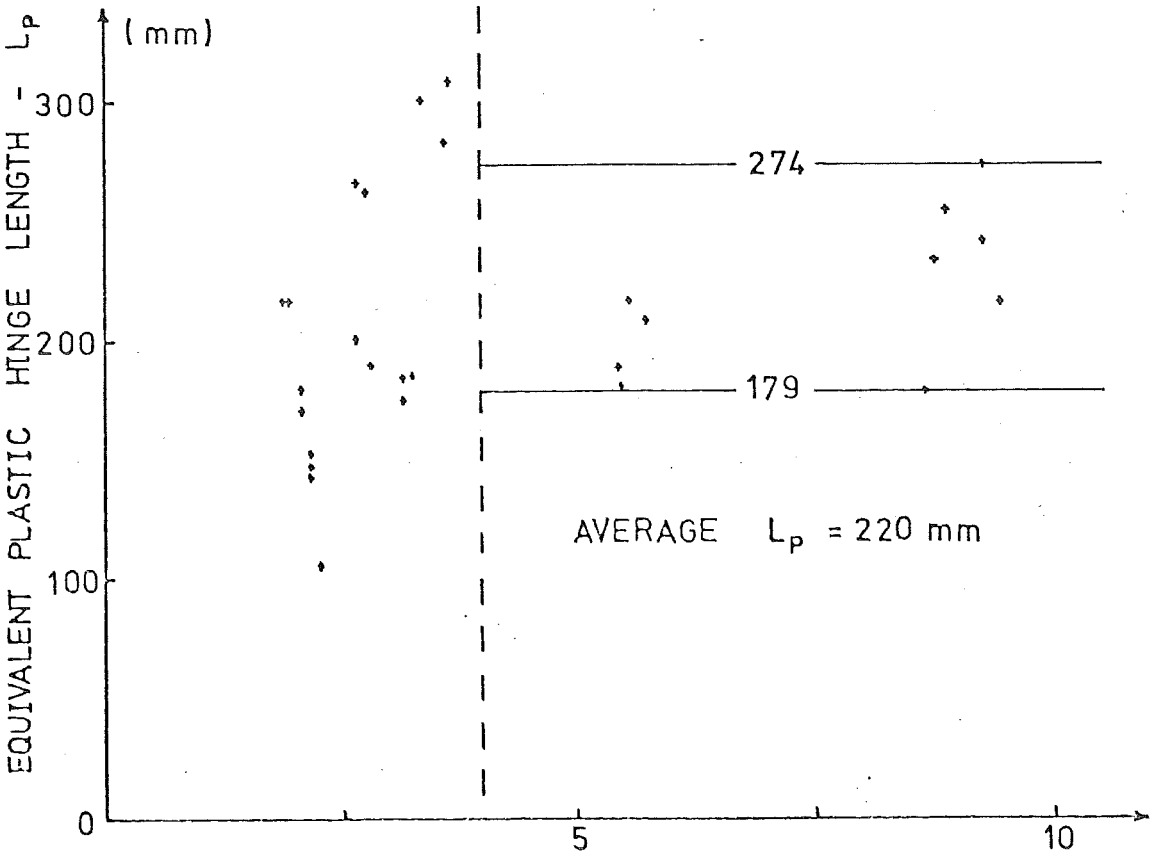

FIG. 4.34 L_p vs μ (UNIT 4)

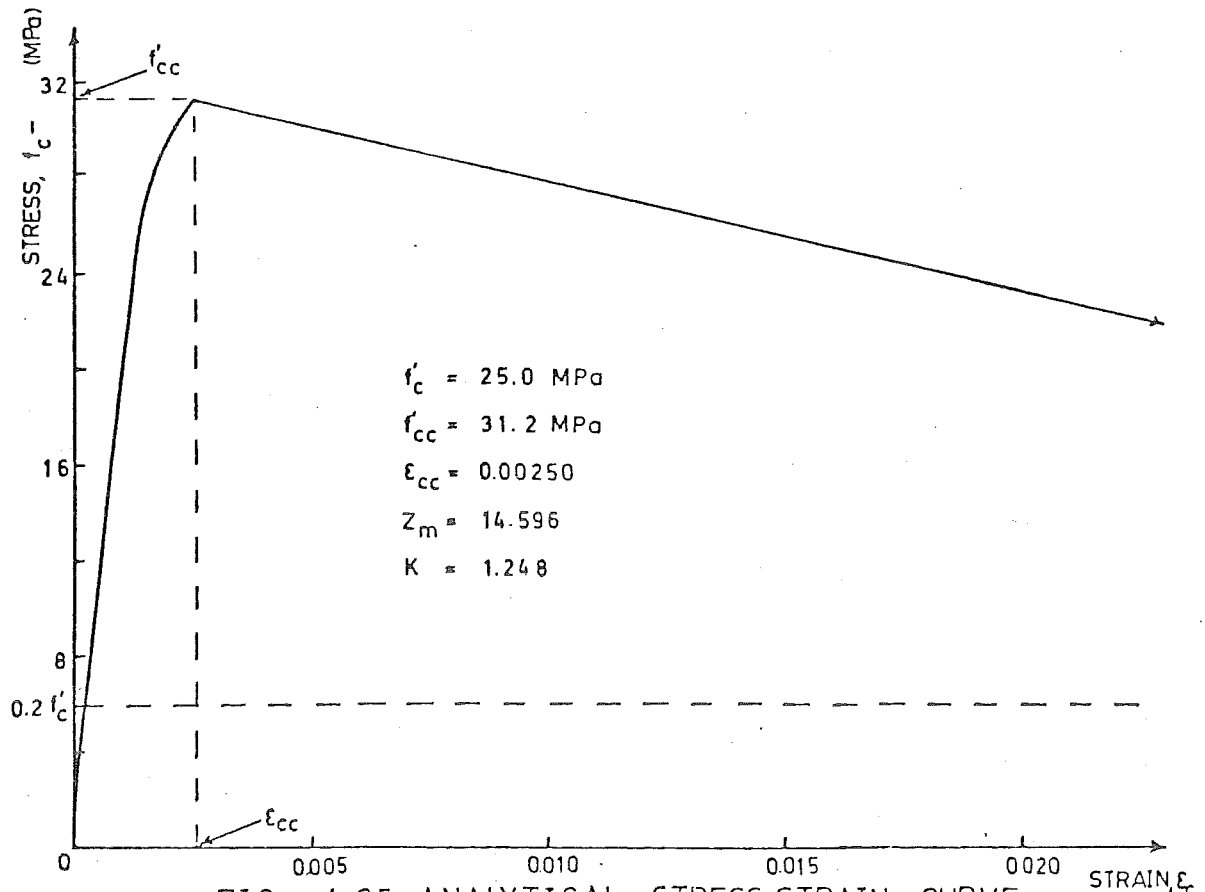

FIG. 4.35 ANALYTICAL STRESS-STRAIN CURVE FOR CONFINED CONCRETE (UNIT 4)

CHAPTER FIVE

DISCUSSION OF RESULTS

5.1 DEFLECTION BEHAVIOUR

Excellent stability of hysteresis loops is apparent in Figs. 4.2, 4.13, 4.22 and 4.29. Similar to that revealed in Gill's and Potangaroa's tests, there was only a little strength degradation occurring on cycling to constant ductility factors and no significant sign of degradation of shear strength as evidenced by the pinching of the loops. The slight strength and stiffness degradation at high ductility factors may be attributed mainly to the spalling of cover concrete.

It can be seen that even the hysteresis loops for dynamic loadings (Figs. 4.2b, 4.22b and 4.29b) demonstrated such stability during the initial cycles. Severe degradation occurred only during the last three cycles and even at completion of testing the piers still could sustain some load carrying capacity (about 30% to 50% of the theoretical ultimate load).

Unlike results of the testing of squat units in Gill's and Potangaroa's works, the longitudinal steel in all units started to show incipient signs of buckling between the range of $\mu = 9$ to $\mu = 11$. It was the fracture of these buckled bars that brought about the failure of the specimens.

5.2 CONCRETE COMPRESSION STRAINS

Except for Unit Three which had the smallest concrete cylinder strength, f'_c, the first visible crushing strain was 0.0084, Table 5.2, well in excess of the traditionally adopted value of 0.003. Even the smallest crushing strain of 0.005 (in Unit 3) was greater than this assumed value, confirming the conservative nature of the assumption. The first sign of crushing appeared as the specimens were loaded to $\mu_o = 2$ for the first time and for the special case of Unit Two, to $\mu_o = 1.5$.

Table 5.2 includes the maximum concrete compression strain measured at the surface of the confined concrete core over the gauge length nearest to the centre block. With the exclusion of Unit Two, this maximum value had an average value of 0.033 and occurred at about $\mu = 10$. The exceptional case of Unit Two has maximum ε_{cu} of nearly 13%.

TABLE 5.1 : ULTIMATE MOMENT CAPACITIES (kNm) AND YIELD DISPLACEMENTS (mm)

UNIT	I_{cr} of Transformed Section ($m^4 \times 10^{-4}$)	Calculated* Δ_y	Experimental Δ_y	Experimental Moment at Maximum ε_{cu} M_{exp}	ACI (ϕ = 1.0)		Trial and Error Method Using f'_c, ε_{cu} = 0.003		Neutral** Axis Depth (mm)
					M_u	$\frac{M_{exp}}{M_u}$	M_u	$\frac{M_{exp}}{M_u}$	
1	9.32	5.1	7.5	262	192	1.36	222	1.18	159 (187)
2	9.50	5.6	6.5	417	200	2.09	219	1.90	263 (350)
3	12.72	7.1	6.6	336	-	-	270	1.24	208 (191)
4	12.54	6.8	9.3	322	-	-	257	1.25	144 (167)

* $\Delta_y = \frac{1}{2} \times \frac{M_u}{E_c I_{cr}} \times 1.6 \times \frac{2}{3} \times 1.6$

** The number in brackets gives the N.A depth at maximum experimental ε_{cu}

TABLE 5.2 : CONCRETE COMPRESSION STRAINS, EQUIVALENT PLASTIC HINGE LENGTHS AND CURVATURE DUCTILITY FACTORS

UNIT	First** Visible Crushing	Experimental Maximum	Plastic Hinge Length, mm ε_{cu} Baker	ε_{cu} Corley	Average Experimental $\mu \geq 4$	Range of L_p $\mu \geq 4$	L_p Baker	L_p Corley	Maximum Experimental Curvature Ductility Factor ϕ_{u/ϕ_y} *
1	0.00837	0.0405 (@ μ = 11)	0.00498	0.00975	216	149 - 267	339	241	12 (24)
2	0.00832	0.1271 (@ μ = 26)	0.00597	0.01161	242	160 - 443	490	249	30 (50)
3	0.00486	0.0232 (@ μ = 10)	0.00883	0.01572	295	190 - 427	440	249	10 (19)
4	0.00839	0.0359 (@ μ = 9)	0.00827	0.01136	220	179 - 274	263	263	11 (22)

* The number in brackets gives ϕ_{u/ϕ_y} value using theoretical ϕ_y

** For Units 1, 3 and 4, first visible crushing occured at $\mu_o = 2$. For Unit 2 it occurred at $\mu_o = 1.5$.

μ_o refers to overall displacement ductility factor.

For comparison, theoretical maximum strains calculated in accordance with equations propoed by Baker and Amarakone (21) and Corley (22) for confined concrete are included.

According to Baker and Amarakone (21),

$$\varepsilon_{cu} = 0.0015\ [1 + 150\ \rho_s + (0.7 - 10\rho_s)\frac{d}{c}] \qquad (28)$$

where ρ_s = ratio of volume of transverse steel to volume of concrete core,

c = neutral axis depth at ultimate moment,

and d = effective depth of member.

The equation proposed by Corley (22) is

$$\varepsilon_{cu} = 0.003 + 0.02\ \frac{b}{L} + [\frac{\rho_s\ f_{yh}}{138}]^2 \qquad (29)$$

where f_{yh} = Transverse steel yield stress in MPa

ρ_s = ratio of volume transversed steel plus compression steel to volume of concrete core,

b = width of member,

and L = distance from critical section to point of contraflexure.

As evidenced by Table 5.2, the values predicted by both equations are very conservative when compared with the maximum experimental strains. However, the agreement between the values predicted by Corley's equation and the peak experimental strains was much better in Gill's test, as reported in Reference 3.

5.3 EQUIVALENT PLASTIC HINGE LENGTHS

Table 5.2 includes experimental plastic hinge lengths, L_p, found from Equations 14-16, using values of ϕ_y obtained experimentally. When plotted against the ductility factor, Figs. 4.9, 4.20, 4.27 and 4.34, there is no obvious relationship between the plastic hinge lengths and μ. The values indicated in the table were the averaged values of L_p in region $\mu \geq 4$ in which the plasticity is considered to have developed fully. The high axially loaded specimens seem to have longer plastic hinge length and the average value for octagonal section is 229 mm (i.e. 0.57h c.f. 0.3h in Potangaroa's tests (2)) and for square section is 258 mm (i.e. 0.64h c.f. 0.4h in Gill's tests (3)), where h = overall section depth.

Also included in Table 5.2 is the theoretical plastic hinge lengths using equations proposed by Baker and Amarakone (21) and Corley (22). Baker and Amarakone suggested the following equation

$$L_p = 0.8\, k_1\, k_3\, (\frac{c}{d})\, L \qquad (30)$$

where k_1, k_3 = factors depending on concrete and steel strengths

c = neutral axis depth at ultimate moment,

d = effective depth of member,

and L = distance from critical section to point of contraflexure.

Using the same notations, Corley's equation is

$$L_p = 0.5d + \sqrt{d}\, (\frac{L}{d}) \qquad (31)$$

Baker's approach gave unnecessarily high value at high axial loads because of the over-emphasis of the importance of the $\frac{c}{d}$ value of his equation. Corley's prediction gave a better agreement with the experimental values and all his values fell within the range of experimental L_p.

Furthermore, with reference to Table 5.5 in which the results from all previous projects on octagonal sections were tabulated it is interesting to note that the equivalent plastic hinge length is apparently independent of the axial load level. Contrary to Baker's prediction, there is no significant trend of equivalent plastic hinge length increasing with the axial load level (Fig. 5.3a). However, from the table it appears that the aspect ratio does have some effect on the equivalent plastic hinge length, i.e. $\frac{L_p}{h}$ increases as the aspect ratio is increased. Potangaroa's tests (low aspect ratio) gave an average value of 0.35h and all the other tests (high aspect ratio) gave an average value of 0.54h for L_p.

5.4 CURVATURE DISTRIBUTIONS AND CURVATURE DUCTILITY FACTORS

The general pattern of curvature distributions, Figs. 4.4, 4.16, 4.24 and 4.31, shows a comparatively short extent of plasticity; the spread of plasticity was larger in higher axially loaded specimens, (e.g. Units Two and Three). Similar to the results obtained in Gill's and Potangaroa's tests, the plasticity does not appear to have a significant tendency to spread when the cyclic loading was repeated at the same displacement

ductility factor, but does spread when the factor is increased.

The maximum curvature in the case of more heavily loaded specimens tends to move away from the stub face to occur in the third gauge length (e.g. Unit Three). This phenomenon is due to the additional confinement effect from the stub which reduced the expansion of the concrete at the critical section at the stub face. Otherwise, in the case of Units One and Four, the maximum curvature concentrated in the first gauge length.

The maximum curvature ductility factor, $\frac{\phi_u}{\phi_y}$, was computed using the measured maximum curvature at the critical hinge. The two different values of ϕ_y derived using different methods (see Section 4.2.1(b)) gave rise to two different curvature ductility factors, one is always about twice the other. However, if assuming $\frac{\phi_u}{\phi_y} = 20$ and $L_p = 0.6h$, then using the following equation,

$$\mu = \frac{\Delta_y + \Delta_p}{\Delta_y} = 1 + 3 \left[\frac{\phi_u}{\phi_y} - 1 \right] \frac{L_p}{L} \left[1 - 0.5 \frac{L_p}{L} \right] \qquad (32)$$

where Δ_p = displacement (plastic) measured beyond the first yield displacement,

the value of displacement ductility factor is given as $\mu = 8.9$ which is high enough to allow the piers to survive through very severe earthquake.

The results from the trial set-up for curvature measurement (Sec. 2.3.1) failed to give good correlation with that from the existing method. This may be due to the close spacing of the strain gauges and the location of the set-up, i.e. in the hinge which did not experience much damage.

5.5 CONFINING STEEL STRAINS

Yielding of hoops of square specimens was not extensive, presumably as a result of provision of more confining steel than required by the draft concrete code. This occurred as a result of a lower value for f'_c obtained experimentally than used for design.

Of both cases only Unit Three experienced some yielding of the confining hoops at overall displacement ductility of 6.12 and higher. Though the supplementary cross-ties were not heavily stressed, the strain pattern (Figs. 4.25 and 4.32) at later stage of loadings pointed towards the confining effect of centre block.

In the two octagonal sections and in particular in Unit Two, the spiral steel yielding due to concrete confinement took place at comparatively early stages and the yielding was more extensive, even though

none of the spirals entered the strain hardening part of the steel stress-strain curve. However, the confining action was adequately maintained by the yielding spiral steel. The extra volumetric ratio of hoop steel in the square sections did not give any obvious overall improvement in performance. Hence, it is unnecessary and not justified to provide more confining steel so as to prevent any yielding of such steel. Both Gill's and Potangaroa's work arrived at the same conclusion.

Also in the case of octagonal sections, the confinement strains reduce markedly immediately adjacent to the centre block, (see Figs. 4.5 and 4.17). Obviously the centre block was providing additional confinement to the concrete, reducing its expansion and thus increasing the confining pressure.

Fig. 4.17 indicates the yielding of confining steel occurred over the full length of potential plastic hinge zone. This proved the necessity of increasing the length of column confined for heavily loaded columns, as recommended after Potangaroa's tests (2).

5.6 TRANSVERSE STEEL STRAINS DUE TO SHEAR

The plot of shear strains over the gauged distance, Figs. 4.6, 4.18, 4.25 and 4.32, reveals that, ignoring some exceptions, the shear strains increases (and in some cases reached yield) as displacement ductility increases, i.e. shear carried by transverse steel increases with ductility. Since the total shear force either remained approximately constant or decreased with ductility, in other words, the concrete must have degrading shear strength as the displacement ductility factor increased.

As reported in Potangaroa's tests, the yielding of spiral steel was much more extensive in the specimen under high axial load. Some of the spirals strain hardened during the later stage of testing, e.g. in Unit Two as compared to Potangaroa's Unit 5 - Stage 2.

Finally, it is important to draw to the attention that the arbitrary differentiation between the confining strains and shear strains is not very correct since the anchorage effect of "confining" action will affect the "shear resisting" action and vice versa. Consequently, shear carried by concrete mechanisms will, if anything, be underestimated.

5.7 ULTIMATE LOADS

Even though adjusted for $\phi = 1$, the ultimate loads predicted by

the ACI column design charts were still very conservative, as it is evidently shown in the figures in which the experimental peak loads plotted always exceed the predicted ultimate load indicated by the dashed line. Note that the correction for P-Δ effect was further magnified by a factor of $\frac{1.75}{1.60}$ because of the fact that the axial load was applied at the end of the member and not at the location of the pin.

There can be three contributing reasons for the discrepancies. Firstly, the ACI value of the ultimate compression strain of $\varepsilon_{cu} = 0.003$ adopted is very conservative. From Table 5.1, it can be seen that the maximum discrepancy in ultimate moment was about 110%, whereas the maximum discrepancy in Potangaroa's tests was about 126%. Both occurred with the most heavily loaded specimens.

Secondly, the increases in longitudinal steel stress due to strain hardening, and lastly, the increase in concrete compressive strength due to confinement from transverse steel and the centre block contributed to the increase in the experimental values.

5.8 ULTIMATE MOMENT CAPACITIES

In all the cases, the theoretical ultimate moment capacities based on the ACI column design charts (19) using actual material strengths and $\phi = 1$ led to very conservative estimates of the ultimate lateral load (Sec.5.7 Even by using ultimate compression strains of $\varepsilon_{cu} = 0.004$, the unconfined compression strength, f'_c, the ACI stress block (Fig. 5.1) and strain compatibility to calculate reinforcement stresses, the ultimate moments obtained were very close to that by using $\varepsilon_{cu} = 0.003$ (therefore they were not reported). As explained in References 2 and 3, these reserve moment capacities may lead to the undesirable underestimation of actual ultimate shear force, resulting in a potential for shear failure.

Of all factors causing the discrepancies, the enhancement of concrete strength by confinement is probably of the main concern. It has been a well known fact that the confined concrete core under a triaxial stress state possesses a greater compressive strength value than the unconfined concrete cylinder. Deriving from the following equation (26)

$$f'_{cc} = f'_c + 4.1\, f_\ell \qquad (33)$$

in which f'_{cc} is unconfined concrete strength

and f_ℓ is the average confining pressure, Fig. 5.2 .

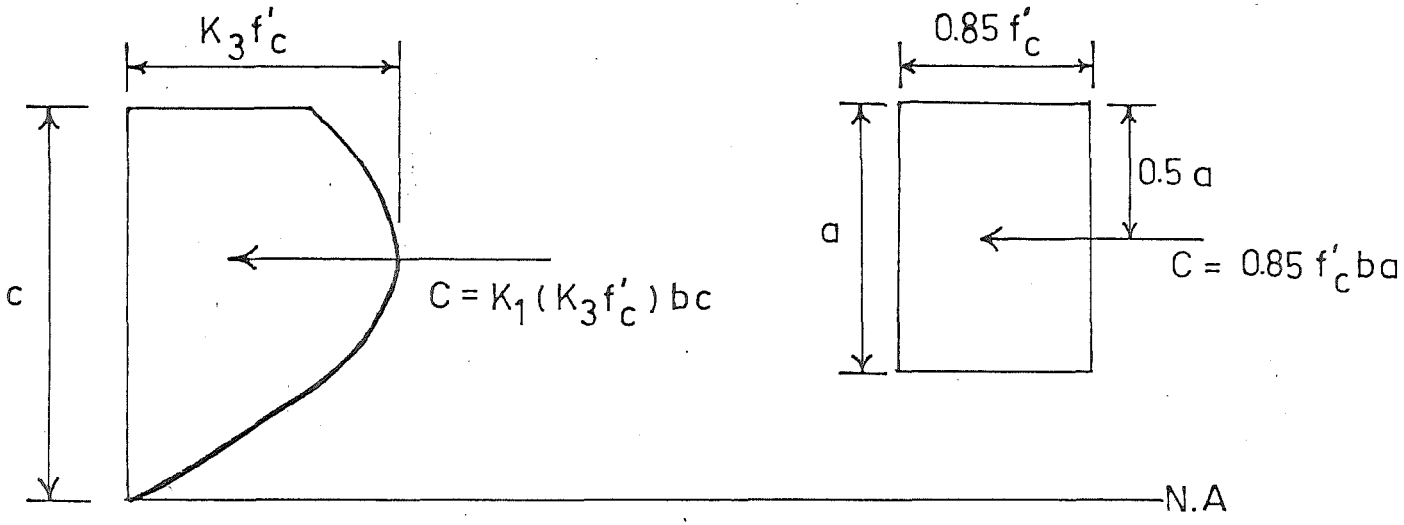

$$C = K_1 K_3 f'_c bc = 0.85 f'_c ba \qquad K_2 c = 0.5 a$$

$$K_1 K_3 = 0.85 \frac{a}{c} = 0.85 \beta_1 \qquad K_2 = 0.5 \frac{a}{c} = 0.5 \beta_1$$

$$\beta_1 = 0.85 \quad \text{for} \quad f'_c \leq 27.6 \text{ MPa}$$

$$= 0.85 - \frac{0.05}{6.89}(f'_c - 27.6) \quad \text{for} \quad f'_c > 27.6 \text{ MPa}$$

FIG. 5.1 ACI STRESS BLOCK

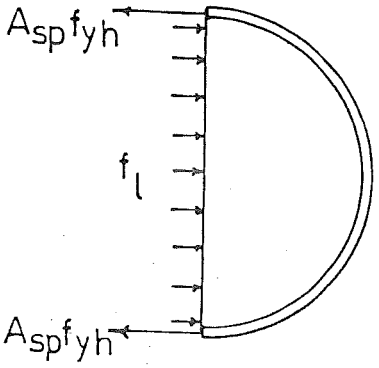

FIG. 5.2
CONFINING LATERAL PRESSURE

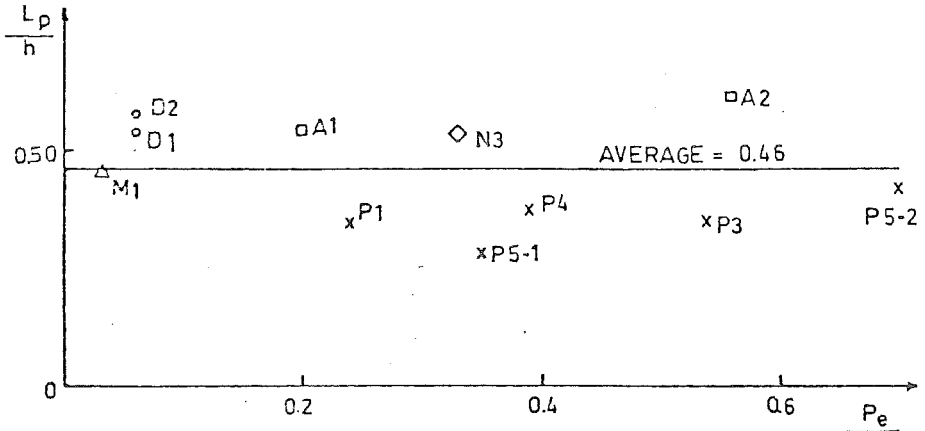

FIG. 5.3b $\frac{L_p}{h}$ vs $\frac{P_e}{f'_c A_g}$

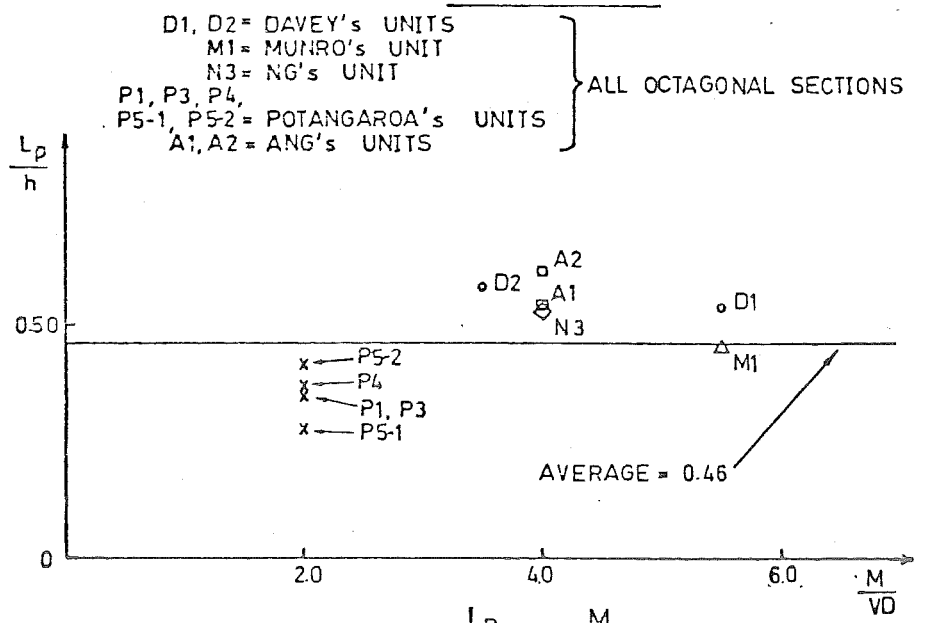

FIG. 5.3 a $\frac{L_p}{h}$ vs $\frac{M}{VD}$

$$f_{\ell} = \frac{2 f_{yh} A_{sp}}{d_s s_h} \qquad (34)$$

assuming the spiral steel is at yield.

Combining the above two equations and rearranging

$$f'_{cc} = f'_c \left(1 + 2.05 \rho_s \frac{f_{yh}}{f'_c}\right) \qquad (35)$$

Equation (35) is modified to take into account the assumption of the reduction in effectiveness to zero as the spiral spacing is increased to the spiral diameter in Equation (19) of Park-Leslie's model.

In the case of rectangular hoops, it is assumed that the efficiency, as far as strength enhancement is concerned, is about one-half of that of a circular spiral with the same ρ_s value. This enhancement is included in the Park-Kent's model, giving

$$f'_{cc} = f'_c \left(1 + \frac{\rho_s f_{yh}}{f'_c}\right) \qquad (27)$$

Table 5.3 lists the theoretical results of f'_{cc} using either Equation (19) or (27).

An alternative way of determining f'_{cc} using experimental data (Section 4.2.1(h)) was considered and the results obtained exceeded the predicted confined value by between 16% and 72%. The extra confinement afforded by the central stub is again apparent. It is interesting to note that if experimental N.A depth is used together with maximum ε_{cu} value, the f''_{cc} values will be in a better agreement with the theoretical f'_{cc} values but the axial load will be far from being balanced. e.g. Unit 1 - 120% difference, Unit 2 - 45% difference, and Unit 4 - 73% difference in axial load values.

To account for the contribution from the centre block, the ultimate moment was calculated based on core dimensions only and using the value of f'_{cc} given by either Equation (19) or (27), assumed constant over the full depth of the compression zone. The maximum concrete strain at the extreme compression fibre was that obtained experimentally in the test. The effect of enhancement is considered to affect a zone extending about $c/_2$ from the critical section, i.e. half the compression block depth. The calculated moment is considered to act at this section and is extrapolated to obtain the value at the critical column-stub junction. As the aspect ratio is about twice that of Gill's or Potangaroa's specimens, the distance moved through was only 5% of the distance to the point of contraflexure. (c.f. 10% in

TABLE 5.3 : COMPARISON OF ULTIMATE MOMENT CAPACITIES (kNm) AT HIGH CONCRETE COMPRESSION STRAINS

UNIT	Concrete Strength			At Concrete Compression Strain $\varepsilon_{cu} = 0.02$			At Maximum Compression Strain $\varepsilon_{cu(max)}$					
	f'_c	f'_{cc} Theoretical	f''^{*}_{cc} Experimental	Experimental	Analytical Stress-Strain Model		$\varepsilon_{cu(max)}$	Experimental Moment	Analytical Stress-Strain Model		Confined Stub using f'_{cc} (theoretical)	
					M_u	$\frac{M_{exp}}{M_u}$		M_{exp}	M_u	$\frac{M_{exp}}{M_u}$	M_u	$\frac{M_{exp}}{M_u}$
1	26.0	30.8	44.9 (32.6)	225	194	1.16	0.0405	262	163	1.60	248	1.06
2	28.5	36.9	63.5	245	223	1.10	0.1271	417	-	-	329	1.27
3	23.6	32.7	38.0 (35.1)	277	292	0.95	0.0232	336	296	1.14	332	1.01
4	25.0	31.2	40.2 (31.7)	260	265	0.98	0.0359	322	260	1.24	313	1.03

* The number within the brackets is the f''_{cc} value determined using experimental N.A. depth.

Potangaroa's units). However, excellent agreement is again obtained for all specimens except Specimen Two. 1% to 6% was the range of discrepancy. In the case of Unit Two, the stub confinement action is equivalent to moving the critical section by up to 7% of the distance to contraflexure point and the discrepancy was still 27%. Although this value is large it gives much better agreement than by using ACI charts (110% discrepancy). The simplicity of the approach and the absence of more reliable stress-strain model may justify the use of this method in estimating the ultimate moment capacity, say at $\varepsilon_{cu} = 0.04$.

The prediction of ultimate moment capacity for maximum experimental concrete strain using the analytical stress-strain curve for confined concrete was not as good as that outlined in the above paragraph. But from the calculations, it seems that the modified Park-Kent's model gives better agreement in the square sections than Park-Leslie's model for octagonal sections. The discrepancy in the latter case is 60%, too large to be just accounted for by the shifting of critical section from the face of the stub. So, it is probable that the falling branch may be too steep, particularly for low confinement ratios.

For further comparison, the ultimate moments at $\varepsilon_{cu} = 0.02$ using the analytical models were calculated. The results obtained show a very good agreement with the experimental values at the same concrete compression strain. It is again evident that the performance of modified Park-Kent's model (only 2%-5% discrepancy) is more superior than the Park-Leslie model (10%-16% discrepancy). Gill's results using $\varepsilon_{cu} = 0.005$ with modified Park-Kent's model also illustrated the excellent performance (3). Nevertheless, these two models have the advantage of simplicity of application, and if adjusted for influence of central stub, they will give a reliable prediction.

5.9 ULTIMATE SHEAR CAPACITIES

Table 5.4 gives a comparison of shear forces carried by the concrete as predicted by the three different codes (16, 17, 18). The experimental values were taken by subtracting the steel contribution from the total maximum shear using measured steel stresses at the same shear force, and assuming a 45° diagonal tension crack.

As it was mentioned in Section 5.6, the distinction between shear strains and confining strains was not very clear, the measured shear strains, due to confining action, can be considerably higher than it should be. So, resulting in an underestimated contribution from

TABLE 5.4 : ULTIMATE SHEAR FORCES (kN)

UNIT	Experimental Maximum Shear Force, V_{exp} *	Plastic Hinge Regions						Outside Plastic Hinge Regions		
		V_s	V_c	$\frac{v_c}{\sqrt{f'_c}}$	V_c 1st Draft DZ 3101	V_c 2nd Draft DZ 3101	V_c ACI Approx.	V_s **	V_c	$\frac{v_c}{\sqrt{f'_c}}$
1	136.5 (136.6)	79	57.5	0.103	90	135	132	47	89.5	0.160
2	157.0 (129.5)	157	0	0	205	232	210	65	92.0	0.164
3	189.0 (162.4)	172	17.0	0.024	179	215	196	175	14.0	0.020
4	155.5 (157.0)	77.5	78.0	0.109	119	139	169	175	0	0

* The number in brackets indicates the predicted Ultimate Shear Force

** Assuming yield of transverse steel

TABLE 5.5 : VARIATION OF EQUIVALENT PLASTIC HINGE LENGTH WITH AXIAL LOAD LEVEL, SPIRAL STEEL CONTENT AND ASPECT RATIO

UNIT	Axial Load Level $\frac{P_e}{f'_c A_g}$	Spiral Steel content ρ_s	Aspect Ratio $\frac{M}{VD}$	Equivalent Plastic Hinge Length L_p (mm)	$\frac{L_p}{h}$	Remarks
Davey's (10)						
Unit One	0.06	0.0044	5.5	270	0.54	at $\mu = 5$
Unit Two	0.06	0.0044	3.5	292	0.58	at $\mu = 5$
Munro's (12)						
Unit One	0.03	0.0126	5.5	225	0.45	at $\mu = 6$
Ng's (13)						
Unit Three	0.33	0.0244	4.0	1.33	0.53	at $\mu = 4$
Potangaroa's (4)						
Unit One	0.24	0.0075	2.0	211	0.35	Average at $\mu = 8$
Unit Three	0.54	0.0112	2.0	207	0.35	Average at $\mu = 4$
Unit Four	0.39	0.0080	2.0	223	0.37	Average at $\mu = 8$
Unit Five (Stage 1)	0.35	0.0261	2.0	168	0.28	Average at $\mu = 8$
Unit Five (Stage 2)	0.70	0.0261	2.0	254	0.42	Average at $\mu = 8$
Present Project						
Unit One	0.20	0.00756	4.0	216	0.54	Average for $\mu \geq 4$
Unit Two	0.56	0.01527	4.0	242	0.61	Average for $\mu \geq 4$

concrete, if V_c is to be determined by the above method.

The First Draft of DZ 3101 (16) adopts a reduced concrete shear capacity within the plastic hinge region, given by the expression

$$v_c = 0.25 \left[1 + \frac{f'_c}{25}\right] \sqrt{\frac{p_e}{A_g} - \frac{f'_c}{10}} \qquad (36)$$

where all units are MPa.

Only the approximate ACI equation is taken for comparison. The equation as given by Clause 11.3.1.2

$$v_c = 0.17 \left[1 + 0.073 \frac{p_e}{A_g}\right] \sqrt{f'_c} \qquad (37)$$

The ACI provisions do not differentiate between concrete shear capacity within and outside plastic hinge regions, and the First Draft of DZ 3101 adopts the same ACI approximate equation for concrete shear capacity outside the plastic hinge region.

The values of V_u reported in References (2) and (3) did not take into account the $P-\Delta$ effect on the specimens, particularly those under high axial load. The values of V_u calculated from $V_u = \frac{M}{L}$, where M is the maximum experimental moment, were higher than the values obtained by just taking $V_u = \frac{H_u}{2}$. In point of fact, the actual shear within the plastic hinge zone will be intermediate between the two values, as in the immediate vicinity of the central stub, the shear found from $V = \frac{\partial M}{\partial L}$ will correspond to the higher value, but outside the plastic hinge zone, where most curvature will have occurred, the shear will correspond to the lower value. (See Section 2.1.1(g)). As a result, the experimental values of V_c might not be so high as reported. Nevertheless, the difference is not so great as to reverse the conclusion arrived at.

In the present project, it was found that the transverse steel for confinement in the plastic hinge regions was sufficient to carry all shear in the heavily loaded specimens. Hence, little was expected of the concrete for shear resistance. However, in Units One and Four, concrete contributed almost half of the shear resistance. All the three codes predicted much higher values for V_c. The conservatism reported in Reference 2 cannot be observed in these results.

The situation did not differ much in the regions outside the plastic hinges, though the concrete contribution in the two octagonal sections tend to increase slightly. However, due to insufficient strain gauges in these regions, it is to be noted that the estimation of V_s by assuming the

yielding of all transverse steel was very conservative.

Due to the uncertainty in some of the shear strain measurement, the contribution of transverse steel in shear resistance is doubtful and this contribution is further exaggerated by taking the maximum measured strain value as representative. Thus, the actual concrete shear resistance might be more than that shown in Table 5.4.

5.10 CODE PROVISIONS FOR TRANSVERSE CONFINEMENT STEEL FOR DUCTILITY

Fig. 5.4a compares the variation of volumetric ratio of confinement steel with axial load level for the two octagonal sections confined in accordance with First Draft of DZ 3101 (16), Second Draft of DZ 3101 (17) and ACI 318-77 (18). The requirements of first code result in lower confinement ratios than ACI values (Clause A6.5.2) for $\frac{P_e}{f'_c A_g} < 0.5$ while the modified equations in second code give lower values for $\frac{P_e}{f'_c A_g} < 0.4$. Obviously, from the performance of Unit One, the requirements of Second Draft of DZ 3101 was sufficient to ensure a ductile behaviour of the pier. In the case of heavily loaded Unit Two, the high curvature ductility as a result of the high spiral steel content required by the code (17) was evidently demonstrated during the test. The other two codes (16,18) demand lower volumetric ratios of confinement steel for high axial load levels and thus, such high ductility may not be achieved. However, moment curvature analyses of typical sections (28) indicated that the provisions of First Draft of DZ 3101 were adequate to ensure curvature ductility factors well in excess of 5 without a decrease in moment capacity greater than 20%.

The ACI provisions adopt the philosophy that the axial load strength of the column before spalling of cover concrete should be maintained even after the spalling has taken place. The code also assumes that the efficiency of rectangular hoops as confining reinforcement is 50% of that of spirals. This resulted in the following equation (Clause A6.5.3)

$$A_{sh} = \frac{\ell_h \rho_s s_h}{2} \tag{38}$$

where

$$\rho_s = 0.45 \left(\frac{A_g}{A_c} - 1 \right) \frac{f'_c}{f_{yh}} \tag{39}$$

$$\geq 0.12 \frac{f'_c}{f_{yh}}$$

and ℓ_h is the maximum unsupported length of rectangular hoop measured

between perpendicular legs of hoop. Reference to Fig. 5.4b shows that the ACI provisions are very conservative. Within the permissible axial load levels, compared to ACI requirements, columns designed according to the New Zealand standards (16,17) need much less transverse confinement steel but are still capable of maintaining the necessary ductile behaviour. In view of such great differences between ACI and New Zealand standards, it can possibly be ruled that, due to smaller experimental f'_c values, the difference in the transverse steel provided and that required by the code (Sec. 4.1) is negligible. In spite of all the discrepancies, the ductile behaviour of the two square sections was apparent in the tests.

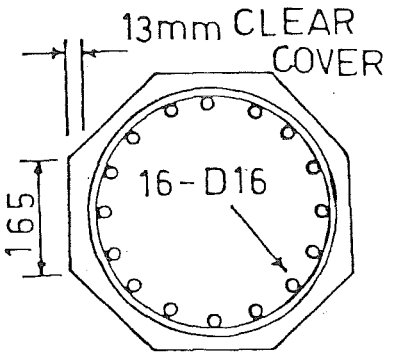

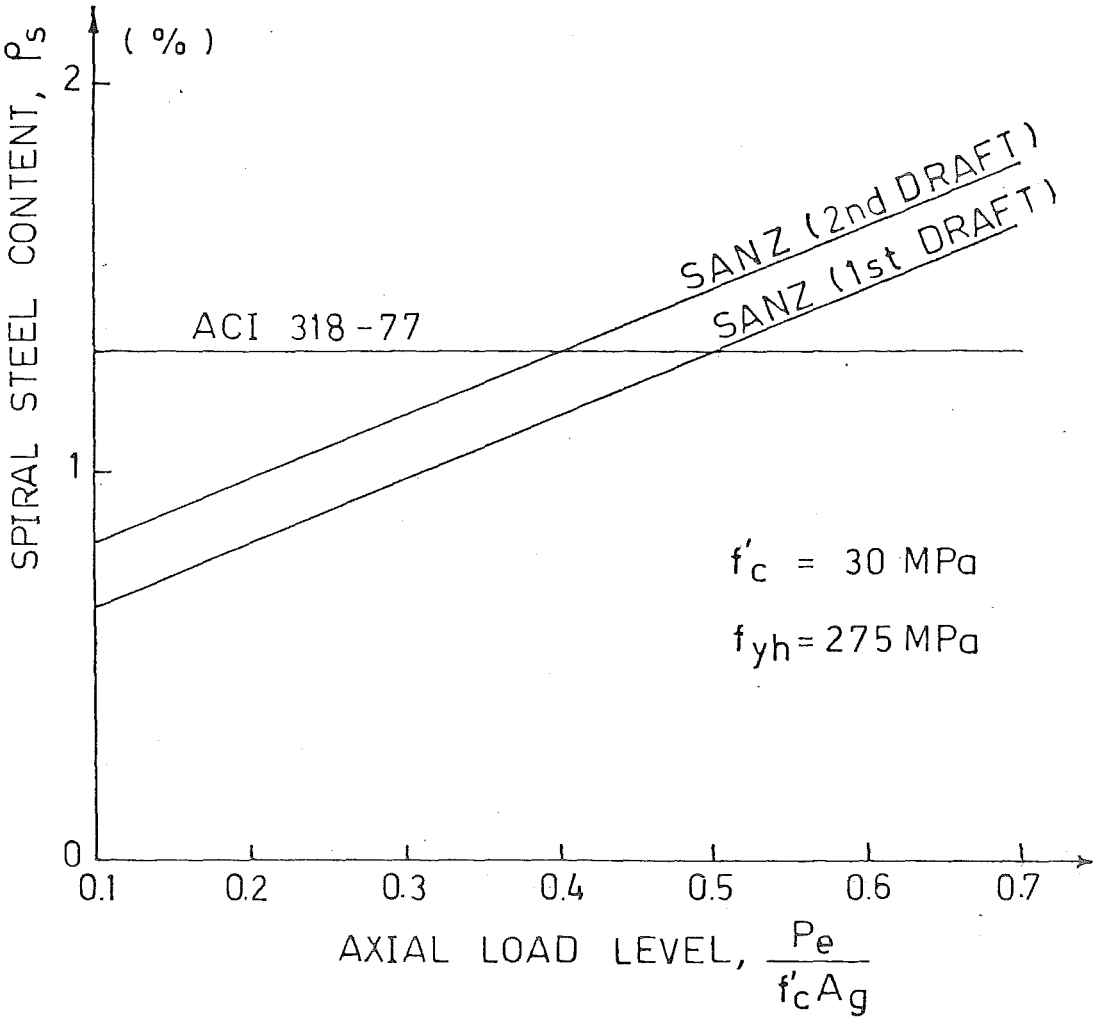

FIG. 5.4a CODE PROVISIONS FOR TRANSVERSE STEEL FOR CONFINEMENT

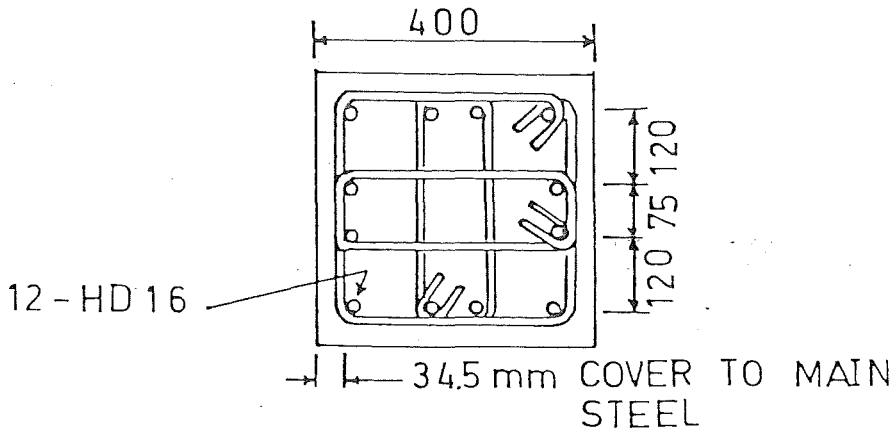

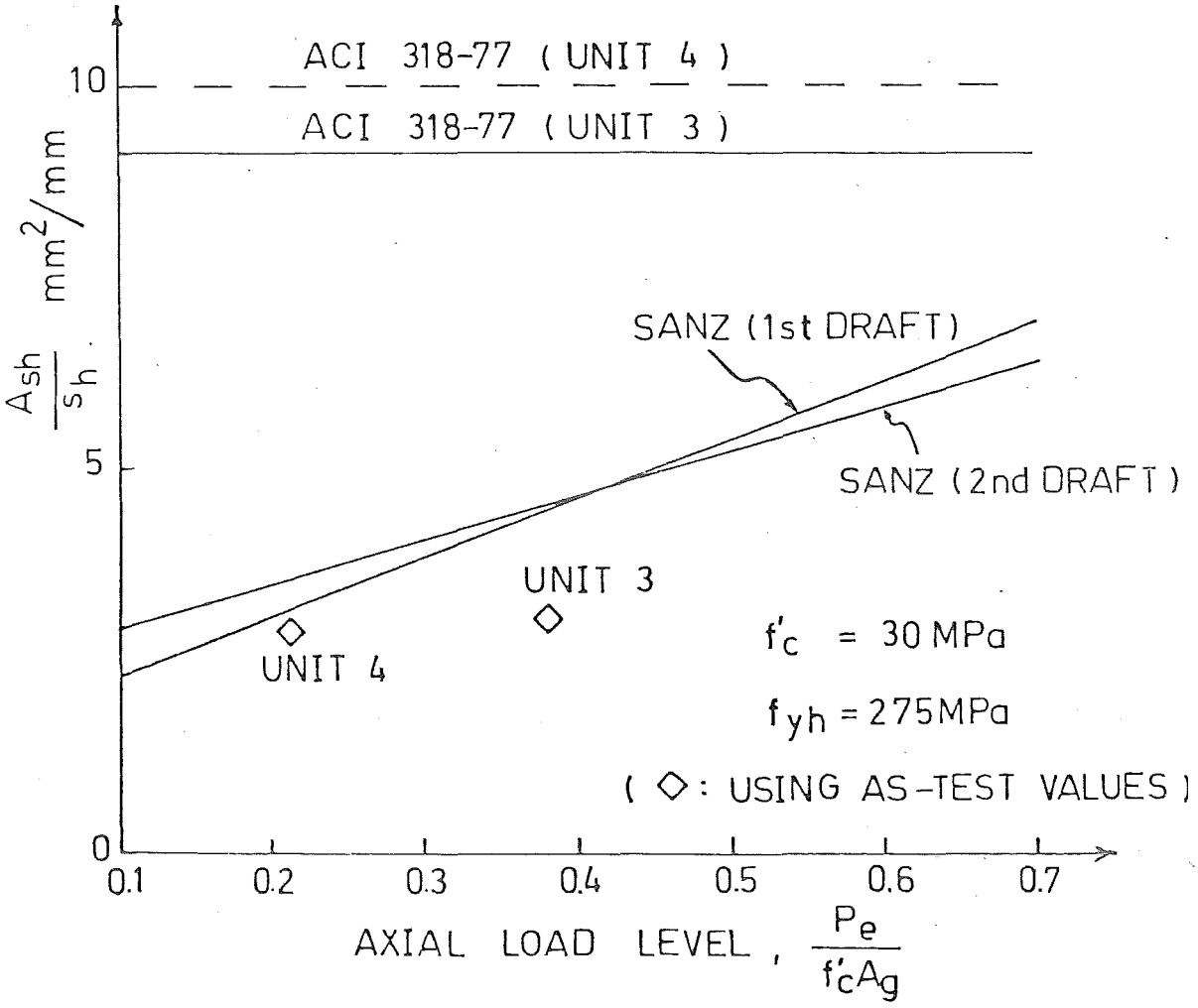

FIG. 5.4b CODE PROVISIONS FOR TRANSVERSE STEEL FOR CONFINEMENT

CHAPTER SIX

CONCLUSIONS AND RECOMMENDATIONS FOR FUTURE RESEARCH

6.1 CONCLUSIONS

(a) Lateral Load-Displacement Relationship

If adequate confinement in potential plastic hinge regions is provided, as required by Reference 17, the hysteresis behaviour is not influenced by the aspect ratio up to at least $\mu = 8$, i.e. before the on-set of incipient buckling. The good energy dissipating potential is unchanged by an increase in the aspect ratio.

Yield displacements estimated by using the transformed cracking section modulus and the theoretical bending moment distribution are within acceptable limits.

(b) Concrete Comression Strains

The traditional assumption of 0.003 for ultimate concrete compressive strain is extremely conservative. More than ten times this value is possible for the extreme compression strain of the confined core. The extreme concrete fibre strain at first crushing is about 0.008. Both theoretical estimations by Equations (28) and (29) are too conservative, though Corley's equation gives better agreement.

(c) Equivalent Plastic Hinge Lengths

The equivalent plastic hinge lengths do not depend on the displacement ductility factor, and to a certain extent, the axial load level. The plastic hinge lengths prediction by Baker are not conservative, i.e. overestimating L_p, whereas Corley's prediction gives a better agreement.

The equivalent plastic hinge length can be reasonably taken to be 0.5h for all specimens (h = overall column depth), which is smaller than normally assumed.

(d) Curvature Distributions and Curvature Ductility Factors

Curvature distributions indicate the concentration of plasticity in a small region around the critical sections. This plasticity zone tends to spread as the axial load is increased. As a result of the tests, it was assessed that it is possible for the columns to reach a curvature ductility factor of about 20, and hence, giving displacement ductility of approaching 9.

(e) Confining Steel Provisions

Though some of the transverse steel reached yield strain, the performance of the columns was not affected. It appears that the yield confinement steel still continued to provide adequate confinement as the displacement ductility factor was progressively increased. Hence, it is unnecessary and not justified to design the confining steel to be in the elastic stage.

(f) Ultimate Moment Capacities

There is an obvious increase in concrete compressive strength, resulting from the confining action of the transverse steel and the centre block. This increase causes the flexural strength of the specimens to be in excess of that predicted by ACI charts.

Using the calculated f'_{cc} value and assuming the critical section to be $c/_2$ away from the central stub, the ultimate moment at the column-stub interface can be calculated quite accurately.

The Park-Leslie's and modified Park-Kent's models give acceptable estimation if higher concrete strain is used. However, Park-Leslie's model seems to have an incompatabily steep falling branch.

(g) Ultimate Shear Capacities

No increase in concrete shear strength by confining steel is apparent in the results. Due to insufficient strain data, it is difficult to assess the shear resistance contribution by the transverse steel. Hence, the contradicting results with the previous two projects (4,5) may not carry much meaning. However, it is worthwhile noting that "shear" strains are increased by increasing the axial load level. This effect is quite significant.

6.2 RECOMMENDATIONS FOR FUTURE RESEARCH

(a) More testing at other axial load levels to investigate the influence of aspect ratio may be necessary to further confirm the conclusion arrived at.

(b) If the situation allows, testing of units with different ratios of shear span to lateral dimension will give some indication of the extent of influence of aspect ratio.

(c) More investigation into the concrete shear resistance, especially its relationship with confinement, with more extensive and

careful strain gauging may be needed to confirm the inference made in Reference 2.

(d) With the availability of the present loading frame, if possible with some modifications, to carry out the tests using actual dynamic earthquake loadings on full-size specimens.

(e) Testing with variable axial load to represent varying load on a two-column pier.

APPENDIX

REFERENCES

1. NZS 4203:1976, "Code of Practice for General Structural Design and Design Loadings for Buildings".

2. M.J.N. Priestley, R. Park, and R.T. Potangaroa, "Ductility of Spirally Confined Concrete Columns", Journal of Structural Division, ASCE, Vol. 107, ST1, January 1981.

3. R. Park, M.J.N. Priestley, and W.D. Gill, "Ductility of Square Confined Reinforced Concrete Columns", submitted to Journal of Structural Division, ASCE.

4. R.T. Potangaroa, "Ductility of Spirally Reinforced Concrete Columns Under Seismic Loading", M.E. Report, University of Canterbury, New Zealand, 1979.

5. W.D. Gill, "Ductility of Rectangular Reinforced Concrete Columns with Axial Load", M.E. Report, University of Canterbury, New Zealand, 1979.

6. D.C. Kent, "Inelastic Behaviour of Reinforced Concrete Members with Cyclic Loading", Ph.D. Thesis, University of Canterbury, New Zealand, 1969.

7. R.A. Sampson, "Ductility of Reinforced Concrete Columns", M.E. Report, University of Canterbury, New Zealand, 1971.

8. J.A. Norton, "Ductility of Rectangular Reinforced Concrete Columns", M.E. Report, University of Canterbury, New Zealand, 1972.

9. P.D. Leslie, "Ductility of Reinforced Concrete Bridge Piers", M.E. Report, University of Canterbury, New Zealand, 1974.

10. B.E. Davey, "Reinforced Concrete Bridge Piers Under Seismic Loading", M.E. Report, University of Canterbury, New Zealand, 1974.

11. A.J. Cameron, "The Response of Reinforced Concrete Bridge Piers to Seismic Motions", M.E. Report, University of Canterbury, New Zealand, 1975.

12. I.R.M. Munro, "Seismic Behaviour of Reinforced Concrete Bridge Piers", M.E. Report, University of Canterbury, New Zealand, 1976.

13. K.H. Ng, "Seismic Behaviour of Circular Reinforced Concrete Bridge Piers", M.E. Report, University of Canterbury, New Zealand, 1978.

14. D.C. Kent, and R. Park, "Flexural Members with Confined Concrete", Journal of Structural Division, ASCE, Vol. 97, ST7, July 1971, pp.1969-1990.

15. "Highway Design Brief", Ministry of Works and Development, New Zealand, Issue C, July 1973.

16. "Code of Practice for the Design of Concrete Structures", First Draft DZ 3101, Standards Association of New Zealand, 1978.

17. "Code of Practice for the Design of Concrete Structures", Second Draft DZ 3101, Standards Association of New Zealand, 1980.

18. ACI Committee 318, "Building Code Requirements for Reinforced Concrete", ACI 318-77, American Concrete Institute, 1977.

19. ACI Committee 340, "Ultimate Strength Design Handbook", Vol. 2, American Concrete Institute.

20. M.J.N. Priestley and R. Park, "Seismic Resistance of Reinforced Concrete Bridge Columns". Proceedings of Workshops on Earthquake Resistance of Highway Bridges, Applied Technology Council, Palo Alto, Nov. 1979, pp.253-284.

21. A.L.L. Baker and A.M.N. Amarakone, "Inelastic Hyperstatic Frames Analysis", Proceedings of the International Symposium on the Flexural Mechanics of Reinforced Concrete, ASCE-ACI, Miami, Nov. 1964, pp.85-142.

22. W.G. Corley, "Rotational Capacity of Reinforced Concrete Beams", Journal of Structural Division, ASCE, Vol. 92, ST5, Oct. 1966, pp. 121-146.

23. R.K.T.S. Iyengar, P. Desayi and K.N. Reddy, "Stress-Strain Characteristics of Concrete Confined in Steel Binders", Magazine of Concrete Research, Vol. 22, No. 72, Sept. 1970, pp. 173-184.

24. R. Park, D.C. Kent, and R.A. Sampson, "Reinforced Concrete Members with Cyclic Loading", Journal of the Structural Division, ASCE, Vol. 98, ST7, July 1972.

25. M.J.N. Priestley, R. Park, B.E. Davey, and I.R.M. Munro, "Ductility of Reinforced Concrete Bridge Piers", Proc. 6th World Conf. on Earthquake Engng, New Delhi, Jan. 1977.

26. R. Park and T. Paulay, "Reinforced Concrete Structures", John Wiley and Sons, New York, 1975.

27. R. Park and R.W.G. Blakeley, "Seismic Design of Bridges", RRU Bulletin 43, Bridge Seminar 1978, Vol. 3, Wellington, New Zealand.

28. R. Park and P.D. Leslie, "Curvature Ductility of Reinforced Concrete Columns Confined by the ACI Spiral", Sixth Australasian Conference on the Mechanics of Structures and Materials, Vol.1, Christchurch, Aug. 1977, pp.342-349.

Classn:

DUCTILITY OF REINFORCED CONCRETE BRIDGE PIERS UNDER SEISMIC LOADING

Ang Beng Ghee

ABSTRACT: Results are presented of tests on two octagonal and two square bridge piers under simulated seismic loadings, intending to investigate the influence of aspect ratio on their post-elastic ductile behaviour. It is concluded that such influence is insignificant for piers confined in accordance to the present N.Z. code provisions.

Department of Civil Engineering, University of Canterbury
Master of Engineering Report, 1981.